



SAPIENZA
UNIVERSITÀ DI ROMA

Virtual micro-reality

Immersive manipulation of live microscopic systems

Scuola Dottorale in Scienze Astronomiche, Chimiche, Fisiche, Matematiche
e della Terra "Vito Volterra"

Dottorato di Ricerca in Fisica – XXXIII Ciclo

Candidate

Stefano Ferretti

ID number 1567525

Thesis Advisor

Roberto Di Leonardo

March 2021

Thesis defended on 6th July 2021
in front of a Board of Examiners composed by:
Prof. Stefano Lupi (chairman)
Prof. Miriam Vitiello
Prof. Dario Gerace

Virtual micro-reality

Ph.D. thesis. Sapienza – University of Rome

© 2021 Stefano Ferretti. All rights reserved

This thesis has been typeset by L^AT_EX and the Sapthesis class.

Author's email: ferretti.1567525@studenti.uniroma1.it

Abstract

For more than three centuries we have been watching and studying microscopic phenomena behind a microscope. We discovered that cells live in a physical environment whose predominant factors are no longer those of our scale and for which we lack a direct experience and consequently a deep intuition. Today's computational approaches to microscopy allow high frame rate volumetric reconstructions from 2D holographic patterns that encode the full 3D structure of the sample. On a parallel track, modern holographic spatial light modulators integrated in optical tweezers setups allow to dynamically arrange complex many-particles systems in precise 3D configurations. In this regard, highly efficient iterative algorithms ensure quick hologram computation for the live refresh of the spatial light modulator.

In this PhD thesis, we present a novel instrument which, by integrating holographic and virtual reality technologies, allows the user to be completely immersed in a dynamic virtual world which is the simultaneous replica of a real system under the microscope. We use a 3-axis implementation of holographic microscopy for fast 3D imaging and real-time rendering on a virtual reality headset. At the same time, hand tracking data is used to dynamically generate holographic optical traps that can be used as virtual projections of the user hands to interactively grab and manipulate ensembles of micro-particles or living motile cells, like swimming bacteria. The strategy used can be flexibly adapted to different sample types by integrating suitable 3D imaging techniques into the system. The dynamics of larger eukaryotic cells is observed using the gradient light interference microscopy label-free technique, which provides quantitative height maps of the specimen. Our interface allows a more direct interaction with systems at the micron scale. The user can immersively explore a microscope sample of colloidal particles or living cells, analyze their motility interactively and with quantitative tools, control optical traps to catch, reorient, probe and eventually release individual bacterial cells.

A further project is also presented, in which the diffraction-limited laser spot is exploited for lithographic purposes. Arbitrary shaped micro-structures with submicrometer 3D resolution can be fabricated by direct laser writing on photosensitive resins. Using this strategy, we developed an optical reaction micro-turbine made of curved micro-fibers that can maximally exploit light's momentum to generate a strong, uniform, and controllable torque. The real-time fabrication of custom micro-structures as well as their operation and manipulation within an immersive environment represent intriguing add-ons to implement in our virtual reality interface.

Contents

1	Introduction	1
2	Tele-manipulation at the atom scale	4
2.1	STM-based nanomanipulator	4
2.2	AFM-based nanomanipulator	6
2.3	Limitations and perspectives	12
3	Holographic tweezers	14
3.1	Principles of optical trapping	14
3.2	Holographic tweezers: interactive multi-trap systems	23
3.3	Computer generation of digital holograms	28
4	Holographic microscopy	37
4.1	In-line digital holographic microscopy: advantages and limitations	38
4.2	3-axis holographic microscopy: 3D imaging of swimming bacteria	41
5	Virtual reality	48
5.1	VR hardware: headset and hand-tracking devices	49
5.1.1	Data transfer protocol	51
5.2	VR software: immersive micromanipulation interface	54
6	Virtual micro-reality	61
6.1	Colloidal particles and living bacteria	61
6.1.1	Falling bodies	61
6.1.2	Handcrafting micro-structures	62
6.1.3	Fishing for bacteria	65
6.2	Generic 3D objects	67
6.3	Eukaryotic cells	70
7	An optical reaction micro-turbine	77
8	Conclusion	86
8.1	Author contributions	87
A	Light propagation through a spherical lens	89
	Bibliography	96

Chapter 1

Introduction

During the second half of the 17th century, scientists like Hooke and van Leeuwenhoek revealed to the world the beauty and complexity of a microscopic universe that was made visible for the first time by microscope lenses. Centuries of developments in optical design have perfected optical hardware to produce detailed and aberration free images. In more recent years, lasers, digital cameras, spatial light modulators, and consumer high performance computing are transforming the optical microscope into an active investigation tool with ever expanding possibilities for interactions with microscopic systems. Using optical tweezers [1–3] we can trap individual cells [4], measure their mechanical stiffness [5], or arrange them in precisely controlled 3D micro-environments [6]. Furthermore, highly focused laser beams can also be employed in two-photon lithography for 3D printing of arbitrary shaped microstructures [7–9]. Ultraviolet (UV) curing resins polymerize upon absorption of a single UV photon. Polymerization can also occur by two-photon absorption in the near infrared spectrum, provided that the light intensity is high enough. In this regard, high intensity fields are obtained by tightly focusing a pulsed laser beam. The great advantage of two-photon absorption lies in its cross section, which scales as the square of the light intensity. The effective point spread function along the optical axis, therefore, is much smaller than for one-photon absorption. Thus, custom micro-objects with submicrometer resolution result from scanning the laser focal spot along a predetermined 3D trajectory.

Although a few advanced interfaces for optical tweezers have been proposed to replace the computer mouse with a multi-touch interface [10] or force-feedback devices [11], the visual feedback has always been limited to 2D projections viewed through the window of a computer display. Computational approaches to microscopy allow high frame rate volumetric imaging by numerical reconstructions based on 2D holographic patterns that encode the full 3D structure of the scene [12–17]. On a parallel track, virtual reality (VR), augmented reality and mixed reality are transforming the way we explore and acquire information from the macroscopic world around us. Applications in science are still very limited but potentially transformative in many fields. Neuroscientists are increasingly using virtual reality to explore the inner workings of animal and human brains [18] by simulating real world inputs. In the context of molecular dynamics simulations, virtual reality interfaces are found to facilitate sophisticated molecular modeling tasks [19]. It

has also been shown that virtual reality can play an important role in scientific education and training, allowing safe and economical experiments to be performed in virtual laboratories [20]. In all of these applications, however, virtual reality is doubly artificial being a software rendering of software objects. More than simulating presence in artificial environments, using virtual reality we can be virtually present in real but physically inaccessible worlds to explore and manipulate them from “within”.

This idea of tele-operation in the nano and micro world was first put forward using the scanning tunneling microscope (STM) [21]. By connecting a haptic device to the scanning tip of a STM and using a virtual reality headset to render topographic reconstructions, the user could either “fly” over the surface or “feel” the surface under his hand or deposit gold mounds over it [22]. Following this pioneering work, the field of tele-nanorobotics has shifted towards the use of the atomic force microscope (AFM) [23], which offers the advantages of being more suitable for a wider range of samples, including biological cells and macro-molecules, and also to provide direct force measurements for tactile feedback. Using a haptic device and 3D topographic reconstructions for visual feedback, it is possible to manipulate strands of DNA, nano-tubes, and other macro-molecules that lie on a surface [24]. However, the use of a scanning tip involves a few drawbacks: 1) imaging and manipulation need the same tip and cannot be simultaneous; 2) 3D reconstructions are slow and limited to topographic surfaces, preventing applications to objects that float and move in a 3D space; 3) manipulation is limited to “pushing with the tip” and, although more complex operations could be performed using two tips for grabbing, this is actually slow, cumbersome, and invasive [25].

In this PhD thesis, we present a novel approach to tele-micromanipulation that is fully based on optical tools for simultaneous 3D visualization and real-time manipulation of micro-systems through an immersive virtual reality interface. Through this instrument, we can be virtually “shrunk” by a million times and sent inside a sealed microscope slide where we can grab swimming cells on the fly and use our hands to interactively arrange colloidal particles in precise 3D geometric configurations. A 3-axis implementation of holographic microscopy [26, 27] allows the real-time reconstruction of a 3D scene that is the simultaneous replica of a real microscopic sample sitting under a microscope in a separate laboratory room. Using hand tracking devices, we project our hands in this virtual micro-reality and use them to grab and move microscopic objects by means of optical traps that are reconfigured in real time based on hand tracking data. Part of this project has been published in Ref. [28].

In chapter 2 we report the first examples of tele-exploration of nano-systems using either STM or AFM based instruments; the main drawbacks of such strategies are discussed as well. Chapter 3 presents the optical tweezers technique, from its principles to the dynamic multi-trap upgrade obtained by integrating digital holographic devices in the original setup. In chapter 4 we discuss the principles of digital holographic microscopy imaging, with a particular focus on our 3-axis implementation of the technique. Chapter 5 explains the strategy adopted to design our system, together with the optical and VR hardware as well as the VR software we developed. In chapter 6 we report a series of exploratory experiments with

microscopic systems composed of both synthetic micro-spheres and live swimming bacteria. Some preliminary results regarding the 3D imaging of generic objects and the analysis of living eukaryotic cells are also shown. Further developments in computational microscopy will allow direct interaction with more complex objects like larger eukaryotic cells or complex micro-machines [29], which could be assembled and operated in an immersive environment. In chapter 7, finally, we report the results of a further project in which I was involved during the first year of my PhD. The experiments aimed to develop an optimized design for an optical-reaction micro-turbine that could maximally convert optical power into mechanical power. Such a project also included a detailed experimental and theoretical study of losses in curved optical waveguides with curvature radii in the micron range, which was fundamental to obtain a design for our optical turbine that maximized the torque-to-power performance.

Chapter 2

Tele-manipulation at the atom scale

Tele-operation (*i.e.* the controlled action at a distance) is a common practice in everyday life to extend man reach into hostile or distant environments. The interactive tele-operation over length scales $10^6 - 10^{10}$ times smaller than ours, however, needs tailored equipment and strategy to be performed. Manipulating micron-sized and smaller objects requires a technology able to operate at microscopic scales following macroscopic input commands. At the same time, only the live sensing of the microscopic system response allows for a real interactive experience. This scenario became feasible after the invention of the scanning tunneling microscope and the atomic force microscope, which can provide atomic-size 3D topographic images. In this chapter, we report the first examples of tele-exploration at the nano scale based on these two instruments.

2.1 STM-based nanomanipulator

The first conception of the idea of tele-operation in the nano- and micro-world involved the use of the scanning tunneling microscope [21,30]. Originally designed to aid in understanding the growth, structures, and electrical properties of very thin oxide layers [31,32], the STM allows to measure surface topographies with nanometric resolution, as well as to manipulate atoms and molecules on a surface [33,34]. The core concept of the STM, sketched in Fig. 2.1(a), consists of a conducting tip (usually metallic) scanning a conducting sample (the surface under study) under the control of a piezoelectric 3D positioning system. A bias voltage is applied to the sample with respect to the tip. At very close range (of the order of a few tenths of nm), a tunneling current flows between the tip and the surface. This current decreases exponentially with the distance between the tip and the sample. A way to derive the topography of the sample is to raster the tip back and forth across the surface, while a feedback circuit maintains a fixed tunneling current and thus a constant distance between the tip and the sample. A scan of the surface proceeds by repeatedly moving the tip in x and y directions and then reading the voltage on axis z to determine the surface height. The key to the resolution of the STM is that the length of the piezoelectric positioners can be accurately controlled with

subnanometer resolution, and that the tunneling current is extremely sensitive to tip-to-sample separation. The standard method of STM data visualization during data collection is to construct gray scale images where dot brightness corresponds point-by-point to the surface height. We report in Fig. 2.1(b) the example of a STM image of cleaved graphite surface in air, which is a particularly well suited material to appreciate the STM atomic resolution [35].

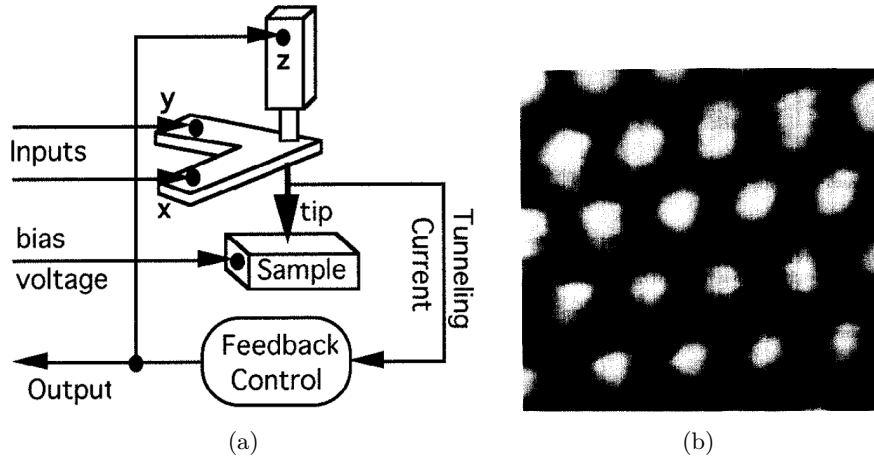


Figure 2.1. (a) Sketch of the STM core structure. A piezoelectric controller guides a conducting tip over a conducting surface, to which a bias voltage is applied respect to the tip. At very short range a tunneling current flows between the tip and the sample. By keeping this current constant, a feedback circuit reads the height of the surface. (b) STM image of cleaved graphite in air ($1.1 \times 1.1 \text{ nm}^2$). Taken from [22] and [21].

In addition to its ability to provide accurate height maps, the tip of the STM can be used as a local probe to modify the surface [36]. A way to accomplish this task is to physically touch the latter with the tip, which causes large and unpredictable modifications to both the tip itself and the surface as well. A more controlled method is to apply a voltage pulse between the tip and the surface. As the distance dividing them is so small, even moderate voltages produce a strong electric field. In this way, either clusters or single atoms can be removed from a surface, with the amount of transferred material per pulse depending on the distance from the bottom of the tip to the sample surface. By applying an opposite voltage, atoms can also be transferred back from the tip to the sample [37, 38]. In this way, it is possible to arrange single atoms on surfaces into patterns [39], or to push and move individual molecules [38, 40–42].

As mentioned before, successfully operating the manipulator is largely dependent on the quality of the feedback information. Connecting a haptic controller to the scanning tip of a STM results in a tele-operator that provides the sensation of “feeling” atomic-scale features on the surface [21]. Indeed, the controller can drive the lateral displacement of the tip, while the z motion of the latter follows the surface profile and drives accordingly the z position of the force-feedback device. In this way, the user can navigate the surface having the impression of touching it, since microscopic forces are amplified to a level of sensibility. An example is reported in Fig. 2.2, in which the STM image of a $\sim 30 \text{ nm}$ thick sputtered gold film is

shown (a), next to a plot of the haptic device vertical response as a function of the tip lateral displacement, driven by the operator (b). A similar system for atomic-

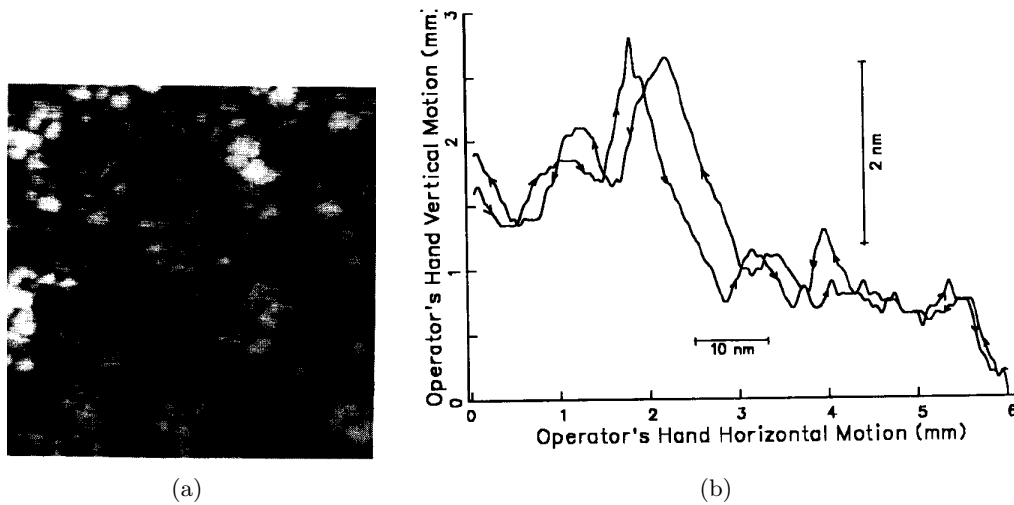


Figure 2.2. (a) STM image of sputtered gold surface in air ($100 \times 100 \text{ nm}^2$). (b) Haptic device vertical feedback motion as a function of the lateral user hand motion navigating the gold surface. Length bars refer to the tip motion; hysteresis is typical of STM piezoelectric actuators. Taken from [21].

scale tele-operation integrates a force-feedback manipulator arm as the haptic tip controller and a head-mounted display for the surface topography visualization [22]. This nanomanipulator, shown in Fig. 2.3, provides an immersive virtual environment where the user is given the ability to act at the atomic scale. The surface below the STM is sampled, graphically reconstructed, lighted and rendered at human scale in the stereoscopic head-mounted display. The viewpoint on the surface follows the user head motions and his control gestures on the haptic arm, while the surface height map data is continuously streamed by the STM tip moving back and forth. Independently and asynchronously, the viewer can “fly” over the surface, scale it up and down, rotate it to any orientation to expose surface details to the directional illumination. In addition, smaller regions of interest can be selected for rapid examination (a scan of the whole surface takes $\sim 33 \text{ s}$ since the tip velocity is constrained). As for the version of atomic-scale tele-operator already discussed, the functions of the force-feedback arm go beyond the mere sensing. Indeed, it serves also as an effector for the interactive modification of the surface. By acting on the haptic controller, the user can move the tip directly over the surface and, with a hand trigger, select locations to fire bias pulses, modifying the surface. Fig. 2.4 shows the example of gold mounds deposited onto a surface from the STM tip.

2.2 AFM-based nanomanipulator

In the wake of the pioneering works just mentioned, the field of tele-nanorobotics shifted towards the use of the atomic force microscope [23, 24], which offers the advantage of being more suitable than STM for a wider range of samples. In addition

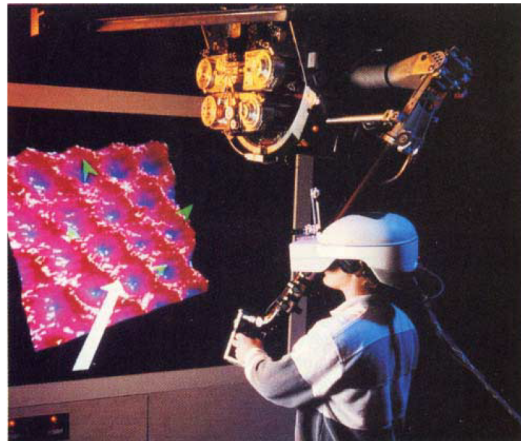


Figure 2.3. Nanomanipulator integrating the STM and a force-feedback arm through a virtual user interface. The haptic arm controls the action of the STM tip, allowing the user both to feel the surface contours and to actuate bias pulses to modify the surface. The reconstructed sample profile is rendered on the head-mounted display. Taken from [22].

to conductive or semi-conductive samples, AFM can also scan non-conductive surfaces, since the topographic profile results from inter-atomic force measurement. Moreover, AFM can be operated in liquid [43–46] and even applied to biological samples like cells and macro-molecules. It can serve as a manipulator as well, although few simple mechanical tasks can be performed, like pushing and pulling particles on a substrate [47–49]. Before the invention of this AFM nanomanipulator, AFM-based manipulations of biological molecules, such as DNA [50–52] or chromosomes [53], were crude and not well controlled. Connecting a force-feedback device to the AFM mechanism allows the user to feel the molecules under investigation, with constant control on the normal force. Indeed, AFM direct force measurement provides a more reliable haptic feedback respect to STM-based manipulators. Sensing the sample is further favored by displaying a 3D topographic reconstruction either on stereo glass or a head-mounted virtual reality display. The integration of this visual tool makes the interpretation of height map data much more intuitive than in the ordinary bi-dimensional display (*i.e.* top view).

As shown in Fig. 2.5, the AFM working principle relies on a very sharp tip, mounted at the end of a flexible cantilever, which scans the sample [54]. As the tip follows the surface profile, the topographical features of the latter deflect the cantilever. Such deflections are usually recorded by an optical lever system, converted back into topography by a computer and displayed on a screen. Atomic resolution can be obtained with this instrument as well [55]. The AFM may be operated in two distinct modes: contact mode or tapping mode (*i.e.* intermittent contact). When working in contact mode, the tip is continuously touching the sample, on which significant normal and lateral forces may be exerted. When using tapping mode, in contrast, the cantilever is oscillated vertically as it scans over the surface. Hence, the tip touches the sample only intermittently and lateral forces are nearly eliminated. A feedback loop keeps either the normal force or the cantilever amplitude constant, in order to measure the surface topography. The nanomanipulator takes advantage of

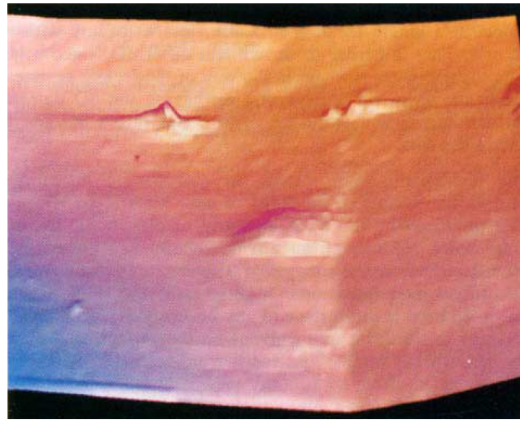


Figure 2.4. Gold surface with some gold mounds deposited over from the STM tip applying bias pulses. Taken from [22].

the crucial difference between these two modes, which it uses for different purposes. The sample can be manipulated in contact mode with controlled normal and lateral forces and it can be imaged in tapping mode before and after the manipulation without further modifications. In tapping mode, indeed, the cantilever is vibrated around its resonance frequency and by an amplitude equal to its separation distance from the substrate. As the tip taps to the substrate, the inter-atomic forces change the vibration amplitude and frequency. By detecting these changes and controlling the sample-cantilever vertical position during scanning, the surface image is yielded. This method is particularly well suited to scan soft samples with few deformations. Depending on the cantilever, forces ranging from a few aN [56] to several tens of μN can be measured in both the normal and the lateral direction. The nanomanipulator can be used in either the imaging mode or the manipulation mode. In the imaging mode, the user does not control the microscope tip, but he merely exploits the haptic system to feel the reconstructed surface, which can be moved, rotated and zoomed in and out for deeper analysis in the virtual environment. Conversely, in the manipulation mode the user controls the tip, which can be moved over the surface in order to manipulate objects on it. This task can be carried out in different ways. A possibility is to carefully position the tip next to the sample in order to apply controlled lateral forces in contact mode, while the normal force is kept constant. The user can also apply normal forces to the sample, while the lateral position is kept constant. In this last case, the tip is placed on top of the sample by using the haptic feedback, and it is then pushed into and retracted from the sample. Moreover, the tip can be moved unrestrained in three dimensions. This strategy allows the free transfer of molecules from one location to another, or force measurements in the lateral and normal directions.

Going from macro- to nano-world, besides the reduction of length scales, forces of different type are affected by different scaling effects, each one with its own scaling factor. Since electrostatic force is not affected by the length scaling, it is dominant with respect to other forces, for example inertia. When scaling nano-forces and positions up to the macro-world, two main approaches are available: linear and nonlinear scaling. In the former, all forces are scaled in the same way such that the

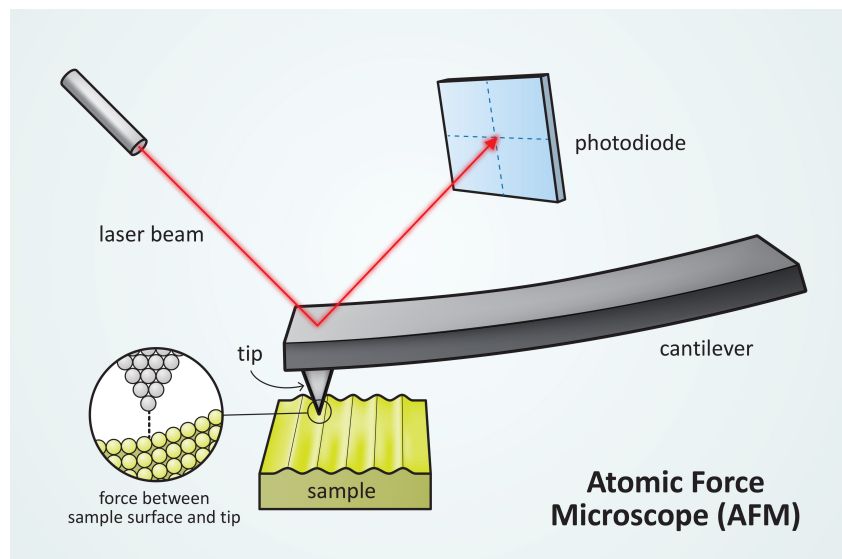


Figure 2.5. Sketch of the AFM working principle. A sharp tip follows the sample profile and bends the flexible cantilever it is attached to. The cantilever deflection is measured by an optical detection system and used to reconstruct the surface topographic map.

inertial forces cannot be felt. In the latter, also called impedance scaling [57], forces are scaled independently. In this last approach, the inertial forces can be magnified such that the operator can feel close to its daily experience. However, this solution requires precise environment parameters, while the linear scaling does not.

By use of this nanomanipulator integrating an AFM, a haptic device and 3D topographic reconstructions for visual feedback, it is possible to scan and manipulate strands of DNA, nanotubes, and other macro-molecules that lie on a surface. Fig. 2.6 shows a sample of InAs quantum dots (a) scanned along the white dashed line [23]. The macroscopic tactile feedback (solid line) is also plotted with the linearly scaled tip motion (dotted line) as a function of time (b). The upward jumps stand for the InAs dots, which are assumed to be fixed on the substrate. Another example of application on inorganic samples concerns the study of the mechanical properties of carbon nanotubes (CNT) [24], which are simple graphite sheets seamlessly wrapped into a tube shape. Many of such tubes can also be arranged in a coaxial structure, known as a multiwall CNT (MWCNT). CNTs are a material with remarkable mechanical properties, mainly due to their unique shape and the fact that the carbon-carbon bond is the strongest bond in nature. They are both very stiff (require large force per unit deformation) and very flexible (able to withstand large deformation without damage). In this respect, the nanomanipulator can be used to study such properties by bending CNTs on surfaces. As shown in Fig. 2.7, a CNT is repeatedly bent to large strain with no permanent distortion of the tube topography. Despite the bending forward, backward, and then forward again (A-D), the tube in the final image appears to be undamaged. The AFM can also measure frictional forces between two contacting surfaces in relative motion by pushing and manipulating MWCNTs on surfaces. As one-dimensional systems, CNTs represent an interesting subject of study even for their electrical properties [58,59],

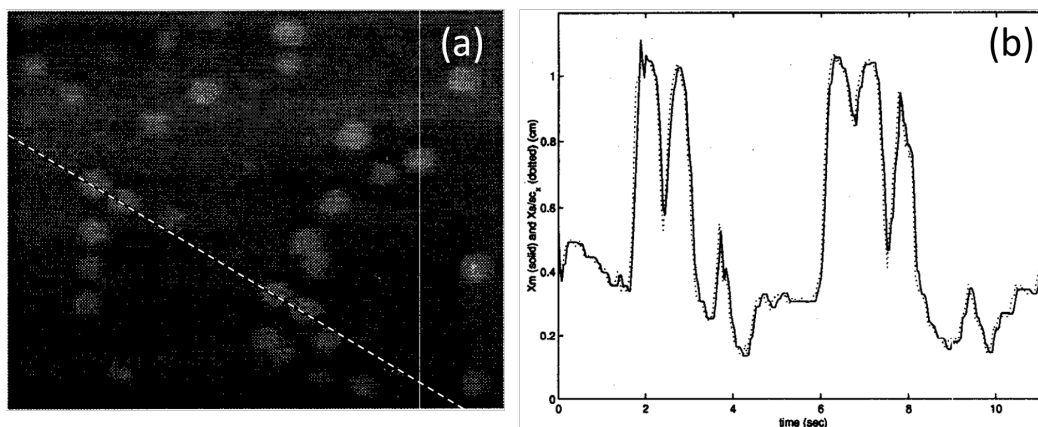


Figure 2.6. InAs quantum dots are scanned along the white dashed line (a); the macroscopic tactile feedback (solid line) is plotted with the scaled tip motion (dotted line) as a function of time (b). Taken from [23].

with the aim of developing advanced electrical devices. In this respect, the AFM tip can be used to interact mechanically, and hence electrically, in a highly localized area, in order to examine how the mechanical strain of a CNT affects its electrical behavior [60].

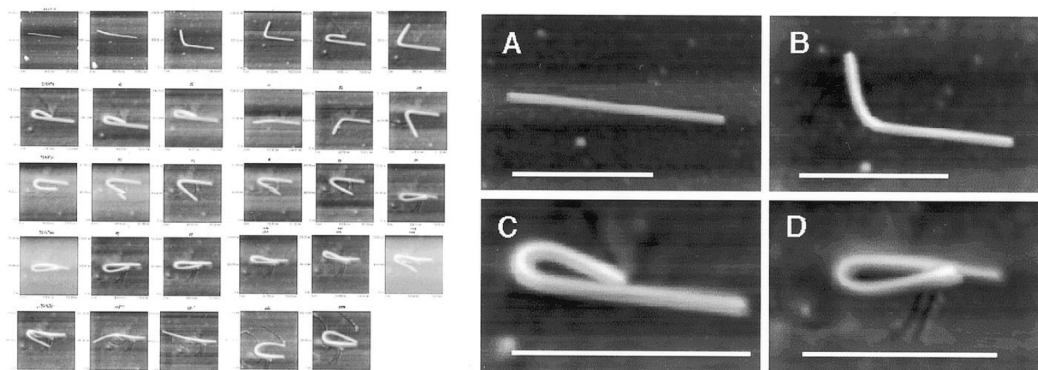


Figure 2.7. Carbon nanotube in highly strained configuration. The sequence on the left depicts the entire AFM-based manipulation process, the enlarged views on the right show some meaningful passages. From its original shape (A), the tube is first bent upward (B) until it bends back onto itself (C). Then it is bent back onto itself in the opposite direction (D). White scale bars are 500 nm. Taken from [24].

As mentioned before, the great step AFM moves respect to STM is the possibility of studying also non-conductive materials like biological samples. Fig. 2.8 shows the AFM-based manipulation of a fragment of DNA. This nanomanipulation strategy allows to directly measure the DNA rupture force for the first time, providing results in good agreement with other more indirect experiments [61]. A further example of application is the measurement of rupture forces and mechanical properties of fibrin fibers, the major structural components of blood clots. Fig. 2.9 reports the images of two fibers before (a,d) and after (b,e) the manipulation, during which a lateral force is applied to the fiber until it ruptures. The respective lateral force traces (c,f)

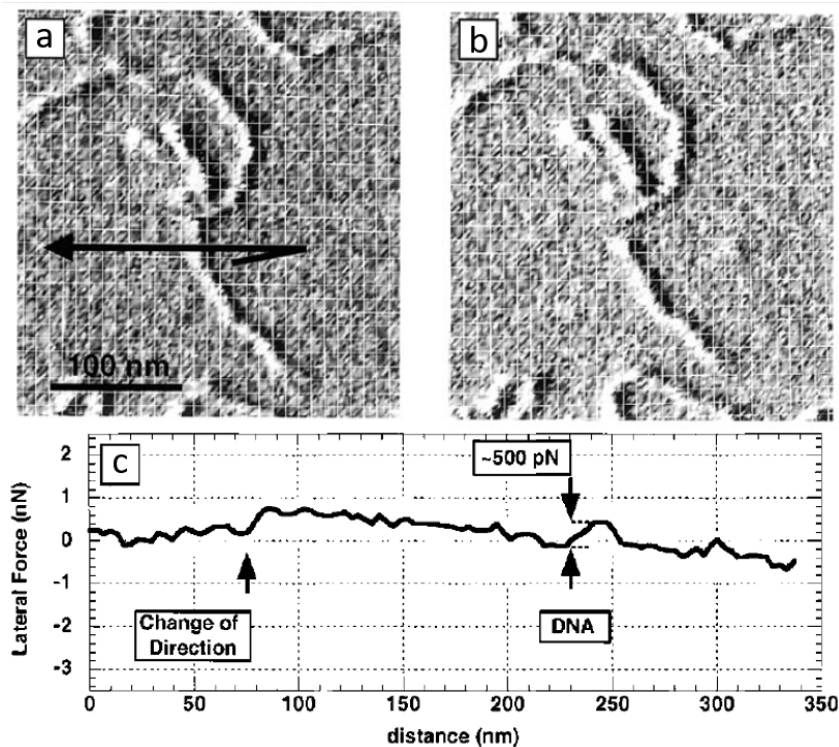


Figure 2.8. DNA fragment before (a) and after (b) it has been manipulated with the scanning tip. The dark arrow indicates the path of the manipulation. The rupture force (~ 500 pN) is deduced from the lateral force versus the distance traveled by the tip (c). Taken from [24].

show two steps and two peaks. The steps are due to a reversal in the direction of tip travel (*i.e.* from left to right and then from right to left) and correspond to the friction between the substrate and the tip itself. The two peaks, instead, contain information about the mechanical properties of fibrin. By comparing the images with the lateral force traces, it can be deduced that the first peak occurs when the tip contacts the fiber and partially detaches it from the surface. As the tip continues its travel, the fiber becomes taut again and is being stretched out. At this point, the force again increases rapidly until the rupture point is reached. From such curves, the rupture force of human fibrin is determined. Furthermore, the manipulation depicted in Figs. 2.9(d) and (e) suggests that the deformation in the fibrin fiber is at least partially elastic. The fiber was initially bent further than the bend in (e), as proved by the scratch left by the tip in the surface (white arrow). The fiber moved then back toward its straight configuration due to a restoring force. The last example we report is the measurement of normal forces applied on Adenovirus particles in order to characterize their elastic properties. Fig. 2.10, showing three virus particles before (a) and after (b) the manipulation, also proves the reliability of the tip placement system.

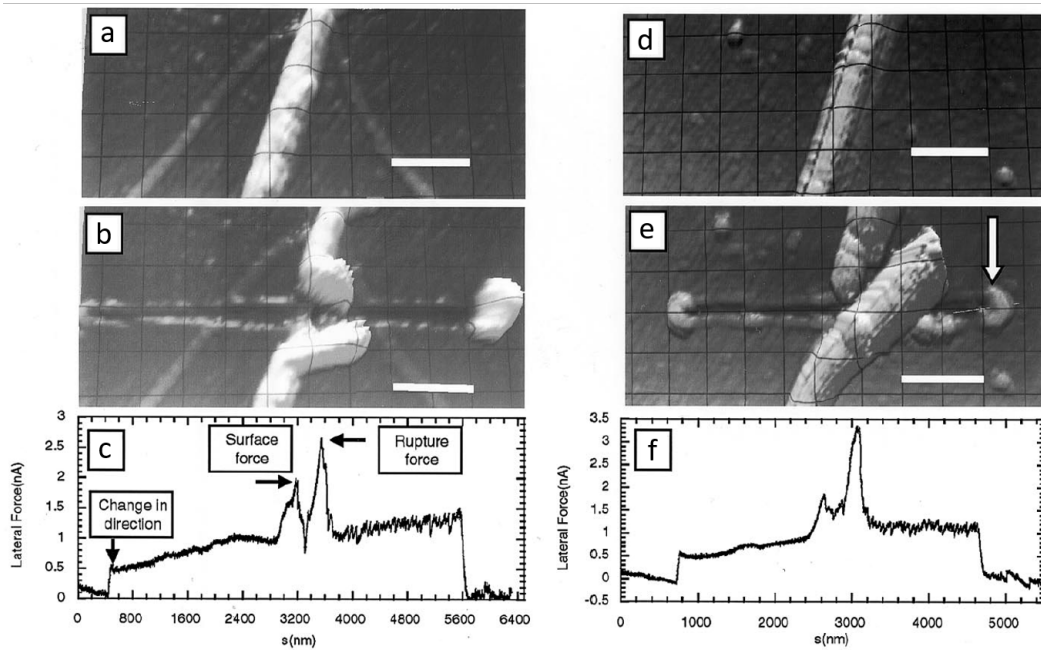


Figure 2.9. Two fibrin fibers before (a,d) and after (b,e) being laterally manipulated by an AFM tip. Their rupture forces can be deduced from relative lateral force traces (c,f). The fiber in (e) shows elastic deformation, trying to restore its original configuration after maximum deformation by the tip (white arrow). White scale bars are 1000 nm. Taken from [24].

2.3 Limitations and perspectives

Both the STM-based and AFM-based nanomanipulator represent an important step forward in the field of interactive tele-operation of micron- and nano-sized samples. However, in both cases the use of a scanning tip involves some unavoidable drawbacks.

- First of all, imaging and manipulation cannot be simultaneous, since they share the same tip and this can be used only for one of the two tasks at a time.
- Secondly, the 3D reconstructions are limited to topographic surfaces, preventing applications to objects that float and move in a 3D space.
- Moreover, such reconstructions are too slow for a true real-time view of the sample.
- In addition, the manipulation task is limited to “pushing with the tip”, and although more complex operations could be performed using two tips for grabbing, this is slow, cumbersome, and invasive [25].

In this PhD project, we design a novel strategy to tele-micromanipulation that is fully based on optical tools for the simultaneous 3D visualization and real-time manipulation of micro-systems through an immersive virtual reality interface. In particular, holographic optical tweezers are in charge of the dynamic manipulation

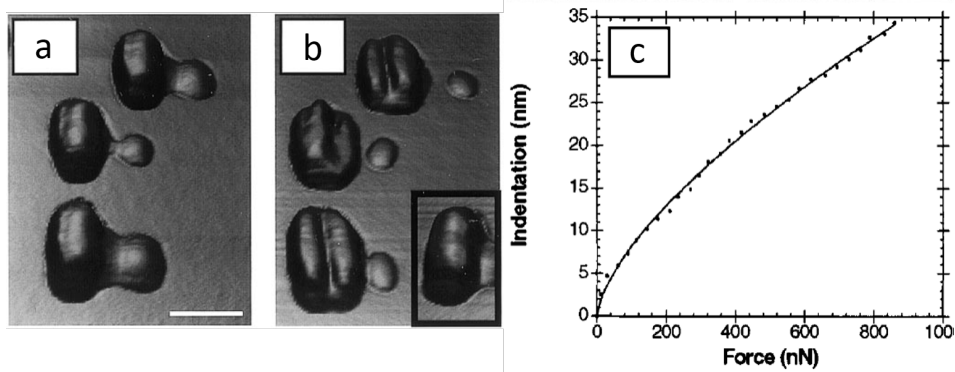


Figure 2.10. Manipulation of Adenovirus particles. AFM images of three viruses before (a) and after (b) force curves are taken. The indentations caused by the manipulation are clearly visible. Inset: Adenovirus particle that was in the same area, but which has not been modified. White scale bar is 200 nm. (c) Plot of the indentation of the virus particle as a function of the applied force (fit: Hertz model of two indenting elastic spheres). Taken from [24].

of 3D many-particles systems, while a 3-axis implementation of digital holographic microscopy technique provides live accurate reconstructions of the sample volume.

Chapter 3

Holographic tweezers

Holographic tweezers allow the 3D manipulation of complex many-particles systems in real time. Developed by integrating Ashkin's optical tweezers [1] with modern digital holographic devices and high-performance computing, this technique can arrange both synthetic and biological particles in custom 3D configurations and move them with negligible time lags. In this chapter we will focus on the principles of optical trapping, to finally discuss the holographic optical tweezers strategy both in its hardware and in its software. Some applications are presented to highlight the power of the technique.

3.1 Principles of optical trapping

Optical tweezers are a technology based on the principle that when a laser beam is tightly focused through a high numerical aperture (NA) objective, the forces arising from light radiation pressure can trap dielectric objects in the nearby of the focus. Any exchange of momentum between light and matter, indeed, results in optical forces. If we simplistically model a propagating beam as a train of light pulses, a single pulse interacting with an object is redistributed asymmetrically in all directions in space. Accordingly, light momentum after interaction with the object has a net component \mathbf{q}_f , generally different in modulus and/or direction from the initial momentum \mathbf{q}_i . By conservation of momentum, the object experiences a force arising from a momentum equal and opposite to the light momentum variation $\Delta\mathbf{q} = \mathbf{q}_f - \mathbf{q}_i$.

Light radiation pressure had already been conjectured in 1619 by Kepler, after some observations of comets tails [62, 63], and it was then formally deduced by Maxwell in 1873 [64] and Bartoli in 1876 [65, 66], independently and through completely different procedures. Nevertheless, only after the invention of laser light by Maiman in 1960 [67, 68], forces of radiation pressure have been employed for practical purposes, namely the manipulation of microscopic objects. As experimentally proved by Lebedew in 1900 [69, 70], despite macroscopic measurements of light radiation pressure were feasible and in quantitative agreement with Maxwell-Bartoli prediction, optical forces were so weak and required such challenging conditions to see some effects that they were practically useless at the macro-scale.

In order to get a more quantitative intuition of the magnitude of such forces [1],

we consider two equivalent expressions for the energy $U_{ph} = h\nu = c_0q$ of a single photon of frequency ν and momentum q in free space, where h is the Planck constant and c_0 is the speed of light. From such relation, we derive the modulus of the photon momentum as $q = h\nu/c_0$. A light beam of power P streams a number of photons per second equal to $P/U_{ph} = P/h\nu$. The corresponding flow of momentum per unit time, having dimensions of a force, is

$$F_{rad} = \frac{h\nu}{c_0} \cdot \frac{P}{h\nu} = \frac{P}{c_0} \quad (3.1)$$

If the beam hits orthogonally a perfectly reflecting mirror M , as in Fig. 3.1, the single-photon momentum variation $\Delta q = 2h\nu/c_0$ results in a total force $F_{rad} = 2P/c_0$ on the mirror. Even if the latter is immersed in a medium of refractive index n , where

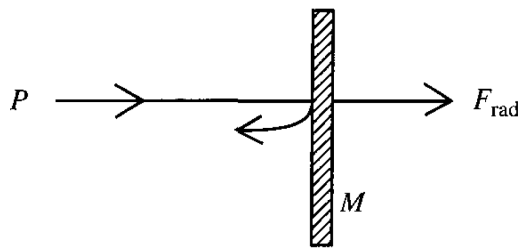


Figure 3.1. Radiation pressure force F_{rad} of a light beam of power P on a 100% reflecting mirror M . Taken from [1].

the momentum flow per unit time is $F_{rad} = nP/c_0$ [64], and is illuminated with a beam of 1 W of power, optical forces would be of the order of few nN, negligible at the macro-scale. The great advantage introduced by Maiman with lasers is the unprecedented degree of coherency of the emitted light. Indeed, coherent laser light can be focused to a diffraction limited spot, in order to concentrate all the available radiation pressure on micron-sized objects. With a mass of the order of 10^{-12} g, such particles can undergo accelerations of $\sim 10^2 - 10^3$ times the acceleration of gravity from powers of about 1 mW, resulting in forces of some pN.

The first experiment showing that radiation pressure forces from focused laser beams can significantly affect the dynamics of microscopic particles was performed by Ashkin in 1970 [1, 71, 72]. In this pioneering work, he used a mildly focused Gaussian beam (wavelength: $\lambda = 0.5145 \mu\text{m}$) of mW of power to illuminate freely suspended polystyrene latex spheres (diameter $\sim 2 \mu\text{m}$) inside a water-filled glass cell. As shown in Fig. 3.2(a), when the laser beam hit a particle, this was not only accelerated in the direction of the incident light as expected, but also simultaneously drawn into the high intensity region on the beam axis. Besides the expected “scattering” force in the direction of the beam, a second unforeseen light pressure force was identified: the “gradient” force, in the direction of the intensity gradient of the beam. As shown in Fig. 3.2(b), a particle stably confined in the beam axis starts wandering around by Brownian motion when the laser beam is turned off, and it is pulled back to the axis when the light is turned on again.

For a deeper comprehension of the meaning of these forces, we consider a plane wave of power P_i and momentum per unit time $F_{rad,i} = nP_i/c_0$, isotropically diffused in space by a particle small respect to its wavelength. After redistribution, the wave

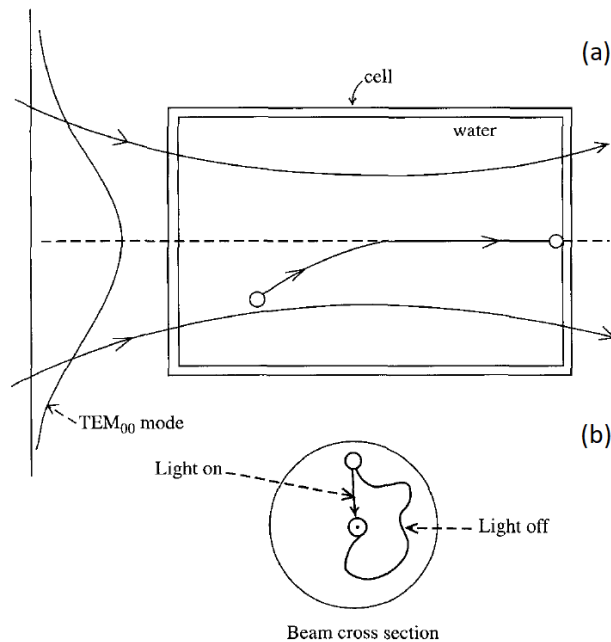


Figure 3.2. First evidence of micron-sized particles manipulated through optical forces. (a) Freely suspended polystyrene latex micro-beads in a water-filled glass cell are guided by a mildly focused Gaussian beam in the direction of the beam and along its axis. (b) Beam cross section depicting stable 2D confinement of a particle in the axis of the beam by light gradient forces. Taken from [1].

has a power $P_f = P_i - \sigma P_i$, where σ is a dimensionless coefficient depending on the scattering cross section. The final momentum per unit time is $F_{rad,f} = n(P_i - \sigma P_i)/c_0$. By conservation of momentum, the quantity $\sigma n P_i / c_0 = F_{scat}$ is a force on the particle arising from light scattering and pointing in the direction of the incident light. Moreover, the wave electric field \mathbf{E} , in first approximation uniform to such a particle, results in an induced dipole $\mathbf{d} = \chi \mathbf{E}$, where χ is the particle susceptibility. Since the energy of a dipole is $U = -\mathbf{d} \cdot \mathbf{E} = -\chi E^2$, the force on this dipole is $\mathbf{F}_{grad} = -\nabla U = \chi \nabla E^2$, directed as the gradient of light intensity.

The particles used for Ashkin's experiment, however, are large respect to the wavelength of light. That's the reason why we can approach the problem in the ray-optics regime to explain the origin of optical forces. As reported in Fig. 3.3, the beam can be modelled as the sum of multiple rays. Each ray hits the sphere with given angle and intensity, according to the Gaussian beam profile. For the sake of generality, we consider a sphere slightly off the beam axis and a pair of typical rays a and b located symmetrically about the center of the sphere. For a sphere of refractive index higher than the surrounding medium, as polystyrene latex spheres in water, ray a hits the sphere and is refracted as shown, apart from minor surface reflections that we can neglect. By conservation of momentum, this gives rise to a force F_a in the direction of the momentum change. Analogously, ray b gives rise to the force F_b . Each of these forces has a forward scattering component in the initial direction of the ray and a transverse gradient component pointing towards the high intensity region of the beam. Since ray a has a higher intensity than ray b , the force

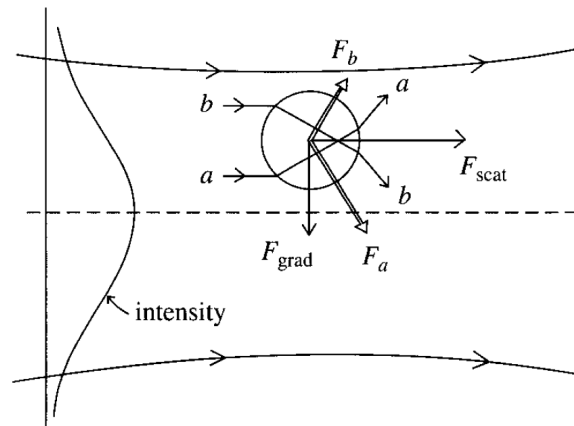


Figure 3.3. Simplified ray-optics diagram of the scattering and gradient force components of the radiation pressure force on a high-index particle, with a diameter large compared to the light wavelength and located off-axis in the near-field of a mildly focused Gaussian beam. The scattering force F_{scat} is in the direction of the beam, the transverse gradient force F_{grad} points towards the maximum intensity region. Taken from [1].

F_a is greater than F_b . Adding all such symmetrical pairs of rays striking the sphere, the resulting net force can be resolved into the two components of the scattering force F_{scat} and the gradient force F_{grad} , obtained by summation of all scattering and gradient components of single-ray forces, respectively. While the net scattering force keeps pushing the particle in the direction of the beam, the net gradient force drives it up to the beam axis, where it cancels out since $F_a = F_b$. This results in a stable bi-dimensional confinement along the beam axis by gradient forces. In order to achieve full 3D confinement, the scattering force needs to be balanced. In this first form of trapping, it cancels out because of the mechanical constraint of the cell wall, while in different versions of the technique the opposing forces were gravity [71, 73], or the scattering force of an equal counter propagating beam [1, 72] (see Fig. 3.4).

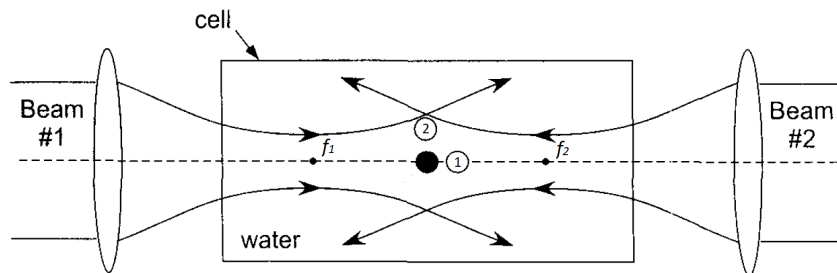


Figure 3.4. First 3D all-optical trap. Two equal counter propagating Gaussian beams perform stable trapping in the system symmetry point (black dot). Restoring forces arise anytime a particle moves along the axis (1: scattering forces unbalance) or out of it (2: gradient forces radially inward). Taken from [1].

The real breakthrough in the field of optical trapping was the invention of single-beam 3D all-optical tweezers [74]. Originally designed as atom traps [75], in 1986 Ashkin decided to try optical tweezers on submicron silica spheres placed in a water-filled glass cell. By use of a single strongly focused Gaussian beam, he

trapped dielectric particles in the size range from $10\ \mu\text{m}$ down to $\sim 25\ \text{nm}$. To this end, the fluid medium surrounding the spheres played a major role, providing partial buoyancy and the viscous damping force essential for a stable trap. Despite the pressure from forward scattering force, proportional to the optical intensity, trapping is feasible thanks to a strong backward axial component of the gradient force. This axial gradient force arises from the high intensity gradient along the beam axis and pulls the particle back towards the high intensity beam focus. In order to get such an axial intensity gradient, the beam needs to be focused through a high NA microscope objective ($\text{NA} = 1.25$), with the entrance pupil (*i.e.* the back aperture) uniformly filled, in order to exploit all the available NA. As depicted in the ray-optics scheme in Fig. 3.5, any displacement of the particle around the focus results in recoil forces also giving stability to the trap. This trapping strategy was then successfully applied also to atoms [76].

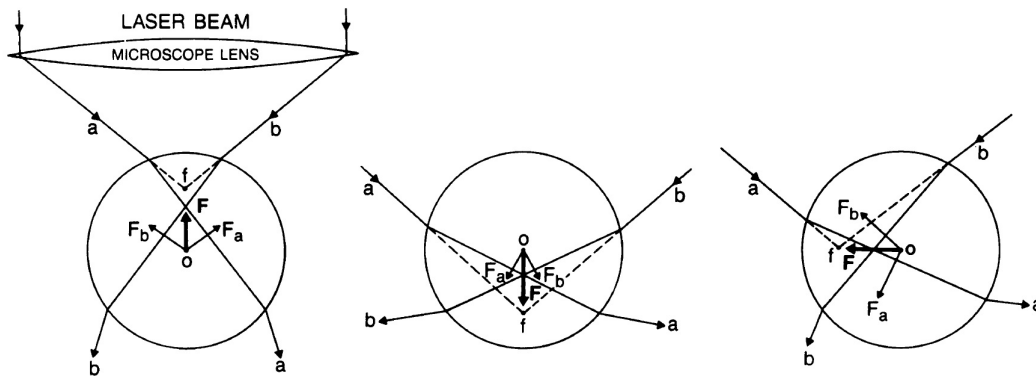


Figure 3.5. Ray-optics picture of the stability of the tweezers trap. Any displacement of a macroscopic sphere away from the focus f , either axially (left, center) or transversely (right), results in a net restoring force \mathbf{F} . Taken from [77].

Since electric fields near the focus of high NA beams are no longer transverse and have very large axial components, a rigorous description of such fields is quite complex and requires the full Maxwell vector wave equation. It is then much simpler and still physically correct to use a ray-optics approach to the problem, for particles large compared with the wavelength λ . The incident beam can be modelled as the sum of many rays, each one with given intensity, direction, and polarization. A ray of power P in a medium of refractive index n applies on the particle a force

$$F = Q n \frac{P}{c_0} \quad (3.2)$$

where the dimensionless factor Q accounts for the momentum transferred to the particle in unity of nP/c_0 . Each of these forces can be resolved into the scattering and gradient components, in the direction of incident ray and orthogonal to it, respectively. The sum of all scattering and gradient single-ray contributions results in the net scattering and gradient forces of the beam.

As a first step to compute these forces, we consider the situation reported in Fig. 3.6, where a ray of power P hits a dielectric sphere at angle θ [77]. By neglecting diffraction, the total force on the sphere results from the contributions of

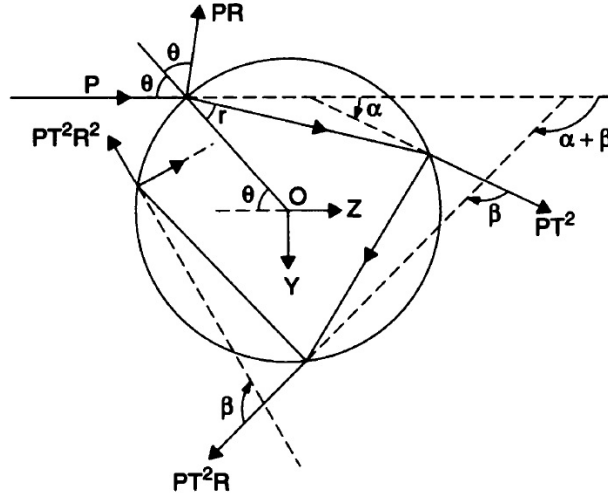


Figure 3.6. Geometry of the scattering of a single incident ray of power P by a dielectric sphere. The optical force results from contributions of reflected ray (PR) and infinite set of refracted rays (PT^2R^l). Taken from [77].

the reflected ray, of power PR , and the infinite set of refracted rays, of decreasing power PT^2 , PT^2R , ... , PT^2R^l , ... (R and T are the Fresnel reflection and transmission coefficients, respectively). The angles between these rays and the incident ray direction are $\pi + 2\theta$, α , $\alpha + \beta$, ... , $\alpha + l\beta$, ... , respectively. The y and z components of the total force result from the momentum-per-second change along those directions:

$$F_z = \frac{nP}{c_0} - \left[\frac{nPR}{c_0} \cos(\pi + 2\theta) + \sum_{l=0}^{\infty} \frac{nP}{c_0} T^2 R^l \cos(\alpha + l\beta) \right] \quad (3.3)$$

$$F_y = 0 - \left[\frac{nPR}{c_0} \sin(\pi + 2\theta) + \sum_{l=0}^{\infty} \frac{nP}{c_0} T^2 R^l \sin(\alpha + l\beta) \right] \quad (3.4)$$

In order to explicitly solve the two summations, we have to consider the total force in the complex plane as $F_{tot} = F_z + iF_y$. Thus, the summation becomes a complex geometric series:

$$\sum_{l=0}^{\infty} R^l e^{i(\alpha + l\beta)} = e^{i\alpha} \left[\frac{1}{1 - Re^{i\beta}} \right] \quad (3.5)$$

We can now rationalize the complex denominator and take the real and imaginary parts of F_{tot} as F_z and F_y , respectively. Knowing that $\alpha = 2\theta - 2r$ and $\beta = \pi - 2r$, where r is the angle of refraction of the ray, leads to [78, 79]

$$F_z = \frac{nP}{c_0} \left\{ 1 + R \cos 2\theta - \frac{T^2 [\cos(2\theta - 2r) + R \cos 2\theta]}{1 + R^2 + 2R \cos 2r} \right\} = F_{scat} \quad (3.6)$$

$$F_y = \frac{nP}{c_0} \left\{ R \sin 2\theta - \frac{T^2 [\sin(2\theta - 2r) + R \sin 2\theta]}{1 + R^2 + 2R \cos 2r} \right\} = F_{grad} \quad (3.7)$$

These relations stand for the scattering and gradient components of the force a single ray applies to the particle and they are exact, since all contributions by

reflected and refracted rays are counted. Moreover, they also consider the ray polarization state through the R and T coefficients. Fig. 3.7 reports the expected values of the scattering, gradient and total force (through coefficients Q_s , Q_g , and $Q_{tot} = \sqrt{Q_s^2 + Q_g^2}$, respectively) for a single ray hitting a dielectric sphere at angle θ (the ray polarization is taken as circular and the sphere effective refractive index n^* , defined as the ratio between the refractive indexes of the sphere and the surrounding medium, is 1.2). It is clear that the gradient force is maximum for $\theta = \theta_{max} \approx 70^\circ$, while for $\theta < \theta_{max}$ it is $F_{grad} > F_{scat}$ almost everywhere.

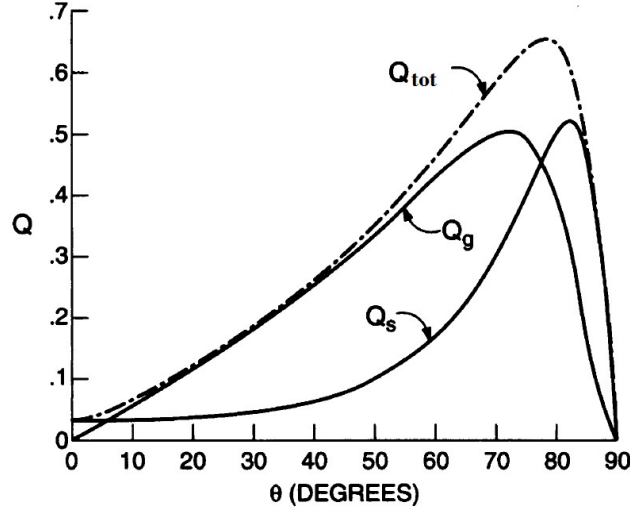


Figure 3.7. Values of the scattering force (Q_s), gradient force (Q_g), and total force (Q_{tot}) for a single ray hitting a dielectric sphere of effective refractive index $n^* = 1.2$ at angle θ . Taken from [77].

The total scattering and gradient forces of the beam result by adding all single-ray contributions. We consider the general case of a beam focused to an arbitrary point f in the vertical plane yz (see Fig. 3.8), at distance S' in $-y$ direction and S'' in $-z$ direction from the sphere origin O . First of all, for a given incident ray the angle of incidence θ needs to be identified, together with the fraction of the ray power in the σ and π polarizations, orthogonal and parallel to the plane of incidence respectively. We consider a ray entering the input aperture of a lens at a distance r from the axis and with azimuthal angle (respect to the y axis) β in the first quadrant. The ray on leaving the lens stays in the vertical plane $AWW'B$ and heads toward f , hitting the sphere at V . The extension of the incident ray beyond f intersects the xy plane at point P at angle α . The plane of incidence for this ray is the plane POV . We see from Fig. 3.8(b) that the knowledge of S' , S'' , α and β leads to the geometrical computation of angles β' and γ' from the following relations:

$$\tan \beta' = \frac{S' \sin \beta}{S' \cos \beta + S'' / \tan \alpha} \quad (3.8)$$

$$\cos \gamma' = \cos \alpha \cos \beta' \quad (3.9)$$

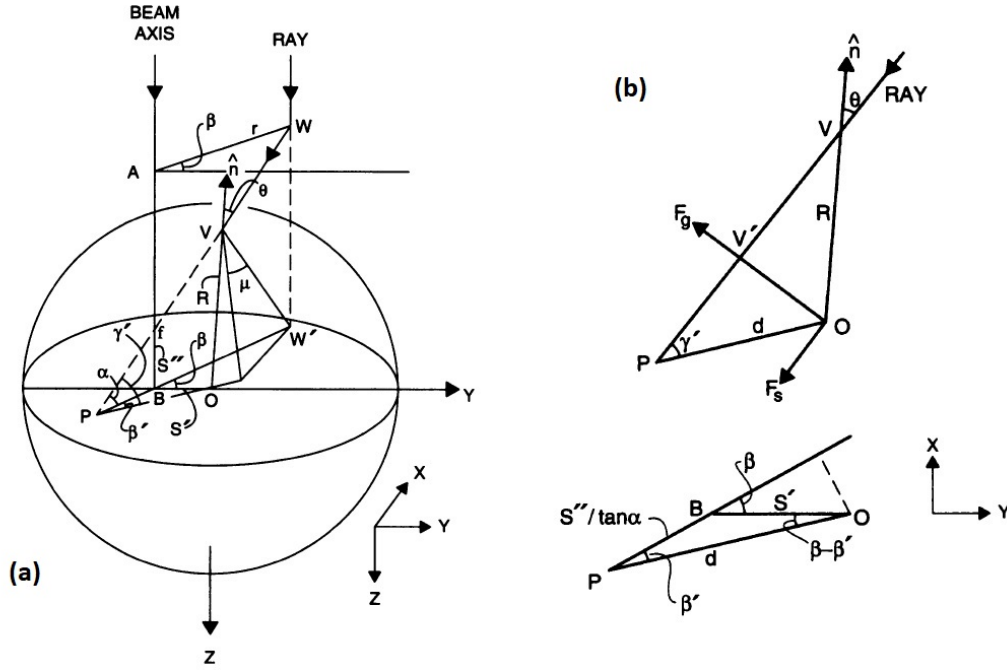


Figure 3.8. (a) Ray-optics geometry of a ray of a beam focused in a generic point f in plane yz . (b) Detail of the plane of incidence POV with directions of scattering and gradient forces of the ray (above) and detail of triangle POB in plane xy . Taken from [77].

We can deduce the angle of incidence from $R \sin \theta = d \sin \gamma'$, where

$$d = \frac{S'' \cos \beta'}{\tan \alpha} + S' \cos(\beta - \beta') \quad (3.10)$$

and the sphere radius R can be set to 1 since in the ray-optics regime it is not important to the resultant forces. On the contrary, the polarization of the incident light plays a major role. The electric field \mathbf{E} of a ray polarized orthogonally to axis y has components perpendicular and parallel to the vertical plane $AWW'B$, respectively

$$\mathbf{E}_{\perp}^{AWW'B} = \mathbf{E} \cos \beta \quad (3.11)$$

$$\mathbf{E}_{\parallel}^{AWW'B} = \mathbf{E} \sin \beta \quad (3.12)$$

These components can be again projected along directions π and σ through the angle μ between the vertical plane $W'VP$ and the plane of incidence POV , given by the relation

$$\cos \mu = \tan \alpha / \tan \gamma' \quad (3.13)$$

For such a polarized ray, the fractions of the incident power p_{π} and p_{σ} for π and σ polarization components are

$$p_{\pi} = (\cos \beta \sin \mu - \sin \beta \cos \mu)^2 \quad (3.14)$$

$$p_{\sigma} = (\cos \beta \cos \mu + \sin \beta \sin \mu)^2 \quad (3.15)$$

Given θ , p_π and p_σ , we can get the scattering and gradient forces components for π and σ directions and sum the results. The scattering force F_{scat} is directed parallel to the incident ray in the VP direction and has components in the z and BP directions:

$$F_{scat,z} = F_{scat} \sin \alpha \quad (3.16)$$

$$F_{scat,BP} = F_{scat} \cos \alpha \quad (3.17)$$

The latter relation can be further resolved as follows:

$$F_{scat,-y} = F_{scat} \cos \alpha \cos \beta \quad (3.18)$$

$$F_{scat,-x} = F_{scat} \cos \alpha \sin \beta \quad (3.19)$$

The gradient force lies on the plane of incidence OPV in direction OV' , perpendicularly to the incident ray. We can resolve also the gradient force along x , y and z axes (see Fig. 3.9). Finally, the global forces along the three reference axes are

$$F_z = F_{scat} \sin \alpha + F_{grad} \cos \mu \cos \alpha \quad (3.20)$$

$$F_y = -F_{scat} \cos \alpha \cos \beta + F_{grad} \cos \mu \sin \alpha \cos \beta + F_{grad} \sin \mu \sin \beta \quad (3.21)$$

$$F_x = -F_{scat} \cos \alpha \sin \beta + F_{grad} \cos \mu \sin \alpha \sin \beta - F_{grad} \sin \mu \cos \beta \quad (3.22)$$

The results obtained for the first quadrant can be extended to other quadrants,

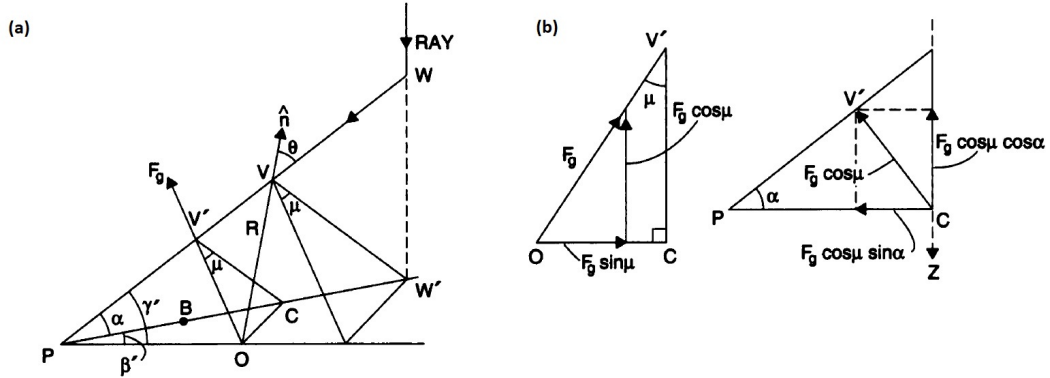


Figure 3.9. Further views of the geometry in Fig. 3.8(a). Taken from [77].

being careful to the correct identification of angles. For symmetry reasons, the contributions from third and fourth quadrant rays along y and z are the same as those from first and second quadrant, while x component cancels out. In order to find the final forces, we only need to double the sum of y and z components of the first and second quadrant.

In Fig. 3.10 the position of the beam focus is mapped to the relative gradient, scattering, and total force on the sphere. The gradient force increases with the particle displacement out of the focus position, acting as the restoring force that gives stability to the trap. The predominant role of the gradient force respect to the forward scattering force clearly emerges from the total force, which remains mostly radially oriented.

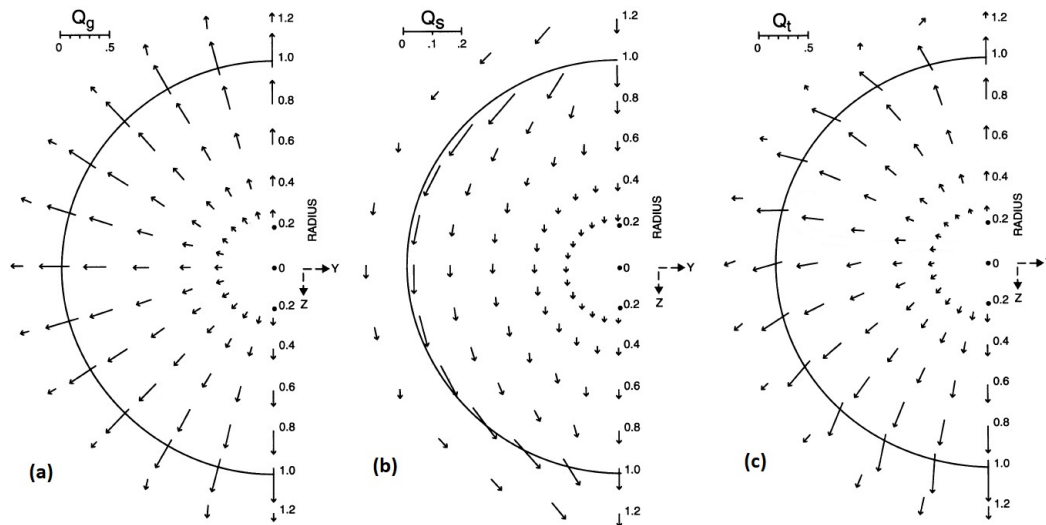


Figure 3.10. Magnitude and direction of gradient (a), scattering (b), and total (c) force as a function of the focus position over the sphere yz section plane, for a circularly polarized trapping beam uniformly filling the objective aperture and a sphere of $n^* = 1.2$. Taken from [77].

3.2 Holographic tweezers: interactive multi-trap systems

Holographic optical tweezers are an upgrade to single-beam optical tweezers able to interactively manipulate complex many-particles systems in 3D. The implementation into the optical tweezers strategy of modern digital holographic devices, operated by high performance computers, allows the real-time generation of dynamic 3D trap arrays around the focal plane.

A single optical trap can be displaced within the objective “focal volume” (*i.e.* the volume around the focal plane) by properly selecting the input beam propagation direction and degree of collimation. We consider a monochromatic plane wave of wavelength $\lambda = \lambda_0/n$ propagating in a homogeneous medium of refractive index n (λ_0 is the wavelength in free space). In a simple scalar approximation, the field can be described through its complex amplitude [80]

$$E(x, y, z) = A(k_x, k_y) e^{i(k_x x + k_y y + k_z z)} \quad (3.23)$$

where $A(k_x, k_y)$ is the complex envelope and the wavevector $\mathbf{k} = (k_x, k_y, k_z)$ of magnitude $k = 2\pi/\lambda$ is parallel to the wave propagation direction. As shown in Fig. 3.11(a), the angles the wavevector makes with the yz and xz planes are, respectively

$$\theta_x = \sin^{-1}(k_x/k) \quad (3.24)$$

$$\theta_y = \sin^{-1}(k_y/k) \quad (3.25)$$

which in the paraxial approximation ($k_x \ll k$, $k_y \ll k$) are small enough to be

approximated as

$$\theta_x \approx \frac{k_x}{k} = k_x \frac{\lambda}{2\pi} \quad (3.26)$$

$$\theta_y \approx \frac{k_y}{k} = k_y \frac{\lambda}{2\pi} \quad (3.27)$$

As depicted in Fig. 3.11(b), a plane wave propagating through an infinity-corrected objective lens with such angles is focused to a bright spot in the lens focal plane, with a lateral displacement from the plane center

$$x \approx \theta_x f \quad (3.28)$$

$$y \approx \theta_y f \quad (3.29)$$

Moreover, a diverging beam focuses along the propagation direction downstream of the focal plane, whereas a converging beam focuses upstream. By the same token, multiple beams simultaneously entering the lens input pupil form multiple optical traps in the focal volume, whose locations are determined by relative angles of incidence and degrees of collimation. This is the principle behind holographic optical tweezers.

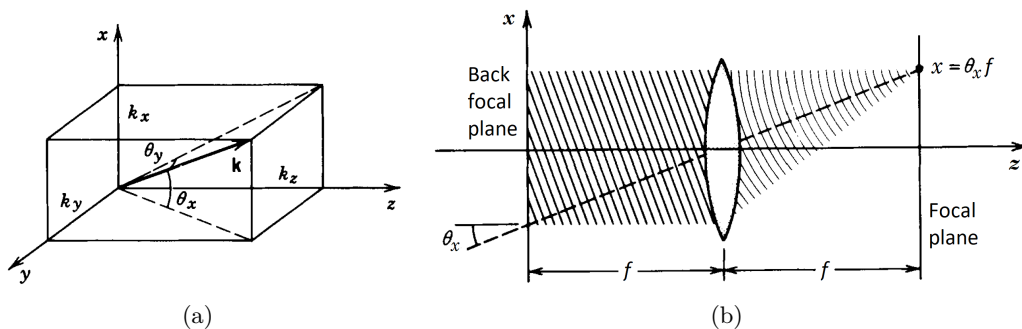


Figure 3.11. (a) xyz reference for the generic wavevector \mathbf{k} . (b) xz -plane section of a thin spherical lens focusing a monochromatic plane wave to a bright spot in the focal plane. In the paraxial approximation, the spot is shifted off the lens axis proportionally to the angle θ_x (f is the lens focal length). Taken from [80].

Two traps can be easily produced using separate steering mirrors and a pair of beam-splitters [81]. In order to create multiple traps, it is possible to time share a single beam either by using a rapid scanning galvo-mirror [82–84] or, for higher speed, acousto-optic beam deflectors [85]. However, neither of these scanning approaches allows simultaneous and easy control of the axial position of the traps, for which holographic tweezers are needed.

Etymologically meaning “*writing of the whole*”, holography stands on the principle that given the structure of a monochromatic electromagnetic field on a plane, the whole 3D structure of the field propagating ahead is uniquely determined [80]. An immediate consequence is that arbitrarily sculpting the wavefront of a plane wave allows to handle the whole 3D structure of the propagated field. A diffractive

beam-splitter can therefore convert a single input beam into several, each of whom forms a separate optical trap.

The tailored modulation to generate a given array of traps in the sample can be deduced from the inverse of the relation mapping the field on the plane of the sculpting hologram to the desired intensity distribution on the target plane. To this aim, Fourier optics provides a smart description of light propagation based on harmonic analysis and linear systems. In particular, a generic wave propagating in a homogeneous medium can be described as the sum of independent plane waves. This conception becomes clear by analyzing the Fourier transform definition of the $z = 0$ cross section of a generic monochromatic field E of wavelength λ paraxially propagating along z :

$$E(x, y, 0) = E_0(x, y) = \frac{1}{4\pi^2} \iint A(k_x, k_y) e^{i(k_x x + k_y y)} dk_x dk_y \quad (3.30)$$

where each pair (k_x, k_y) defines a harmonic contribution $e^{i(k_x x + k_y y)}$ of amplitude $A(k_x, k_y)$ to the global field. As for Eq. 3.23, each of these functions describes a plane wave propagating with angles (θ_x, θ_y) , whose transverse phase profile is 0 or an integer multiple of 2π along lines described by the equation

$$y = -\frac{k_x}{k_y} x + l \frac{2\pi}{k_y} \quad (3.31)$$

where l is an integer [86]. Eq. 3.31 encodes a 2D harmonic function, namely a grating of pitch along x and y axes respectively equals to

$$\lambda_x = 2\pi/k_x \quad (3.32)$$

$$\lambda_y = 2\pi/k_y \quad (3.33)$$

Hence, the propagation of a monochromatic field can be resolved into the propagation of each of the plane waves it is composed of. Moreover, one of the most important Fourier optics results, explicitly derived in appendix A, maps the field in the back focal plane (BFP) of a spherical lens to the field in its focal plane through a Fourier transform (\mathcal{FT}). This relation can be empirically tested for a plane wave (constant function) converging to a bright spot (δ function) in the focal plane. Actually, since we aim at 3D multi-trap configurations around the focal plane, the relation mapping the field in the BFP to its structure around the focal volume is needed. This formula is the same Fourier transform of the field on the back focal plane, with an additional phase term accounting for the beam divergence for axially shifted traps. With the same geometry of Fig. 3.11(b), the field $V(x, y, z)$ in the lens focal volume is [80, 86]:

$$\begin{aligned} V(x, y, z) &= -\frac{i}{\lambda f} e^{i2kf} \mathcal{FT} \left\{ E_0(x', y') e^{-i\frac{\pi z}{\lambda f^2}(x'^2 + y'^2)} \right\} \left(\frac{2\pi x}{\lambda f}, \frac{2\pi y}{\lambda f} \right) = \\ &= -\frac{i}{\lambda f} e^{i2kf} \iint E_0(x', y') e^{-i\frac{\pi z}{\lambda f^2}(x'^2 + y'^2)} e^{-i\frac{2\pi}{\lambda f}(xx' + yy')} dx' dy' \end{aligned} \quad (3.34)$$

where E_0 is the field on the back focal plane of coordinates (x', y') , while the focal volume reference (x, y, z) has origin in the focal plane center. By use of the inverse of Eq. 3.34, a tailored diffractive holographic pattern can be computed for any

given intensity distribution around the focal plane. Such a hologram will then be converted into a diffractive optical element (DOE) in the lens back focal plane.

The hologram design for a single trap displacement is trivial, since the focal location only depends on the phase profile. As a lateral trap shift results from an angular deviation of the beam, the corresponding hologram is a simple blazed diffraction grating phase mask, as Hologram A in Fig. 3.12 [3]. Such a grating diffracts all the incident power into the first order, where the pitch of the grating (see Eqs. 3.32 and 3.33) and its angular orientation set the distance and direction, respectively, of the trap shift from the zero-order. An axial displacement of the trap out of the focal plane, instead, results from a Fresnel lens phase mask as Hologram B in Fig. 3.12. The hologram resulting from the pixel-by-pixel addition, modulo 2π , of a diffraction grating and a Fresnel lens phase masks (see Hologram C in Fig. 3.12) creates a single trap that can be positioned in (x, y, z) .

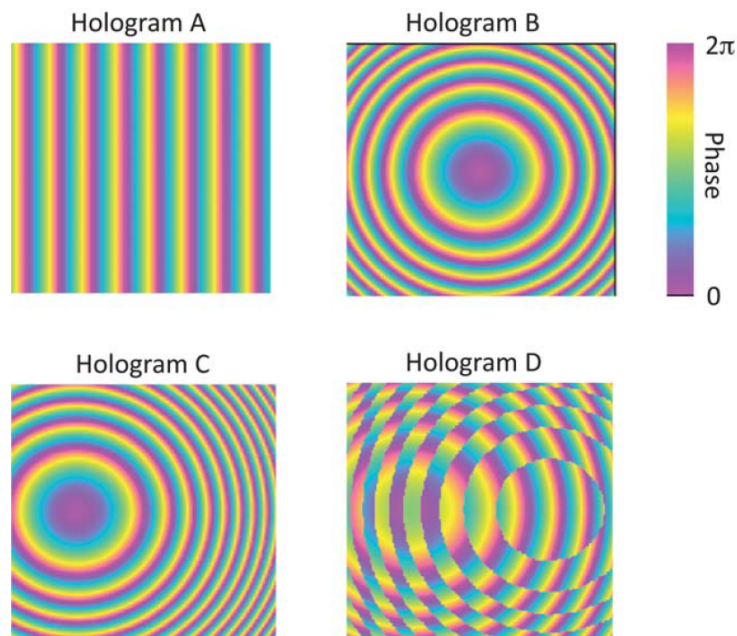


Figure 3.12. Holographic phase masks. A: diffraction grating displacing a single trap along x . B: Fresnel lens displacing a single trap along z . C: addition (modulo 2π) of A and B to displace a single trap in the $(x+z)$ direction. D: complex addition of A and B creating two traps, one displaced in x and the other in z . Taken from [3].

In order to produce multiple traps, the most immediate solution might be the complex addition of single-trap holograms (see Hologram D in Fig. 3.12). However, for large arrays of traps this “gratings and lenses” algorithm fails and more sophisticated methods are needed. Indeed, despite Eq. 3.34 provides a recipe to compute the hologram resulting in the desired intensity distribution upon propagation, such a hologram implies the modulation of both amplitude and phase of the input beam. The required amplitude modulation would remove power from the beam, with catastrophic consequences for the traps efficiency in many cases. Since the computation of a phase-only modulation hologram from a desired intensity distribution has no analytical solution in general, optimized iterative algorithms

were developed to fulfill these requirements (further details in § 3.3).

This holographic trapping strategy was first demonstrated in 1998 using a pre-fabricated commercial DOE [87], while a description of the most common algorithm for creating tailored holograms for optical trapping followed in 2001 [88]. After early demonstrations of the dynamic manipulation of a single particle [89] and of multiple particles with lateral control [90] and also axial control [91], new methods of creating large 3D trap arrays were introduced in 2002 [92, 93]. Here, the DOE was a computer-controlled dynamic spatial light modulator (SLM), a mini-display of liquid-crystal micro-pixels that can sculpt the wavefront of a monochromatic wave with reconfigurable phase masks (further details in § 3.3). Optimized iterative algorithms and modern computing power allow the real-time hologram computation for the interactive manipulation of 3D arrays of traps at the same speed of the SLM refresh rate.

In Fig. 3.13 a schematic representation of a standard holographic optical tweezers (HOT) setup is shown [94]. Just after the laser, a beam telescope expands the beam so that its dimension roughly matches that of the active area of the holographic element, here shown as a reflective programmable SLM. Following the SLM, a second telescope ensures that the beam diameter is appropriate given the diameter of the back aperture of the lens used for tweezing (usually a standard microscope objective lens). In particular, the first lens in this second telescope (Fourier lens) is separated on the one side from the SLM by its own focal length, on the other side from the second lens by the sum of their focal lengths, while the second lens is separated by its own focal length from the back aperture of the objective. With this geometry, this second telescope actually serves four separate roles:

1. it adjusts the beam diameter so to fill the entrance pupil of the objective lens;
2. since a pattern like a simple phase grating on the SLM is equivalent to a steering mirror, the telescope projects the hologram onto the back aperture of the objective lens, thereby ensuring that any beam deflections created by the hologram do not cause the beam to walk off of the entrance pupil of the objective lens;
3. as the hologram and the back aperture of the objective are conjugate image planes, the beam complex amplitude in the trapping plane P is the Fourier transform of its complex amplitude in the SLM plane, as described by Eq. 3.34;
4. since the telescope used is Keplerian, the greater amount of real estate taken up on the optical table respect to a Galilean one allows to perform a spatial filtering in the Fourier plane F . The plane F is conjugate to the focal plane P , so an enlarged image of the trapping pattern is there, where it may be manipulated [95] for example by removing the undeflected zeroth-order spot through a spot block.

In optical tweezers, the strong intensity gradient along the propagation direction is mainly produced by the peripheral rays in the tightly focused beam. For that reason, it is essential to ensure that the input beam delivers significant power to those peripheral rays entering the back aperture of the final high NA tweezing lens.

Therefore, it is very important the second telescope role of matching the beam diameter to that of the entrance pupil of the microscope objective or, in the case of a Gaussian beam, where the intensity of peripheral rays is weak, to slightly overfill the back aperture of the objective.

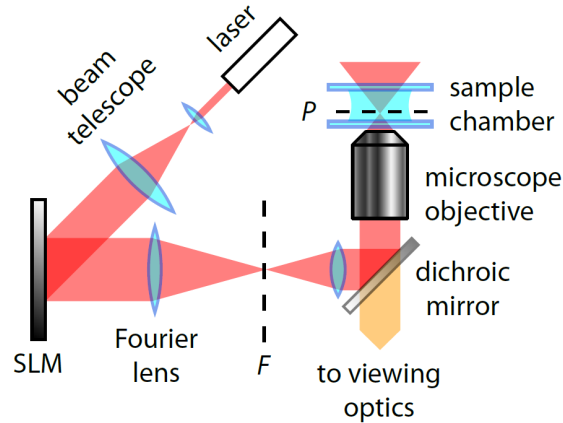


Figure 3.13. Scheme of standard HOTS setup. The beam from a laser is widened in a beam telescope and illuminates a SLM. The diffracted beam is collected by the Fourier lens, which projects in the Fourier plane F the Fourier transform of the complex amplitude of the field in the SLM plane. The remaining combination of lenses, usually including a microscope objective, images the beam in the F plane into the central trapping plane P , which is usually chosen to be in a liquid-filled sample chamber. Taken from [94].

HOTs unique ability to dynamically maneuver multiple traps in 3D was largely employed to precisely arrange multiple colloidal particles or living cells in controlled spatial configurations [96–100], with the opportunity to iteratively study their stochastic behavior following reproducible initial conditions [27, 101], as well as their biological interactions during growth [6]. Using multiple traps it is also possible to grab and rotate microfabricated objects with complex shapes, which can be used as tools for advanced microscopy applications [102, 103], or for the study of Brownian motion and hydrodynamics of non-spherical objects [104, 105].

3.3 Computer generation of digital holograms

The intensity distribution usually required in the sample space of an HOTS setup consists of a set of diffraction-limited bright spots surrounded by darkness. For the sake of efficiency, we need a way to compute a phase-only hologram that uniformly redistributes as much as possible incident power towards the desired configuration of traps in the sample. As mentioned before, since the analytical solution described by Eq. 3.34 does not fulfill these requirements, more sophisticated and optimized iterative algorithms are needed [94]. Some algorithms are fast and therefore particularly well suited to interactive use [106], other algorithms create better traps.

As shown in Fig. 3.14, the field modulated by the SLM in the lens BFP can be discretized on a 2D grid of N pixels, where the j -th pixel coordinates are $(x_j, y_j, 0)$

respect to the SLM center. On the other side of the lens, the field in the volume around the Fourier plane can be discretized on a 3D grid of voxels, where the m -th voxel coordinates are (x_m, y_m, z_m) respect to the Fourier plane center. All the considered algorithms utilize the phase shifts Δ_j^m picked up by the light (of wavelength λ) as it travels from pixel j to trap m . The complex amplitude of the

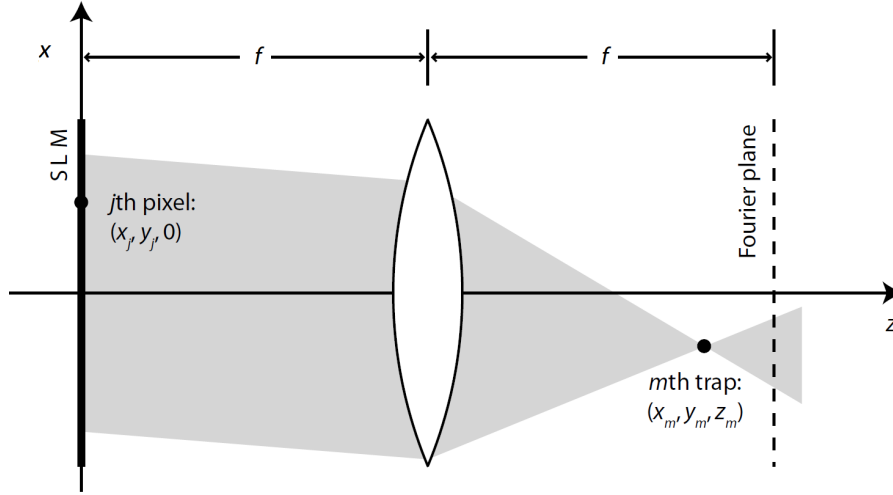


Figure 3.14. Geometry of pixels and traps positions relative to the tweezing lens focal planes. The transverse position of the j -th pixel in the SLM plane is (x_j, y_j) , the position of the m -th trap relative to the centre of the Fourier plane is (x_m, y_m, z_m) . Taken from [94].

electric field at the j -th pixel is

$$E(x_j, y_j) = E_j = |E_j| e^{i\phi_j} \quad (3.35)$$

where ϕ_j is the corresponding phase shift. We can use scalar diffraction theory (Eq. 3.34) to propagate the complex electric field from the j -th pixel to the location of the m -th trap in the image space. By summing up the contributions from all the N pixels, we obtain the complex amplitude v_m of the electric field at the position of trap m :

$$v(x_m, y_m, z_m) = v_m \propto \sum_{j=1}^N |E_j| e^{i(\phi_j - \Delta_j^m)} \quad (3.36)$$

where the phase shifts Δ_j^m are given by

$$\Delta_j^m = \frac{\pi z_m}{\lambda f^2} (x_j^2 + y_j^2) + \frac{2\pi}{\lambda f} (x_j x_m + y_j y_m) \quad (3.37)$$

In order to create a single focus at the position of the m -th trap, these propagation phase shifts allow a trivial computation of the relative holographic pattern. Indeed, we can choose the phase ϕ_j at each pixel of the SLM to cancel out the phase shift as the light propagates from pixel j to trap m , namely $\phi_j = \Delta_j^m$ for all pixels ($j = 1, \dots, N$). In this way, the contributions from all pixels interfere constructively

at the position of trap m , where the intensity is maximum. The normalized field at trap m is

$$V_m = \sum_{j=1}^N \frac{1}{N} e^{i(\phi_j - \Delta_j^m)} \quad (3.38)$$

whose square modulus $|V_m|^2 = I_m$ is the m -th trap normalized intensity. For the single m -th trap hologram, all terms in the sum 3.38 are real and equal to $1/N$, so $I_m = |V_m|^2 = 1$.

For any single trap m there is a well defined configuration of the phase hologram $[\phi_j = \Delta_j^m]_{j=(1\dots N)}$. Whenever a number $M > 1$ of simultaneous traps needs to be created, optimized iterative algorithms are in charge of hologram calculation. The performance of different algorithms can be evaluated in terms of the efficiency e (fraction of overall power in the traps) and uniformity u (measure of how evenly power is distributed between the different traps), respectively defined as follows:

$$e = \sum_m I_m \quad (3.39)$$

$$u = 1 - \frac{\max[I_m] - \min[I_m]}{\max[I_m] + \min[I_m]} \quad (3.40)$$

Some of the most common algorithm strategies will now be presented, whose performance will be evaluated through efficiency and uniformity on a 2D benchmark square grid of 10×10 traps [107].

Random-mask encoding

A very simple and fast approach for creating more than one trap is random-mask encoding [108]. As mentioned before, in the hologram for a single m -th trap all SLM pixel phases are chosen to be Δ_j^m . In this way the propagation phase shift between each pixel and the m -th trap cancels out and all pixels contributions interfere constructively at the trap position. In random-mask encoding, each SLM j -th pixel is matched to a trap m randomly chosen among all the M traps, and the SLM pixel phase is set to the corresponding propagation phase shift Δ_j^m :

$$\phi_j = \Delta_j^{m_j} \quad (3.41)$$

where m_j is a number between 1 and M randomly chosen for each j . The contributions from the fraction of pixels displaying the propagation phase shift corresponding to trap m , and therefore the corresponding fraction of the light illuminating the SLM, interfere constructively at the position of trap m ; the contributions from the other pixels similarly interfere constructively at the positions of the other traps.

This technique is very fast, and performs remarkably well as far as uniformity is concerned. However, the overall efficiency can be very low when M is large. Indeed, on average for each trap m only N/M pixels will interfere constructively, while all the others give a negligible contribution. Therefore

$$|V_m|^2 \approx 1/M^2 \quad \implies \quad e \approx 1/M \quad \implies \quad e \ll 1 \quad \text{when } M \text{ is large.}$$

Numerical results for the benchmark test ($M = 100$) are $u = 0.58$ and $e = 0.01 (= 1/M)$ (see Fig. 3.17).

Still, random-mask encoding is particularly useful to quickly generate either one or a few additional traps on top of a complex light structure obtained via a pre-calculated hologram.

Superposition algorithms

The field immediately after the SLM displaying a single m -th trap hologram is $E_j = |E_j| e^{i\Delta_j^m}$ and propagates to a bright spot at the position of the m -th trap. As mentioned in previous section about Hologram D in Fig. 3.12, the hologram generating multiple bright spots at different traps positions can be computed as the superposition, or complex sum, of individual trap holograms. However, this superposition field cannot be easily created with a phase-only SLM, as the intensity immediately after the SLM is not that of the superposition field. Superposition algorithms neglect this intensity mismatch and use the phase pattern of the superposition field as the phase-hologram pattern [90,91], so

$$\phi_j = \arg \left(\sum_m e^{i\Delta_j^m} \right) \quad (3.42)$$

This algorithm is slower than random-mask encoding (due to the extra N arg function evaluations), but produces useful light distributions with reasonable efficiency but very poor uniformity ($e = 0.29$ and $u = 0.01$ in the benchmark test), as shown in Fig. 3.17. Moreover, a significant part of the energy is diverted to unwanted ghost traps, particularly in highly symmetrical trap geometries [109].

This very simple version of the superposition algorithm can be improved by adding random phases θ_m , uniformly distributed in $[0, 2\pi)$, to each single trap hologram, and therefore to each trap. The phase of the j -th SLM pixel then becomes

$$\phi_j = \arg \left(\sum_m e^{i(\Delta_j^m + \theta_m)} \right) \quad (3.43)$$

This algorithm, usually called Random Superposition [110], has the same computational cost as the previous one, produces similar uniformity but much better efficiency ($e = 0.69$ and $u = 0.01$ in the benchmark test).

When dealing with low-symmetry geometries, holograms calculated using superposition algorithms can also produce good uniformity levels with no further refinement. Although slower than random-mask encoding, the computational speed of superposition algorithms allows for interactive manipulation, mostly when implemented on the computer graphics processing unit (GPU) [111].

Gerchberg-Saxton algorithm

Originally developed for electron beam systems, the Gerchberg-Saxton algorithm [110,112–116] plays a major role even when applied to light, specifically to find a phase distribution that turns a given intensity distribution on the SLM plane into a desired intensity distribution in the trapping plane. In the Gerchberg-Saxton algorithm, the complex amplitude is propagated back and forth between these two planes through Fast Fourier Transforms (FFT) [86], each time replacing the intensity

in the trapping plane with the target intensity and that in the SLM plane with the illuminating laser beam actual intensity profile. This algorithm can be extended to 3D trap geometries where multiple planes are considered for forward propagation. The back-propagated field is then obtained as the complex sum of the corrected and back-propagated fields from the target planes.

When the target intensity is an array of bright spots surrounded by darkness, it is not necessary to calculate the complex field in points whose intensity will be replaced by zero before back propagation. A much faster and more versatile implementation of the Gerchberg-Saxton algorithm for HOTs only computes the field at the trap locations. Through Eq. 3.38, the fields V_m at the traps positions can be calculated from the SLM phases ϕ_j . By weighting the contribution from each SLM pixel with the same factor $1/N$, Eq. 3.38 also effectively replaces the intensity distribution in the SLM plane with the uniform intensity distribution of the illuminating laser beam (it can be generalized to non-uniform illumination intensities). A phase-hologram pattern that takes into account the phases of the field at the traps locations can then be calculated using a superposition algorithm (Eq. 3.43) in which the single-trap holograms are superposed with the relative phase of the corresponding trap

$$\theta_m = \arg(V_m) \quad (3.44)$$

Like all algorithms incorporating the superposition algorithm, the Gerchberg-Saxton algorithm can be speeded up by using the computer GPU [111]. One iteration of this optimized Gerchberg-Saxton algorithm [117, 118] consists of the successive application of Eqs. 3.38, 3.44 and 3.43. It converges after a few tens of iterations. After thirty iterations, the benchmark case results are $e = 0.94$ and $u = 0.60$ [107] (see also Fig. 3.17).

Weighted Gerchberg-Saxton algorithm

Another variation of the Gerchberg-Saxton algorithm, which is biased very strongly towards a uniform distribution of the intensity in the different traps, was derived by introducing the M additional degrees of freedom w_m and maximizing the weighted sum $\sum_m w_m |V_m|$ with the constraint that all $|V_m|$ s are equal. In the corresponding variation of the Gerchberg-Saxton algorithm, the weights w_m^k for the current k -th iteration are calculated from those for the previous $(k - 1)$ -th iteration, w_m^{k-1} , according to

$$w_m^k = w_m^{k-1} \frac{\langle |V_m^{k-1}| \rangle}{|V_m^{k-1}|} \quad (3.45)$$

where $\langle \cdot \rangle$ denotes the average over all trap indices m . Then, the phase hologram is calculated using

$$\phi_j = \arg \left[\sum_m w_m^k e^{i(\Delta_j^m + \theta_m)} \right] \quad (3.46)$$

One iteration of this weighted Gerchberg-Saxton (GSW) algorithm comprises successive application of equations 3.38, 3.44, 3.45, and 3.46. Fig. 3.15 reports the schematic view of GSW algorithm flow chart [96].

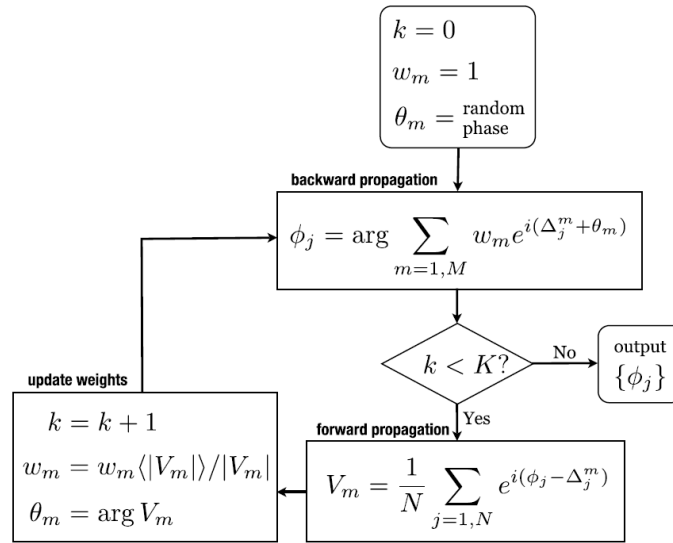


Figure 3.15. Flowchart representing K iterations of Weighted Gerchberg-Saxton algorithm. Taken from [96].

As shown in Fig. 3.16, in the benchmark case this algorithm converges after ~ 15 iterations, with both efficiency and uniformity above 90% after ~ 10 iterations, a speed typical of the Gerchberg-Saxton algorithm. Fig. 3.17 shows the hologram

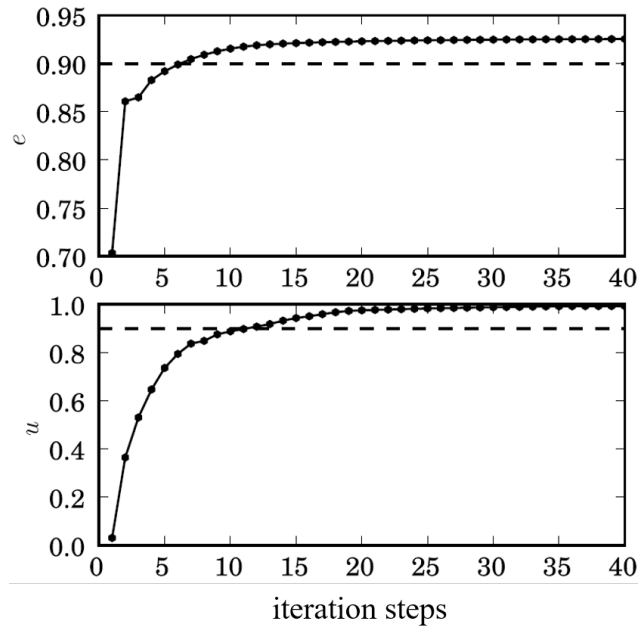


Figure 3.16. Optimization progress for GSW algorithm: efficiency e (top) and uniformity u (bottom) of the 10×10 benchmark square trap grid are plotted as a function of the iteration step. Taken from [107].

produced starting from a random-superposition phase hologram (ϕ_j calculated according to Eq. 3.43) and setting all initial weights to 1 ($w_m^0 = 1$). The final result

has the almost optimal performance of $e = 0.93$ and $u = 0.99$ [107]. The performance of this algorithm remains the highest even for three-dimensional trap arrays.

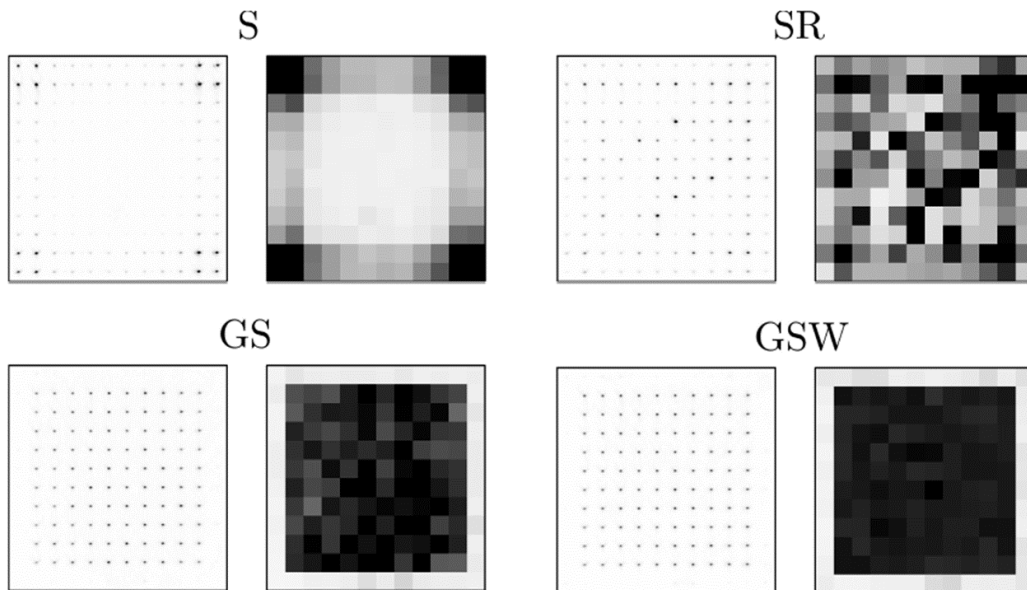


Figure 3.17. Experimental determination of light distribution on trapping plane for the 10×10 benchmark trap grid with Superposition (S), Random Superposition (SR), Gerchberg-Saxton (GS) and Weighted Gerchberg-Saxton (GSW) algorithms. For each algorithm, the negative raw image of laser spots is shown (left), together with a map of the trap energy flow per unit area, represented in the gray level of square tiles centered at the corresponding lattice site (right). Taken from [107].

Computer-controlled Spatial Light Modulator

The holographic phase mask obtained from all the described algorithms is thought to be applied to an incoming beam in the lens back focal plane. After such a modulation, the field propagating through a high NA microscope objective forms the desired array of traps around the focal plane. The simplest and less expensive strategy to display the hologram is through a tailored lithographically-manufactured diffractive optical element [88]. However, the interactive manipulation of many-particles systems is more suitably allowed by reconfigurable holographic devices like programmable spatial light modulators. This technology can dynamically display holograms generating custom arrays of traps, which can be moved with the same speed of the SLM refresh rate. Indeed, successive phase masks can be computed in real-time when optimized iterative algorithms like GSW are implemented on the computer GPU [96].

Different types of SLM [119] are distinguished according to which aspect of light they modulate, which mechanism they use to do this, and whether they work in reflection or in transmission. Most HOT setups integrate phase-only, reflective, liquid-crystal spatial light modulators (LC-SLM). As mentioned before, a phase-only modulation allows the redistribution of input power towards multiple traps with minimum loss. Among the different technologies able to tune the phase of a

light beam, liquid crystals are one of the cheapest and more mature. As elongated birefringent molecules, their optical properties change with their orientation respect to the incident field. Since they re-align in response to an applied voltage, the SLM structure is a 2D array of micron-sized independent electrode pixels spread across the LC layer (see Fig. 3.18). With such a geometry, we can have a pixel-by-pixel control of the output beam phase profile by applying locally-defined voltages.

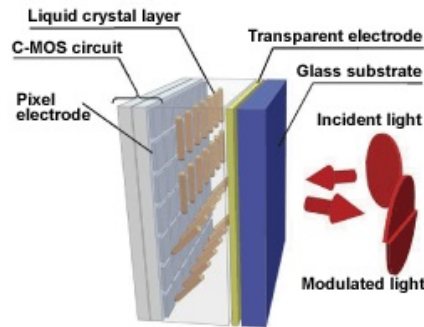


Figure 3.18. Schematic structure of a phase-only, reflective, liquid-crystal spatial light modulator.

The LC character of most SLMs used in HOTs determines many of the SLM properties [120]. Liquid crystals can be either nematic or ferroelectric. Despite ferroelectric LC are significantly faster, they only offer two phase levels, which limits the choice of algorithms for the calculation of the hologram patterns and the diffraction efficiency. This is the reason why HOTs usually exploit nematic LC-SLMs, with a nominal number of 256 available phase levels, between 0 and 2π . The maximum phase delay a LC-SLM can introduce grows with the thickness of its LC layer. Depending on the LC layer thickness, the SLM has a maximum wavelength for which it can achieve a full 2π phase delay; this is often taken as the upper limit of an SLM's specified wavelength working range. Besides, the LC-SLM response time is proportional to the square of the LC layer thickness [121]. This is the reason why reflective SLMs present great speed advantages respect to transmissive ones. Indeed, since light passes through the LC layer twice, its thickness for a required phase delay can be halved.

Due to lack of surface flatness, reflective SLMs usually aberrate the light beam more than transmissive ones. Like the spherical aberration introduced by the objective, this can deteriorate the quality of the traps and limit the trapping range [122]. This sort of aberrations, together with other aberrations in the optics, can be corrected by displaying a suitable phase hologram on the SLM [123–126].

A good compromise between power efficiency and resolution of the traps requires the size of the illuminating Gaussian beam to be properly regulated. On the one hand, the larger the beam, the better use it makes of the active area of the SLM, which in turn means higher resolution of the resulting light pattern in the trapping plane. On the other hand, if the beam is too large, a fraction of the incident power misses the active area of the SLM and is therefore either lost or goes into the zeroth order. Nevertheless, when a SLM is used any significant incident beam power must be properly distributed, so to avoid boiling the liquid-crystal active element,

permanently destroying the device. The standard solution is a beam diameter that is roughly matched to that of the SLM active area.

Chapter 4

Holographic microscopy

Despite holographic optical tweezers allow the live dynamic manipulation of multiple objects in 3D following user input (see § 3.2), the visual feedback we get is typically limited to a 2D view of the sample scene, obtained by bright field or epifluorescence microscopy [10, 102]. In order to achieve a full 3D interactive micromanipulation experience, an imaging technique that is fast enough to provide the volumetric reconstruction of a sample in real time is needed. Obtaining 3D microscopy images over a large volume and with a good resolution ($< 1 \mu\text{m}$) and a high frame rate is of fundamental importance for the analysis of dynamical processes in physics and biology. Most of consolidated techniques for the 3D imaging of micro-systems, such as confocal microscopy [127, 128], 2-photon femtosecond laser scanning microscopy [129], or light sheet microscopy [130], make use of mechanical or optical scanning methods, with strong constraints on the achievable frame rates. An alternative 3D and label-free imaging tool is diffraction tomography, which allows for a 3D reconstruction of the sample refractive index from stacks of 2D frames acquired while changing the illumination angle [12–14, 16, 17] or while scanning the focal plane position along the optical axis [15]. These frames stacks can be acquired with a real-time frame rate; however, diffraction tomography is computationally very intense and consequently too time consuming to be used for real-time visualization of the sample.

We consider as a benchmark case of study the motion of a swimming *E. coli* bacterium, schematically shown in Fig. 4.1. *E. coli* is a bacterium with a rod-shaped

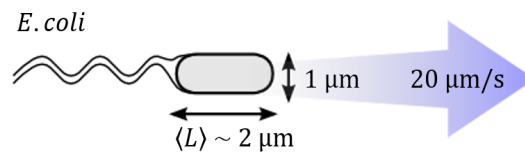


Figure 4.1. Sketch of an *E. coli* bacterium geometric and dynamic data. The cell body is approximately a spherocylinder of average length $\langle L \rangle \sim 2 \mu\text{m}$ and diameter $\sim 1 \mu\text{m}$. The bacterium propels himself at a speed of $\sim 20 \mu\text{m/s}$ by rotating a bundle of flagella.

body, approximately $2 \mu\text{m}$ long and $1 \mu\text{m}$ thick, propelled by a spinning bundle of helical flagella at an average speed of about $20 \mu\text{m/s}$ [131, 132]. A reasonable time resolution for tracking would be such that the cell body is displaced by 1/10 of its size between two successive frames, needing a frame rate of about 100 fps for a single

frame of the order of 500×500 pixels. This requirement has to be combined with a submicron spatial resolution in both transverse and axial direction to allow precise tracking of both position and orientation of the swimming cell. In order to follow the events in a 3D field of view (FOV) measuring about $50 \times 50 \times 10 \mu\text{m}^3$, the needed frame rate for the real-time reconstruction of the whole volume becomes a couple of orders of magnitude higher. The combination of all these requisites rules out the possibility of using microscopy techniques relying on a scan of the focal plane, such as confocal microscopy, which, apart from some advances where 512×512 -pixel plane sections can be acquired at up to 200 Hz [133], offers video-rate frame rates for a single plane [128].

When a very high frame rate is desired, techniques that encode the required 3D information in a single 2D snapshot are the most effective ones, since no scans are involved. In this respect, holographic microscopy allows to numerically retrieve the 3D structure of a scattered field from the intensity fringes resulting from its coherent superposition with a reference beam. The holographic principle behind this microscopy strategy is the same used in HOTs to handle the 3D structure of a propagating beam by modulating its wavefront with a tailored 2D diffractive optical element. In this case, however, it is exploited to deduce volumetric information on the scattering objects by numerical back-propagation of the scattered field encoded in the 2D interference pattern just mentioned. Digital holographic microscopy (DHM) has been proved to be one of the most effective label-free techniques for real-time 3D imaging of micrometer sized objects over a large depth of field and without any mechanical motions [134–139]. We will now discuss the more common in-line geometry, whose main limitations are overcome by a recent implementation by our group that improves a lot the quality of the reconstruction.

4.1 In-line digital holographic microscopy: advantages and limitations

A basic DHM setup consists of an illumination source, an interferometer with microscopic imaging optics, a digital camera, and a computer with necessary programs. In standard in-line (or on-axis) DHM, the condenser stage of a conventional microscope is replaced by a collimated coherent source directed along the optical axis of the objective [135]. As shown in Fig. 4.2, the coherent illumination beam \mathbf{E}_i of wavelength λ interferes on the image plane with the light \mathbf{E}_s scattered by a generic object (*e.g.* a colloidal sphere), giving rise to a fringe pattern (*i.e.* the hologram) that encodes the phase information of scattered light in the intensity I . By direct back-propagation, one can numerically reconstruct the 3D structure of the scattered light from a single two dimensional image, so that the acquisition speed is only limited by the frame rate and the sensitivity of the camera [135, 139–141].

In a coordinate system centered in the image plane, the incident field complex amplitude is $E_i(\mathbf{r}) = |E_i| e^{i\mathbf{k}\cdot\mathbf{r}}$, with $\mathbf{k} = 2\pi n/\lambda [\sin \theta_x, \sin \theta_y, \sqrt{\cos^2 \theta_x - \sin^2 \theta_y}]$, where θ_x and θ_y are the direction angles of the illumination beam, defined by Eqs. 3.24 and 3.25 (see § 3.2), n is the refractive index of the medium inside the sample and $\mathbf{r} = (x, y, z)$. The incident and scattered fields interfere in the image plane

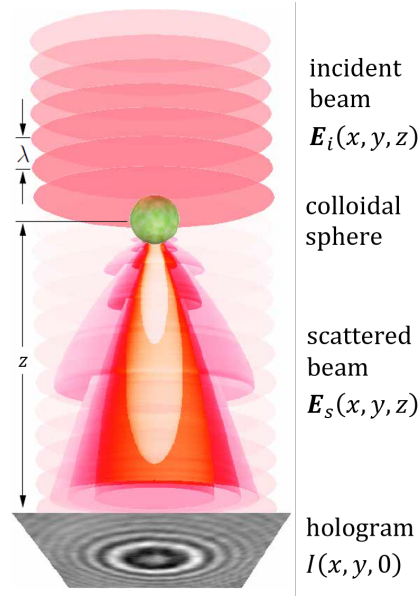


Figure 4.2. Sketch of in-line DHM geometry. The coherent incident beam \mathbf{E}_i of wavelength λ is partially scattered by a micron-sized object (*e.g.* a colloidal sphere). The interference between the unscattered light and the scattered beam \mathbf{E}_s results in a 2D fringes hologram I on the image plane. Taken from [142].

giving rise to the intensity pattern:

$$\begin{aligned} I(x, y, 0) &= |\mathbf{E}_i + \mathbf{E}_s|^2 = |\mathbf{E}_i|^2 + |\mathbf{E}_s|^2 + 2 \Re \{ \mathbf{E}_i^* \mathbf{E}_s \} \approx \\ &\approx |\mathbf{E}_i|^2 + 2 \Re \left\{ |\mathbf{E}_i| e^{-i(k_x x + k_y y)} \mathbf{E}_s \right\} \end{aligned} \quad (4.1)$$

where the second order term in the scattered field can be neglected for weak scatterers, as it is for some synthetic particles and most of biological samples, as well as if it is observed at a distance such that the diverging scattered field becomes small enough. Since $|\mathbf{E}_i|^2$ is the flat intensity pattern obtained with an empty field of view, it can be easily subtracted from Eq. 4.1. As the starting point for back-propagation we then take the field:

$$E(x, y, 0) = \left[I(x, y, 0) - |\mathbf{E}_i|^2 \right] |\mathbf{E}_i|^{-1} e^{i(k_x x + k_y y)} \approx \mathbf{E}_s + \mathbf{E}_s^* e^{i2(k_x x + k_y y)} \quad (4.2)$$

which is proportional to the scattered wave plus its complex conjugate. The latter term, in particular, gives rise to mirror images of the scatterer around the image plane [143, 144]. Such an artifact highlights the two symmetric locations, coincident for vertical illumination, where the object would produce the same pattern on plane $z = 0$.

If the Born approximation is valid (*i.e.* weakly scattering particles), the field $E(x, y, z)$ on a generic plane is given by the convolution between $E(x, y, 0)$ and the Rayleigh-Sommerfeld free space propagation kernel [86, 145]

$$G(x, y, z) = -\frac{1}{2\pi} \frac{\partial}{\partial z} \frac{e^{ikr}}{r} = \frac{z e^{ikr}}{2\pi r^2} \left(\frac{1}{r} - ik \right) \quad (4.3)$$

where $r = \sqrt{x^2 + y^2 + z^2}$ and $k = 2\pi n/\lambda$. In the end, the back-propagated field is

$$E(x, y, z) = G(x, y, z) * E(x, y, 0) = \mathcal{FJ}^{-1} \left\{ \tilde{G}(k_x, k_y, z) \cdot \mathcal{FJ} \{E(x, y, 0)\} \right\} \quad (4.4)$$

where $\tilde{G}(k_x, k_y, z) = \mathcal{FJ} \{G(x, y, z)\}$. In the last passage of Eq. 4.4 we apply the Fourier convolution theorem [80, 86], with whom the back propagated field can be efficiently evaluated in real time through 2D FFT implemented on the computer GPU.

The basic assumption behind DHM is that the reconstructed scattered field has maximum intensity in correspondence of the location of the scattering particles. By reconstructing the wavefront on a number of planes at various distances in the vicinity of the objects, a 3D image can be built up from a single 2D hologram. Dilute samples of spherical particles and solutions of various swimming micro-organisms have been 3D tracked at hundreds of Hz frame rate and at micrometer resolution in thick samples (up to mm) [135, 144, 146]. Notwithstanding these advantages, DHM reconstructions are usually poor in terms of optical axis resolution [143], unless prior knowledge on the scatterer geometry is known [142, 147]. In particular, the reconstructed intensity presents an extended axial focal region that is maximum at a point that appears to be shifted downstream along the beam propagation direction. The position of this maximum represents the focal point of the object acting as a lens, since the light scattered by micron-sized particles has a small angular divergence that results in poor refocusing power upon back-propagation, as shown in Fig. 4.3. When multiple objects are stacked along the optical axis, direct numerical back-propagation, which assumes an optically homogeneous medium, gives rise to insufficient volumetric reconstructions [143]. Moreover, using lasers as the coherent source, the coherent superposition of light scattered by unwanted objects leads to speckle noise and artifacts in the reconstruction. Using partially coherent sources like LEDs suppresses coherent noise [148] but, at the same time, it also reduces fringe visibility deteriorating the axial resolution in numerical reconstructions.

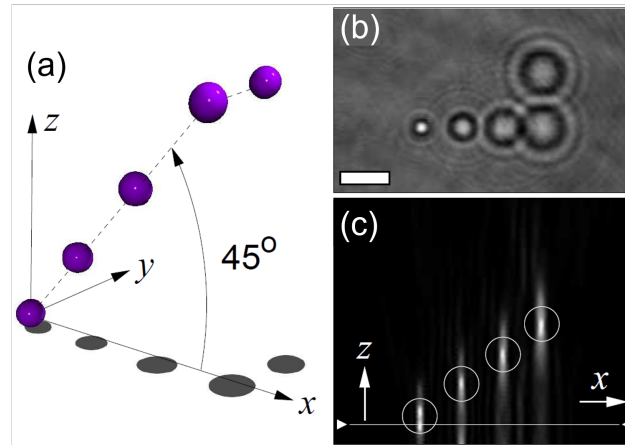


Figure 4.3. Holographic imaging of three-dimensionally arranged $1.5 \mu\text{m}$ silica beads: (a) sketch of the 3D configuration arranged with HOTs; (b) xy -plane hologram of the coherently illuminated beads (scale bar is $5 \mu\text{m}$); (c) xz section of the back-propagated field intensity (circles denote the intended particles coordinates). Taken from [143].

4.2 3-axis holographic microscopy: 3D imaging of swimming bacteria

Some years ago our group introduced an implementation of in-line holographic microscopy that significantly improves the resolution along the optical axis by combination of DHM and simultaneous multi-axis illumination [26]. As shown in Fig. 4.4, the sample is illuminated by three collimated red, green, and blue (RGB: $\lambda_R = 630$ nm, $\lambda_G = 520$ nm, $\lambda_B = 460$ nm) LED beams, forming an angle of approximately 45° with the optical axis and equally spaced along the azimuthal coordinate. As mentioned before, using partially coherent LED sources removes most of the speckle noise due to laser light [149, 150]. However, an extended transverse coherence is still required for a good fringe visibility and can be easily increased, at the cost of illumination intensity, by using iris diaphragms to reduce the numerical aperture of the condenser lenses. Three independent holograms, produced by the standard on-axis interference between the illumination and scattered light, are magnified through a $100\times$ objective-tube lens pair, and acquired by a RGB camera in a single snapshot (the LEDs peak wavelengths match the spectral response of the three color channels of the camera). Each hologram can be back propagated to retrieve the corresponding scattered field suffering from typical poor axial resolution of in-line DHM. However, the overlap of these three independent intensities (I_R , I_G , I_B) returns a volumetric image whose isosurface contours represent quite closely the surface of simple microscopic objects. Moreover, the coherent background noise, which appears to be strongly sensitive to beam wavelength and direction, is also suppressed when overlapping the three reconstructions. Hence, the final 3D intensity distribution resulting from the reconstructed fields overlap is

$$\rho(\mathbf{r}) = \rho(x, y, z) = [I_R(x, y, z) I_G(x, y, z) I_B(x, y, z)]^{1/3} \quad (4.5)$$

where the cubic root ensures that ρ has the dimensions of an intensity. For a more quantitative analysis on the sample, the global intensity volume needs to be segmented and processed. First of all, applying a threshold Γ to ρ converts the image into a binary volumetric image ρ^Γ , where

$$\rho^\Gamma(\mathbf{r}) = \begin{cases} \rho(\mathbf{r}) - \Gamma & , \rho(\mathbf{r}) \geq \Gamma \\ 0 & , \rho(\mathbf{r}) < \Gamma \end{cases} \quad (4.6)$$

For each j -th portion of ρ above the threshold we can find a 3D region of interest (ROI) of arbitrary size. Integrating the intensity volume ρ^Γ in the three directions of space results different from 0 only in ROI locations. Each j -th ROI has an intensity distribution

$$\rho_j(\mathbf{r}) = \begin{cases} \rho^\Gamma(\mathbf{r}) & , \mathbf{r} \in \text{ROI} \\ 0 & , \mathbf{r} \notin \text{ROI} \end{cases} \quad (4.7)$$

Given the ROI intensity distributions ρ_j , they can be individually processed to extract single objects data. In particular, the center-of-mass coordinates $\mathbf{R}_j = (x_j, y_j, z_j)$ of each j -th object are obtained from the first order spatial moment of the 3D intensity distribution inside j -th ROI, namely

$$\frac{\int \mathbf{r} \rho_j(\mathbf{r}) d^3r}{\int \rho_j(\mathbf{r}) d^3r} = \langle \mathbf{r} \rangle_j = \mathbf{R}_j \quad (4.8)$$

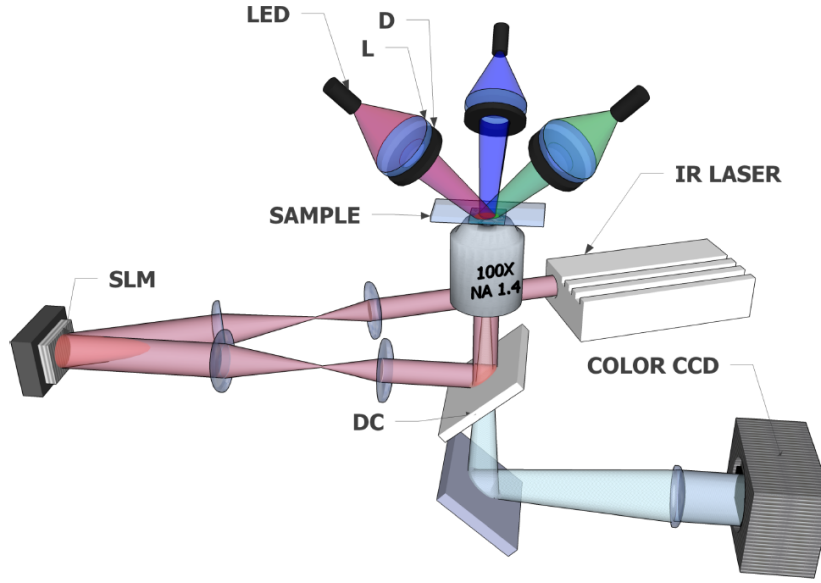


Figure 4.4. Holographic setup. Three RGB LED sources are used for illumination. Light from each LED is collected by a lens (L) and filtered through a diaphragm (D) to enhance the transverse spatial coherence. A RGB color camera acquires the three independent RGB holograms in a single snapshot. The infrared trapping laser (pink beam) is expanded, phase modulated by a SLM, reflected by a dichroic mirror (DC) and sent to the back pupil of a 100× oil immersion objective. Taken from [26].

Moreover, the central second order moments can be arranged in the following 3×3 covariance matrix:

$$\frac{\int (\mathbf{r} - \langle \mathbf{r} \rangle_j) (\mathbf{r} - \langle \mathbf{r} \rangle_j) \rho_j(\mathbf{r}) d^3r}{\int \rho_j(\mathbf{r}) d^3r} = \left\langle (\mathbf{r} - \langle \mathbf{r} \rangle_j)^2 \right\rangle = \langle \mathbf{r}^2 \rangle - \langle \mathbf{r} \rangle_j^2 = \langle \mathbf{r}^2 \rangle - \mathbf{R}_j^2 \quad (4.9)$$

which as a symmetrical matrix can always be diagonalized. The resulting eigenvectors represent the three principal axes of the object body, while the eigenvalues correspond to the object extents along such axes.

As shown in Fig. 4.4, our setup is also equipped with a holographic trapping system based on an infrared laser beam ($\lambda = 1064$ nm) and a LC-SLM, which in combination with our 3-axis holographic microscopy system allows for the simultaneous live 3D imaging and manipulation of microscopic particles.

As a first example testing the performances of this imaging technique, we present the reconstruction of $2 \mu\text{m}$ silica beads in water, trapped at a distance of a few microns above the objective focal plane [26]. Each sphere in the field of view contributes to the global RGB hologram with a fringe pattern like the one reported in Fig. 4.5(a). Red, green, and blue density maps in Fig. 4.5(b) depict the three reconstructed independent intensities, which overlap in small volumetric regions centered at the locations of the four silica beads in the FOV. The beads position and aspect ratio can be computed using the first two spatial moments of the 3D intensity distribution, as described before.

The comparison between Figs. 4.5(c) and (d) highlights the improved axial resolution of 3-axis strategy respect to previous holographic imaging techniques. In

particular, Fig. 4.5(c) plots the axial and transverse intensity profiles of a $2\ \mu\text{m}$ silica bead reconstructed through in-line DHM (intensity derived by back-propagation of the green hologram). This figure proves what already discussed in § 4.1: the intensity transverse cross section represents quite closely the nominal dimension of the bead (gray shaded area), while the axial profile is much more elongated. On the contrary, 3-axis DHM results in Fig. 4.5(d) show an unprecedented axial resolution for a holographic microscopy technique. The axial and lateral profiles, having comparable width, reflect pretty well the bead dimensions, with the axial one slightly elongated in agreement with the aspect ratio of the beads in Fig. 4.5(b).

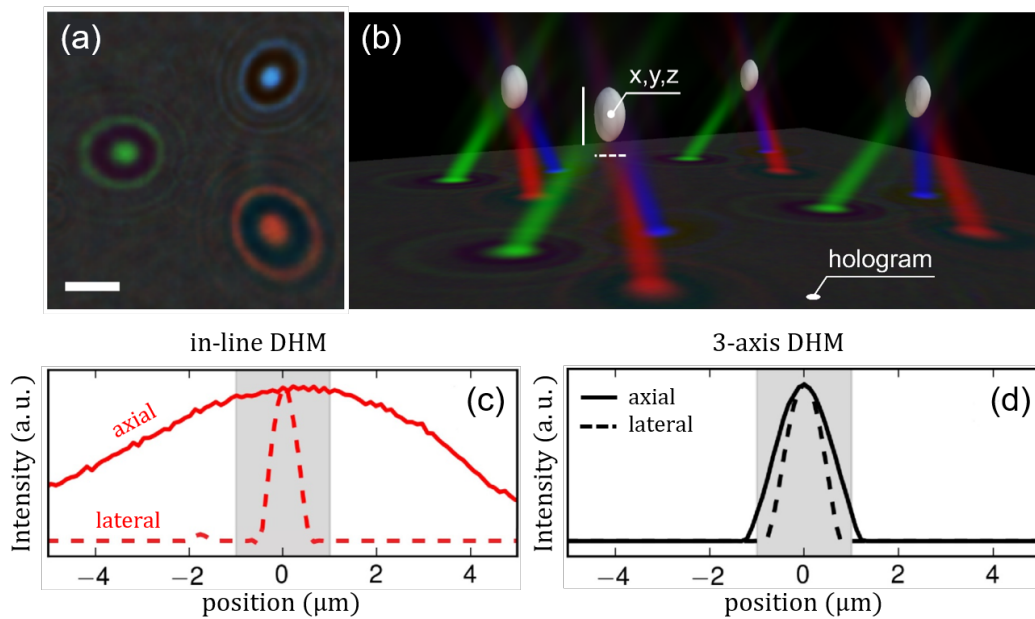


Figure 4.5. 3-axis DHM on $2\ \mu\text{m}$ silica beads. (a) RGB hologram of a single bead (scale bar is $5\ \mu\text{m}$). (b) The three color channels are numerically reconstructed by free-space back-propagation (RGB density maps). The elongated refocusing regions intersect at the scatterer location, which appears as a mildly elongated blob, depicted in white. Further analysis of the overlap region gives information on beads position (x, y, z) and axial and lateral dimensions (solid and dashed white segments, respectively). (c) Profiles of the reconstructed intensity of a single color channel along directions parallel (solid) and transverse (dashed) to the illumination axis. (d) Axial (solid) and transverse (dashed) profiles of the volumetric image ρ_j of j -th bead, obtained overlapping the three color channels. Gray shaded area in (c) and (d) indicates the size of the $2\ \mu\text{m}$ silica bead. Taken from [26].

Another limitation of in-line DHM that can be successfully faced with 3-axis geometry is the “shadowing” effect produced by particles stacked along the optical axis [26, 143]. Using a 3-axis illumination avoids this problem and results in a perfect volume sectioning. In Fig. 4.6 we show the volumetric reconstruction of four beads trapped along the z axis with both in-line and 3-axis DHM. The arrangement of the micro-spheres can be directly realized from the RGB hologram in Fig. 4.6(a), where the fringe patterns are laterally shifted as the distance of the beads from the image plane increases. However, nothing more than a simple intuition of beads position

results before the RGB hologram is back-propagated, the independent intensities overlapped and the threshold applied. As shown in Fig. 4.6(b), the final 3D intensity distribution ρ^Γ allows a very efficient sectioning of the sample volume. The four beads can be easily resolved, as witnessed also by the ρ intensity profile along the vertical axis crossing all the beads, plotted in Fig. 4.6(c).

On the contrary, a much more confused scenario results from in-line DHM strategy, performed with the green LED to vertically illuminate the same axially displaced four beads. Fig. 4.6(e) shows the intensity of the field derived by back-propagation of hologram in Fig. 4.6(d). In this case it is impossible to distinguish any of the beads, with the intensity profile along the vertical axis in Fig. 4.6(f) appearing meaningless.

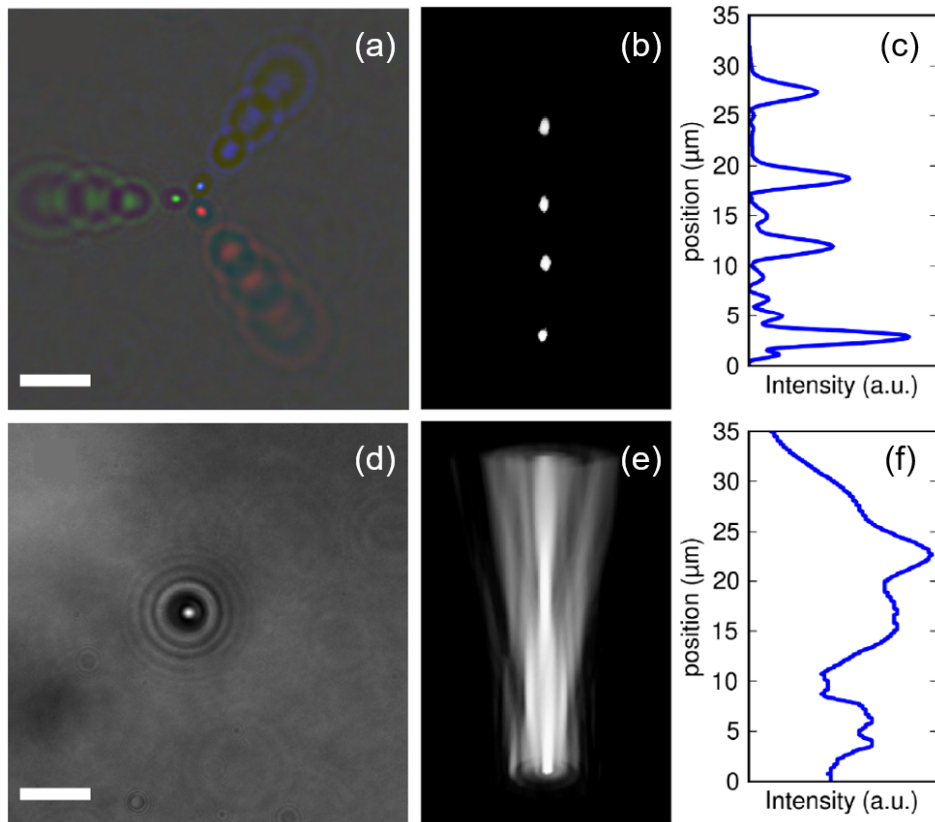


Figure 4.6. In-line vs 3-axis DHM reconstruction of four silica beads trapped along a vertical line. (a) RGB hologram of the four beads. (b) 3-axis volumetric reconstruction of the RGB hologram (threshold already applied). (c) Plot of intensity ρ along the vertical axis passing through all the four beads. (d) In-line monochrome hologram of the same four particles. (e) Volumetric reconstruction of the field intensity from the in-line hologram and (f) corresponding intensity profile along the vertical axis. Scale bar in (a) and (d) is $10\ \mu\text{m}$. Taken from [26].

3-axis DHM extracts accurate morphological information even for objects with more complex shapes, provided that the Born approximation for scattering is fulfilled. Since this is the case for weak scatterers and for thin or slender bodies, our technique can be tested on a much more challenging 3D object: an *E. coli* bacterial cell trapped

a few microns above the focal plane. RGB density maps in Fig. 4.7 represent the intensities reconstructed by numerical back-propagation of the underlying RGB hologram. The white isosurface in the overlap region clearly shows the position, orientation and shape of the bacterium prolate body. The cell position can be derived as discussed before, while the body length is extracted as the total extent of the binary image along the eigenvector $\hat{e} = (e_x, e_y, e_z)$ describing the bacterium orientation, which corresponds to the largest eigenvalue. The combination of optical tweezers and

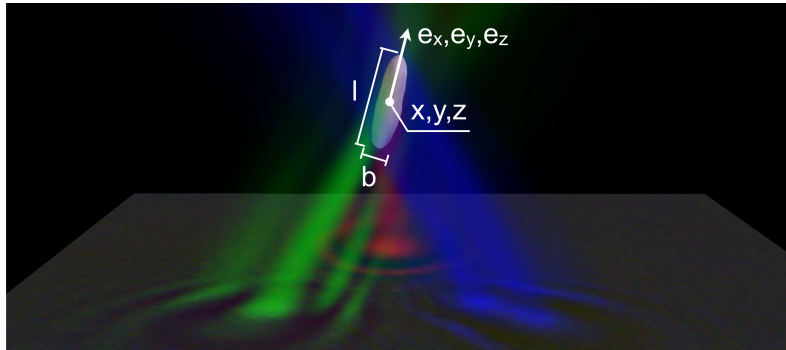


Figure 4.7. The RGB hologram is back-propagated to numerically reconstruct the three independent scattered fields, whose intensities are represented by red, green, and blue density maps. An isosurface of the overlapped intensity is represented in white and closely matches the shape of a trapped *E. coli* bacterium. Morphological analysis of the overlap region gives information on position (x, y, z) , size and shape (l, b) , and orientation (e_x, e_y, e_z) of the cell.

3-axis holographic microscopy allows to record the 3D motion of individual *E. coli* bacteria swimming in optical traps with the typical run and tumble pattern [151]. In particular, two cell run states (forward and backward) can be observed, with relative propulsion forces, total torque, and bundle conformations [152]. The statistical properties of bundle reversal can be analyzed and the hydrodynamic features of forward and backward running states compared.

3-axis microscopy can also bear the real-time 3D imaging of objects rapidly moving in the FOV, like swimming bacteria. A meaningful example, representing also an interesting case of study, is the mechanism by which self-propelled particles, both synthetic and biological as *E. coli*, are stably trapped by walls and develop high concentration peaks over bounding surfaces [153–155]. In addition to being an interesting dynamical problem on its own, cell-wall interactions have a strong biological relevance in the first stages of biofilm formation [156–158]. Moreover, understanding cell-wall interactions is also important in designing wall geometries that can be used to direct bacteria inside micro-fluidic devices [159, 160] or exploit bacteria as tiny propellers in micro-structures [161, 162]. A clear experimental demonstration and description of a wall entrapment effect necessarily requires a systematic 3D analysis of both positions and orientations. The combination of holographic tweezers and 3-axis microscopy allows to reconstruct with submicrometer resolution (lateral: $0.4 \mu\text{m}$; axial: $0.8 \mu\text{m}$) the full 3D entrapment dynamics of smooth swimming *E. coli* cells. Individual cell bodies can be grabbed with two holographic traps at their poles, oriented, and released at a controlled distance ($\sim 10 \mu\text{m}$) and

angle from a flat wall, which can be either solid or gassy [27, 163]. Figs. 4.8(a) and (b) show two frame sequences in which cells collide with a liquid-solid interface and a liquid-air interface, respectively. When close to the solid interface, cells always swim along a clockwise circular trajectory. This behavior is well known [154, 159, 164] and typical of no-slip boundary interfaces [165]. Conversely, on the liquid-air interface, cells swim along a counter clockwise trajectory as already observed and explained as due to free-slip boundary conditions [165, 166]. Despite that, bacteria approach the two surfaces with a very similar dynamical behavior, as shown in Figs. 4.8(d) and (e), where the cell body pitch angle θ (red line) and the cell-interface gap h (black line) are reported as functions of time for the same two cells in Figs. 4.8(a) and (b). The quantities h and θ are defined in the sketch in Fig. 4.8(c). The curves in Figs. 4.8(d) and (e) display the same qualitative behavior characterized by the presence of three stages: approach, reorientation (gray area in Figs. 4.8(d) and (e)), and surface swimming. In the first stage, the cell swims towards the wall and h shows a rapid decay, while θ oscillates around a stable value. The fast oscillations of θ are due to cell wobbling, *i.e.* a precession motion of the cell body axis around the swimming direction [4, 152]. In the reorientation stage, h is close to zero, which corresponds to a cell in contact with the interface, and the cell tilt angle θ starts to decrease as the cell body aligns to the surface. In the last phase, surface swimming, both h and θ oscillate around a stationary value. The recorded data of swimming bacteria can be processed in many different ways, accordingly to which aspect of their motion needs to be studied.

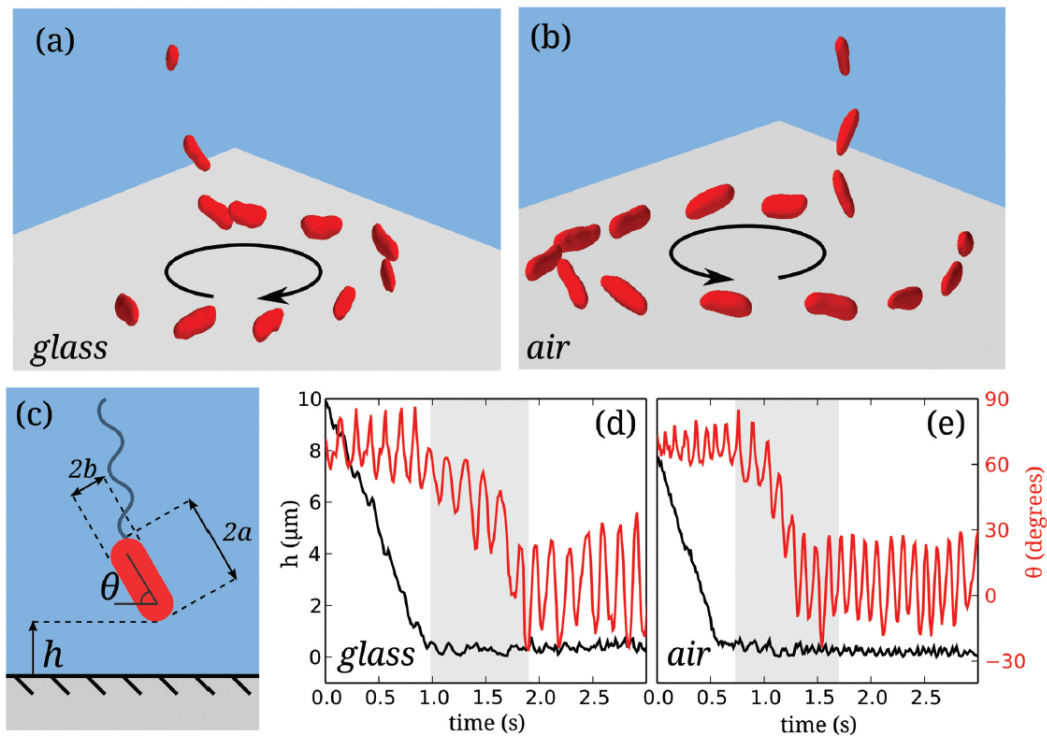


Figure 4.8. Wall entrapment at liquid-solid and liquid-air interface. (a,b) Sequence of volumetric reconstructions of swimming cells from an entrapment event in the case of a solid-water interface (a) and of an air-water one (b). (c) Sketch of a bacterium approaching the interface. The coordinates h (black line) and θ (red line) corresponding to (a) and (b) are plotted respectively for the liquid-solid (d) and the liquid-air (e) interfaces. Taken from [163].

Chapter 5

Virtual reality

Nanomanipulators based on scanning tunneling microscope or atomic force microscope represent an important step forward in the field of interactive tele-operation of microscopic samples (see § 2). Due to their design, however, they are forced to work with either imaging or manipulation purposes. Such a constraint, together with their limited scanning speed, prevents the simultaneous and live manipulation and sensing of micro-systems. Moreover, this technique cannot handle objects really moving in 3D, but it only pushes particles on a substrate with a tip. The invention of holographic optical tweezers provided a powerful technology for the live dynamic manipulation of micron-sized and smaller particles in 3D (see § 3). On a parallel track, our 3-axis implementation of digital holographic microscopy ensures high-frame-rate volumetric reconstructions with a good resolution in the three directions of space (see § 4). Integrating these two techniques through a modern high-performance computing system allows for the interactive exploration and manipulation of complex 3D micro-systems in real time.

Some advanced interfaces have been proposed to facilitate the handling of trap arrays. Among others, we mention a multi-touch interface implemented on an Apple iPad [10], capable of processing up to 11 simultaneous touches, a force-feedback device providing a haptic controller on the micro-world [11], and an interface that integrates the Microsoft Kinect sensor bar to reconfigure trap arrays following user input gestures [167]. Despite such innovative interfaces, the visual feedback is still limited to a 2D projection of the system displayed on the screen of a computer. Conversely, a truly immersive experience would require the user to be projected into the microscopic environment with the ability to manipulate it from “within”. This task can be accomplished through an interface capable of reproducing a replica of the micro-system all around the user. In this regard, particularly suitable is the technology of virtual reality, which, together with augmented reality and mixed reality, is transforming the way we explore and interact with the macroscopic world around us. Scientific applications are very limited at the moment, although they are potentially revolutionary in many fields. Within the scope of neuroscience, the inner workings of animal and human brains are increasingly explored using virtual reality to simulate real world inputs [18]. In the context of molecular dynamics simulations, virtual reality interfaces are found to facilitate sophisticated molecular modeling tasks [19]. Furthermore, scientific education and training can greatly

benefit from virtual reality in order to implement virtual laboratories where safe and economical experiments can be performed [20]. In all these applications, however, virtual reality is doubly artificial, being a software rendering of software objects. More than simulating presence in artificial environments, using virtual reality we can be virtually present in real but physically inaccessible worlds to explore them from “inside”. In this PhD project, we developed an unprecedented system that, by integrating HOT and 3-axis DHM through a VR interface, allows the user to enter microscopic samples to manipulate them in real time with his own hands and analyze their live response immersively. Along this chapter we present the hardware and the strategy adopted to design such a system, together with the software managing our interface with all the virtual tools we implemented.

5.1 VR hardware: headset and hand-tracking devices

Our VR workstation integrates the **Oculus Rift CV1** system, shown in Fig. 5.1. This VR system is composed of a headset for the 3D visual (and audio) rendering and a pair of joysticks for hand-gestures tracking. A pair of sensors (not in figure) is in charge of collecting head- and hand-tracking data for the real-time update of the virtual environment.



Figure 5.1. Oculus Rift CV1 virtual reality system, composed of a headset for 3D video and audio rendering, a pair of joysticks for input hand signals and a pair of “constellation” tracking sensors (not in figure).

The **headset** mounts two PenTile OLED displays of 1080×1200 pixels per eye (stereoscopic view: 2160×1200 pixels), providing a field of view of 110° with a refresh rate of 90 Hz. The lenses distance can be customized by moving a slider below the device (see Fig. 5.1), in order to fit the user inter-pupillary distance. This headset model is also provided with integrated headphones for a fully immersive virtual experience.

In Fig. 5.2 the two **joysticks** of the Oculus Rift CV1 system are reported with

the different input channels. Every input command affects the value of its channel variable in the running VR software. We now describe the input channels pointed in the figure.

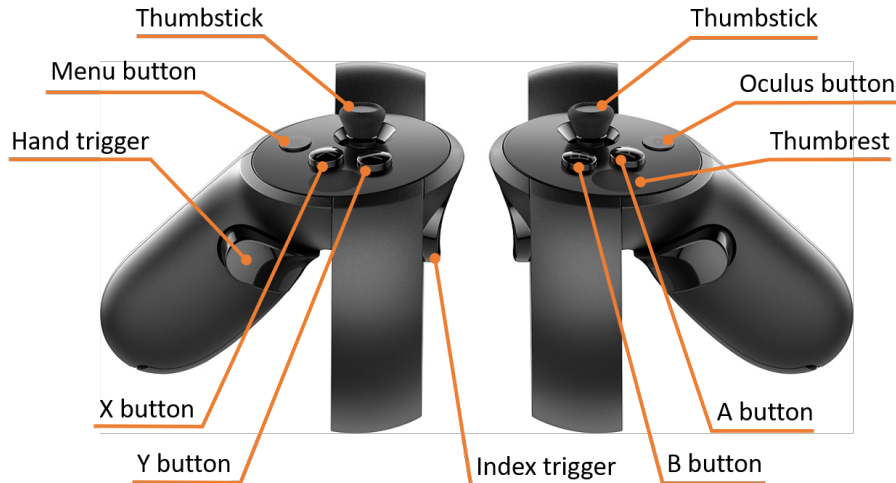


Figure 5.2. Hand-tracking controllers of the Oculus Rift CV1 system and relative input channels.

- **A, B, X, Y, Menu, and Oculus buttons:** the variable monitoring the status of each button turns from 0 to 1 when the relative button is pushed.
- **Thumbrest sensors:** each of these two touch sensors generates the same signal of the buttons described above when the user’s finger touches their active area.
- **Hand triggers:** each of these two triggers is a single-axis lever that generates a gradual signal between 0 (not pressed) and 1 (totally pressed). They can also work as normal binary buttons.
- **Index triggers:** these two levers share the same functions of the two hand triggers. In addition, they are equipped with a touch sensor that detects the user’s index finger detach gesture.
- **Thumbsticks:** these 2-axis levers generate a gradual signal between -1 and 1 for each of the two directions in which the stick can move (horizontal and vertical). They also act as buttons when pressed.

Apart from the Oculus button, which controls the options menu of the Oculus built-in software, all other input commands can be exploited individually or in custom combinations to send frame-by-frame signals to the running VR software.

Data on position and orientation of the user’s head and hands is collected using the “constellation” tracking system. A pair of **infrared LED sensors** ensures the full 6-degree-of-freedom (3 positional, 3 rotational) optical tracking of tailored VR devices with submillimeter precision and negligible time lag. Any device tracked

with this system is equipped with a series of infrared LEDs with precise position and specific blinking pattern. By knowing the configuration of the LEDs on the object and their blinking pattern, the system can recognise and perform accurate spatial tracking of the device in real time.

5.1.1 Data transfer protocol

In order to integrate the HOT and 3-axis DHM techniques through a VR interface, we designed the system schematically illustrated in Fig. 5.3(a). In a room there is

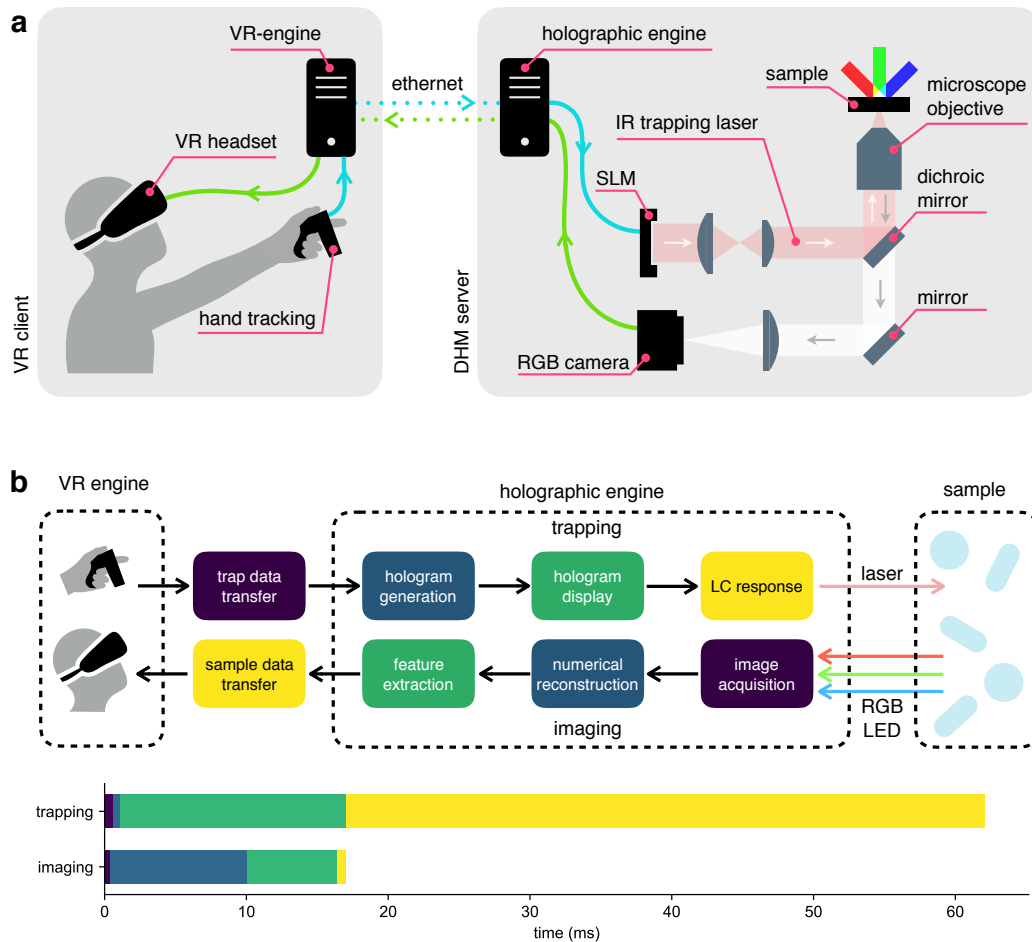


Figure 5.3. (a) Schematic view of the optical and computer hardware setup. The sample is illuminated by three tilted RGB LEDs and a $100\times$ magnified image is captured by a color camera. The “holographic engine”, running on a control PC in the lab, performs 3D numerical reconstructions and identifies the objects in the field of view. Position and shape parameters of the objects are sent to a remote PC running a “VR engine” that renders the objects on a VR headset. Hand-tracking input data is transferred back to the “holographic engine” for the computer generation of digital holograms to be displayed on the SLM. The SLM shapes the wavefront of an IR laser beam that is then focused by the same imaging objective to generate the desired 3D traps arrangement. (b) Data and optical flow diagram and related timing chart. Chart colors correspond to the boxes above it.

the “VR engine” (client), which exchanges data flows with the “holographic engine” (server) through an Ethernet connection. We integrated the holographic techniques for manipulation and imaging using a game engine that supports user interaction through the Oculus Rift CV1 system (further details in § 5.2). Optical traps are implemented as game objects that can be interactively and independently created, destroyed, selected, and moved around using hand gestures (*i.e.* “grab”) or more sophisticated remote control tools. When the “VR engine” detects an event related to the creation, destruction or displacement of traps, the data describing the updated traps configuration is sent to the “holographic engine”. The “holographic engine” runs on a computer controlling the optical hardware in a separate lab (detailed setup in § 4.2, Fig. 4.4). When an update request is received from the “VR engine”, the “holographic engine” computes an optimized digital hologram on the computer GPU and directly displays it on a liquid crystal SLM (Hamamatsu X10468-03). A collimated infrared laser beam ($\lambda = 1064$ nm) reflects off the SLM and acquires a phase modulation such that, after propagation through a microscope objective (Nikon 100 \times , Plan Apo λ , NA = 1.45) produces diffraction limited spots having a spatial arrangement that is the same as their virtual counterparts. Each of these spots serves as an optical trap that can be used to grab and manipulate small dielectric objects, such as colloidal particles or living cells, in a 3D region covering the entire field of view. Typically, trap rearrangements result in the rapid motion of nearby objects, which are captured in RGB holographic images (light sources: Prizmatix UHP-T-LED-630, Prizmatix UHP-T-LED-520, Prizmatix UHP-T-LED-460) by a color camera (Basler avA1000-100gc) at 40 fps, and processed in real time by the “holographic engine”, as described in § 4.2. The obtained volumetric reconstructions are segmented to extract the relevant geometric features of all identified objects. These geometric data are sent back to the “VR engine” to update the geometric parameters of game objects providing a virtual representation of the real objects that are being interactively manipulated under the microscope.

A current limitation of our system lies in the difficulty of discriminating nearby objects in conditions of high density. When we propagate scattered fields backwards, interference between scattered fields from nearby objects can give rise to imaging artifacts. For example, our 3-axis implementation of DHM fails to return two disconnected regions when two objects are separated by less than $0.5 \mu\text{m}$ in xy plane. A safer distance along the vertical direction z is approximately $1 \mu\text{m}$.

In order to match coordinates between trapping and imaging spaces, we trap a glass micro-sphere ($1 \mu\text{m}$ radius) and scan its position \mathbf{r}' in trapping space on a three dimensional grid. During scanning, the trapping laser power is maximum to minimize displacements from the trap equilibrium position caused by Brownian fluctuations and gravity. We extract the corresponding bead coordinates $\mathbf{r} = (x, y, z)$ in imaging space from the 3D reconstructions. Finally, we compute the transform $\mathbf{r}' = T\mathbf{r} + \mathbf{r}_0 + \alpha z^2 \hat{\mathbf{z}}$ by fitting the matrix T , a linear transform operator, the vector \mathbf{r}_0 , which represents the displacement between the two origins, and the empirical factor α , which takes into account small displacements in the position of the trap due to spherical aberrations.

The closed complex flow of data and light just described, starting from the “VR engine”, is summarized in Fig. 5.3(b). For trapping alone, the maximum achievable refresh rate is limited to 20 Hz, the main bottleneck being the slow response dynamics

of 45 ms of the SLM liquid crystals. Even if we neglect this slow response, the SLM is refreshed at a 60 Hz rate, corresponding to a minimum lag time for hologram display of 17 ms. Optimized phase masks are generated using a GSW algorithm (see § 3.3), with a computation time that scales linearly with the number of traps as well as the number of optimization steps. We set the number of GSW iterations to 3, giving an expected efficiency (ratio of trapping spots power over the total power) of about 80%. The resulting total computation time per trap is 0.48 ms, so that most of the computational time is used for image analysis (blue bars in Fig. 5.3(b)). On the imaging side, the main frame rate limiting factor is the computational time of the tasks performed by the “holographic engine”. Starting from a 512×512 RGB frame, whose acquisition time is negligible, we obtain a volumetric image of $512 \times 512 \times 61$ voxels (corresponding to a field of view of $56 \times 56 \times 20 \mu\text{m}^3$) in 9.7 ms. The segmentation of the volumetric image takes about 5.8 ms, while the extraction of position and orientation of each of the identified objects takes about 0.5 ms. For instance, if two objects are present in the field of view, the total time required to obtain a full geometric description of the scene is 16.5 ms. System latency, *i.e.* the time interval between a trap rearrangement input from hand-tracking devices and the actual observation of the resulting objects motion, can be estimated from data in Fig. 5.3(b) by summing the total trapping time (62 ms) to the total imaging time (15.5 ms + 0.5 ms per object), which gives an overall latency of about 80 ms. This latency is low enough to guarantee a smooth and interactive manipulation experience.

Such an estimate also includes the time due to a back-and-forth data transfer event, which affects both the trapping and imaging process. For the sake of the Ethernet communication efficiency, we implemented in our system the User Datagram Protocol (UDP), which uses a simple connectionless communication model to send messages, referred to as datagrams, to other hosts on an Internet Protocol network. The structure of each datagram can be divided in two parts: the header, consisting of four fields of 2 bytes each, followed by the data section, which is the payload data of the message. In particular, the header fields are the source and destination port numbers, respectively identifying the sender and receiver ports, the length, which specifies the length in bytes of the header and data sections, and the checksum, used for error-checking of the header and payload data. As can be deduced from the datagram encoding, UDP provides checksums for data integrity and port numbers for addressing different functions at the source and destination of the datagram. However, since connectionless protocols do not set up any dedicated end-to-end connections, communication is achieved by transmitting information in one direction from source to destination without verifying the readiness or state of the receiver. With no handshaking dialogues, UDP exposes the communication to any unreliability of the underlying network: there is no guarantee of delivery, ordering, or duplicate protection. Despite all these drawbacks, UDP is particularly suitable for purposes where error checking and correction are either not necessary or are performed in the software. Since it avoids the overhead of such processing in the protocol stack, UDP is very useful to time-sensitive applications, when dropping packets is preferable to waiting for packets delayed due to retransmission. All this works well for our real-time system, too, for which the time per data transfer event is only 0.6 ms.

5.2 VR software: immersive micromanipulation interface

Despite VR is by now a very advanced commercial technology, whose increasing capabilities can be successfully addressed to different purposes, its great success in video games encouraged the birth of a number of useful tools that facilitate developing gaming applications. In order to exploit the power of VR to integrate the holographic techniques for manipulation and imaging described before, we created an immersive interface using the game engine Unity [168], which supports user interaction through VR devices such as the Oculus Rift CV1 system. Thanks to the smart organization of its workspace in different windows, shown in Fig. 5.4, the Unity editor turns out to be particularly convenient to build this kind of projects. These windows are the Project window, which collects all the available assets arranged in folders, the Hierarchy window, where all game objects in the play area, whether they are active or inactive, are listed, the Inspector window, showing all the components attached to a selected game object or asset, and the Scene view, which represents the real working table where the play area can be shaped and inspected from different perspectives. Moreover, by running the play mode the application can be tested in any moment in the editor Game view, looking for any bugs. In particular, the changes made in play mode are very helpful for various live attempts, since they won't be saved in the end. Conversely, permanent modifications can be applied outside of play mode, where all objects in the Hierarchy can be individually edited from their respective Inspector windows, while configuring an asset in the Project window affects all objects where it is implemented.

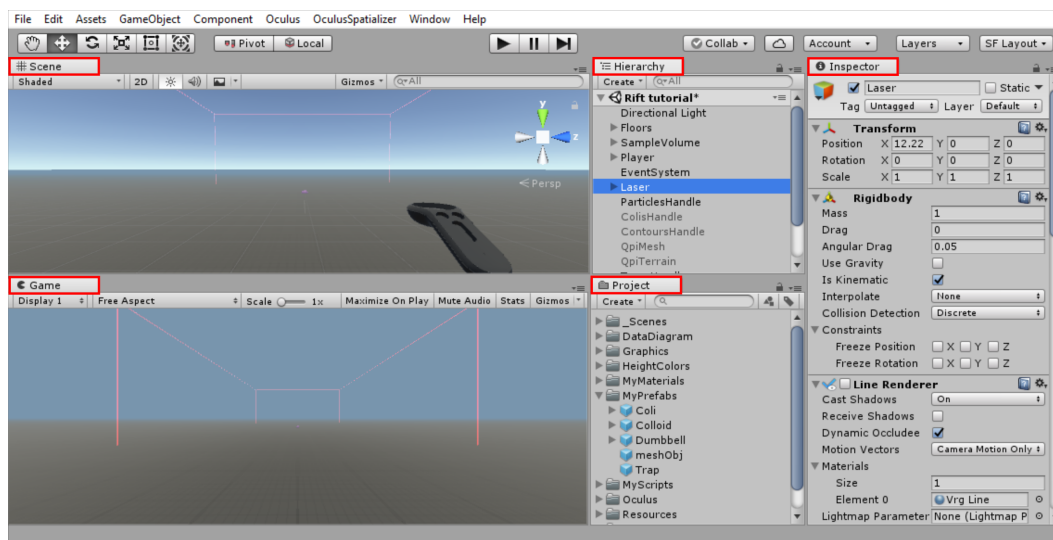


Figure 5.4. Unity editor view. The workspace is organized in multiple windows, namely Scene, Hierarchy, Inspector, Game, and Project, which are highlighted in red.

The first step to create an application is to create a new scene. As levels in a game, scenes are ways to organize different scenarios. In our case, we need a single scene for our interface. Then, we need to create the play area, representing the virtual environment where game objects replicating the microscope sample will

appear. In order to do this, we can use primitives, simple pieces of geometry (*e.g.* planes, cubes, spheres, capsules) that come bundled with the Unity editor and can be used individually or combined together to form various objects. In this respect, an empty game object can be created and filled with multiple primitives attached as children, which can be arranged to form a complex parent of arbitrary shape. The appearance of any game object can be modified by adding a color or a texture. To this aim, custom materials can be created in the Project window and defined in their parameters, such as color, transparency, metallic look, or smoothness. In order to apply the material to an object, the former needs to be dragged onto the latter in the Hierarchy window or in the Scene view. The core structure of our virtual environment is composed of a plane (floor), reproducing the coverglass, and a virtual red-light cage made of eight cylindrical rods that signals the boundaries of the reconstructed micro-volume (see Figs. 5.4 and 5.5(b)). The latter can be shown or hidden by button control. The whole scene is lighted by a whitish vertical light. For VR applications, the player game object is provided by an open source Oculus virtual reality software development kit, which rules how it moves and operates around the virtual space. In particular, the left thumbstick controls its bi-dimensional horizontal motion, while the third dimension can be navigated with buttons X and Y to go down and up, respectively. The player can also turn around by horizontally moving the right thumbstick. In addition, pressing the left index trigger speeds up all movements. The camera object that defines the point of view on the virtual space is clearly integral with the player head position. For the sake of the user experience realism, a tailored game object needs to be configured as a virtual counterpart to every type of real object under the microscope. In this respect, for instance, micron-sized beads are figured as spheres, bacterial cells as capsules with adjustable elongation, and optical traps as point-like light sources. Any game object can implement several components, which once attached can be edited directly from the Inspector window. Some components shared by most objects are the Transform component, through which the object position, rotation, and scale are set, the Mesh Filter and Mesh Renderer components, in charge of shading and rendering the object, and the Collider component, which defines the objects boundaries either for inter-object collisions or to trigger tailored functions when the “Is Trigger” checkbox is enabled and two objects touch. Furthermore, some built-in Unity packages are used to provide specific enhanced functionality to objects: if an item has to respond to forces and gravity, for instance, the Rigidbody component needs to be attached. In particular, any game object implementing a Collider and a Rigidbody components is considered dynamic rather than static by Unity, which is extremely convenient for objects that need to be updated every frame.

One of the most useful features of Unity is the possibility of writing additional code in C# language to integrate the behavior of game objects with tailored new functions. Once compiled, such scripts can be implemented like any other component. The most popular editor to write code for Unity applications is Visual Studio [169], which provides a preset template with the main namespaces and functions already included. Namespaces are collections of classes and data types which can be imported at the start of the script. The main ones, used in most of the codes, are System.Collections, System.Collections.Generic, and UnityEngine, although many others can be selected depending on the classes needed. Regarding the functions, two of them play a major

role in Unity scripts: Start and Update. The code in the Start function is called on the first frame that the script is active, while the code in Update is called once per frame. Actually, different versions of the Update function exist and are called in slightly different moments of each frame. The standard Update function is called before rendering a frame, and this is where most of the code goes. In addition, there are the FixedUpdate function, which is called just before performing any physics calculations and thus contains the physics code, and the LateUpdate function, which runs every frame after all other update functions are done. We can also write our own additional functions, which are accessible either only inside the running script or from other scripts, too, depending on whether they are defined as private or public, respectively. As usual, the basic bricks used to write functions are variables, which can be of different types depending on the data they need to store (*e.g.* numbers, Boolean values, vectors, game objects, components). As functions, variables can be defined either as private or public. In this last case, they can be accessed not only from other scripts, but also from the relative object Inspector, and this allows an easier setting. From inside a script, moreover, we can have access to the components of both the current game object and all other objects in the Hierarchy, with all their variables.

An additional feature of the Unity editor, which allows the application to classify different game objects, is the built-in tag system. In the Inspector of any game object, indeed, a tag can be either selected among a few pre-made values or custom created. By comparing an item tag value to a string, tailored tools that have been specifically implemented for that object can be triggered. Using this strategy, all primary objects inside our software are managed with appropriate functions, which will be described later on. All tagged items, however, are mainly classified into two categories: “grabbable” objects and “trappable” objects. In particular, a “grabbable” object has to be manipulated inside the virtual environment: the user can grab it with his virtual hands by pressing either the right or the left hand trigger in the nearby of the object. Conversely, a “trappable” object is a virtual object whose real counterpart under the microscope has to be manipulated with optical tweezers. Such an item allows a virtual trap to be created at its location by remote control. As described before, a real optical trap is simultaneously created in the micro-sample at the location of the “trappable” object real counterpart. As “grabbable” objects, virtual traps can be handled inside our interface, resulting in the live displacement of real optical tweezers in the sample. At the same time, “trappable” objects following virtual traps replicate the behavior of trapped particles in the micro-system. All this is possible since game objects in the Unity application representing either optical traps or micro-particles implement clients that connect to two separate UDP sockets running on the holographic server and managing data transfer for trap coordinates and sample geometric parameters.

Once a game object has been properly configured, we can turn it into a prefab, which is an asset that contains a template, or a blueprint, of the object itself. The prefab can then be used in any scene in the current project to create custom replicas of the saved item. Moreover, we can make changes either to a single instance of the prefab or to the prefab asset itself, so that all asset instances in the game will be updated as well. In order to turn an item into a prefab, it needs to be selected in the Hierarchy and dragged into the Prefabs folder in the Project window. The

needed replicas of the prefab item can then be instantiated either inside the Unity editor, by dragging back the object from the Project window to the Hierarchy, or from a script.

Besides all 3D objects shaping the scene, the Unity editor also allows to display text items through the built-in User Interface (UI) system, whom we have used to create our options menu. Anytime a new UI text element is created, it needs to be attached as a child to a Canvas game object to behave correctly. In addition, the UI tool set also requires another game object called Event System, which is automatically created. When configuring a text element, we have to consider that the Transform component of UI objects is different from the other game objects in Unity. For UI objects, indeed, the standard transform is replaced with a Rect transform which takes into account many specialized features necessary for a versatile UI system, including anchoring and positioning. Moreover, using the appropriate namespace we can also set a text item by script.

Many different game objects have been implemented for all the experiments we performed. We will now present a list of the main ones with their specific functions.

- **Virtual pointer:** it serves for the easy manipulation of distant objects and it is activated by pressing the right index trigger. The pointer implements a range of tailored functions for all the different game objects we developed, which will be discussed case by case below. By pressing the right thumbstick button while pointing at an object, a panel is displayed showing all functions intended for that game object and the relative buttons combinations to operate them. All “grabbable” objects, in addition, can be remotely grabbed by pointing at them and pressing the right hand trigger. In this case, the pointing beam turns orange (see Fig. 5.5(b)) and can move the object around the field of view or act as a “tractor beam” to regulate the distance between the object and the user hand with the right thumbstick vertical motion. For a more realistic experience, a virtual pointer emitting the pointing beam is designed to appear in the player’s right hand at the activation moment (see the black object in the “Scene” view of Fig. 5.4).
- **Optical trap:** acting on these green-light point-like-source game objects (see Fig. 5.5(a)) results in real-time rearrangements of laser traps in sample space. They are created with button A either in front of the user or at the location of any “trappable” object when pointed. By pointing at a trap (or trapped object) and pressing button A again, the trap is cancelled. As a “grabbable” object, any trap can be manipulated either by hand or remotely with the pointer.
- **Traps handle:** it serves for global translations, rotations, and scaling of multiple traps (see Fig. 5.5(b)). This “grabbable” object can be activated/deactivated with button B. When it is active, any of its movements results in the integral displacement of all traps in the scene, which, however, can also be manipulated individually. By managing the handle with the virtual pointer, using the right and left thumbrest sensors the traps array can also be scaled or rotated around the axis signaled by the handle elongation. Another function is implemented

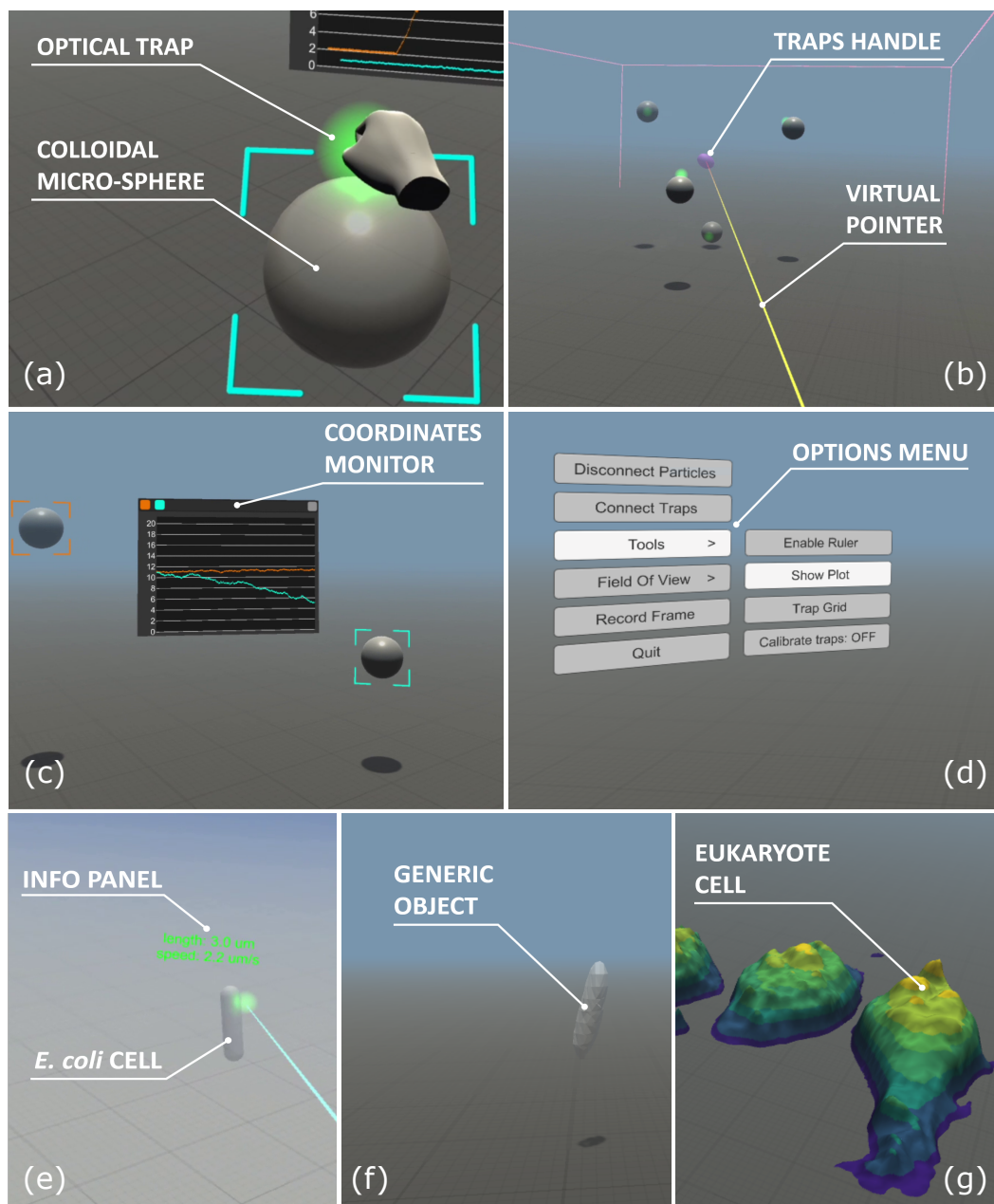


Figure 5.5. Example views of our virtual reality interface, where we highlight some of the tools we implemented. The figure shows a colloidal micro-sphere manipulated through an optical trap with hand gestures (a), the traps handle remotely manipulated with the virtual pointer (b), the coordinates monitor displaying the height of the selected beads (c), the options menu (d), an *E. coli* bacterial cell with its info panel (e), another *E. coli* bacterium rendered through the generic object mesh strategy (f), and an eukaryotic cell imaged with gradient-light-interference-microscopy technique (g).

that simultaneously creates/destroys multiple traps at the location of every object in the scene.

- **Colloidal micro-sphere:** the positions of these virtual objects (see Fig.

5.5(a)) follow in real time the Brownian motions of micron-sized spheres under the microscope. Anytime a colloidal bead enters/exits the reconstructed volumetric field of view, a virtual sphere like this one is created/destroyed. As mentioned before, virtual colloids are “trappable” objects, but not “grabbable”. Thus, such items cannot be grabbed in the virtual environment by hand or pointer, although they can be manipulated by handling real optical traps through their virtual counterparts. Attached to these game objects there is a panel showing their 3D position and size. Such a panel is always oriented towards the player’s head and can be activated/deactivated through the pointer by pressing the Menu button.

- **Bacterial cell:** the position, orientation, and size of these virtual objects with spherocylindrical shape of adjustable elongation (see Fig. 5.5(e)) follow the live motions of *E. coli* cells under the microscope. As the colloidal micro-sphere, it is a “trappable” object and it is created and destroyed upon the same principles. It also presents a similar augmented-reality info panel showing length and speed of the bacterium, which is activated when looking at the cell and is always oriented towards the player’s head as well.
- **Generic object:** the mesh of these game objects, which is originally empty, is shaped and shaded frame by frame with the triangle model returned by the marching cubes algorithm applied to the reconstructed volume of the micro-sample (further details in § 6.2). This strategy allows the real-time rendering of generic dynamic objects under the microscope, for which we lack an a priori knowledge on the shape. In order to show the quality of this approach, we report in Fig. 5.5(f) the reconstructed mesh of an *E. coli* bacterium. As colloids and bacteria game objects, this is also a “trappable” item.
- **Eukaryotic cells:** a terrain game object is shaped frame by frame with the 2D height map data obtained with gradient-light-interference-microscopy imaging technique (further details in § 6.3). With this method we can follow the slow dynamics of thin biological samples laying on a substrate, like a bunch of interacting Microglia eukaryotic cells (see Fig. 5.5(g)). A height-dependent color texture was also implemented for a better rendering of the sample shape.
- **Coordinates monitor:** this augmented-reality monitor plots the time evolution of custom quantities, which are different depending on the selected game object. For micro-spheres like those in Fig. 5.5(c), the height coordinate is displayed, while for living bacteria the swimming speed can be tracked. When the pointer is active, the user can select the particles to study by pressing the left thumbstick button. The selected particles are then framed by a square showing the same color as the relative track on the chart. As info panels attached to colloids and bacteria game objects, the orientation of this monitor follows the player’s head position. Moreover, it moves jointly with the player, unless he decides to fix it in a specific location of the scene by pressing the left thumbstick button while pointing at the screen. This monitor can be manipulated as any other “grabbable” object, either in the global reference or

in the player's one. Furthermore, it can be scaled up and down through the pointer with the vertical motion of the right thumbstick lever.

- **Options menu:** it is activated with the Menu button and presents a list of button game objects that allow the user to individually start/stop the connection with the two holographic server sockets, show/hide the field of view boundaries or activate useful tools, such as the monitor just described, an array of traps with preset configuration or a virtual micro-ruler for interactive distance measurement (see Fig. 5.5(d)). Furthermore, the remote calibration of optical tweezers via software can be triggered as well. When trap game objects appear slightly shifted respect to the virtual particles they handle, it may be appropriate to have a strategy to solve the problem inside our interface rather than re-calibrating the whole setup. By button control, all traps in the scene enter a "calibration mode" where their coordinates are no longer transferred to the "holographic engine". While real optical tweezers hold their positions, virtual ones can be moved and overlapped to the trapped particles. After that, the distance between virtual and real traps is saved as an offset that restores the matching between trapping and imaging spaces.

A complex system of control cycles ensures the absence of conflicts between all the functions just discussed, mostly when they share the same commands.

Chapter 6

Virtual micro-reality

Our innovative system can be customized and adapted to different purposes, with revolutionary effects in many fields. In order to demonstrate the power of virtual reality technology for scientific applications, we report some meaningful experiments immersively performed through the interface we developed. In the examples we present along this chapter, we observe and manipulate systems of different type, populated by both colloidal particles and swimming bacteria. Samples of the first kind were prepared by diluting silica and/or polystyrene micro-spheres of $1\ \mu\text{m}$ radius in pure water, while biological specimens were made of living *E. coli* bacteria in motility buffer (67 mM NaCl, 10 mM potassium phosphate, 0.1 mM EDTA, 10mM glucose, 0.02% Tween20 at pH 7.0). In particular, bacteria of the strain RP437 [170] (wild type) and HCB437 [171] (smooth swimmer) were grown overnight in 10 mL of LB supplemented with $100\ \mu\text{M ml}^{-1}$ streptomycin or $30\ \mu\text{M ml}^{-1}$ kanamycin respectively, at 30°C , 200 rpm. In the morning the culture was diluted 1:100 in 5 mL of Tryptone Broth (1% Tryptone, 0.5% NaCl) with kanamycin or streptomycin and grown at 30°C , 200 rpm until an OD600 of 0.6 – 0.8. Then the cells were washed through centrifugation three times at $1500\ g$ in motility buffer. The concentration of both synthetic and biological particles was regulated empirically depending on the experiment to carry out. The examples shown in § 6.1 required only few objects simultaneously present in the field of view, while for the demonstration in Fig. 6.10 a crowded sample of swimming bacteria was needed. The solution prepared in this way filled a micro-chamber made by sealing a cover slip to a microscope slide with NOA 81 UV curing optical adhesive. The depth of the chamber was defined by two pieces of a $140\ \mu\text{m}$ -thick wire between the glass walls.

6.1 Colloidal particles and living bacteria

6.1.1 Falling bodies

The first application we present is a simple experiment that demonstrates the potential impact of our instrument for physics education. If we grab two balls, one made of plastic and the other one made of glass, and release them from the same height, they will accelerate with constant speed along the vertical direction and hit the ground at approximately the same time. Now, we can do the same experiment but on a microscopic scale. As shown in Fig. 6.1, we can virtually

explore a microscope sample, look around and find two spheres, this time having a radius of $1\ \mu\text{m}$, floating above the cover slip. Acting on optical trap game objects with our own virtual hands, we can grab (a), lift (b), and release (c) the two micro-spheres. By watching them falling in front of our eyes (d), we can directly experience that a falling body experiment on the micro-scale looks very different than on the macro-scale. The spheres do not move on a vertical line but have a strong Brownian random motion. Although they slowly sediment, it often happens to see them moving up against gravity, which constitutes an apparent violation of the second law of thermodynamics [172].

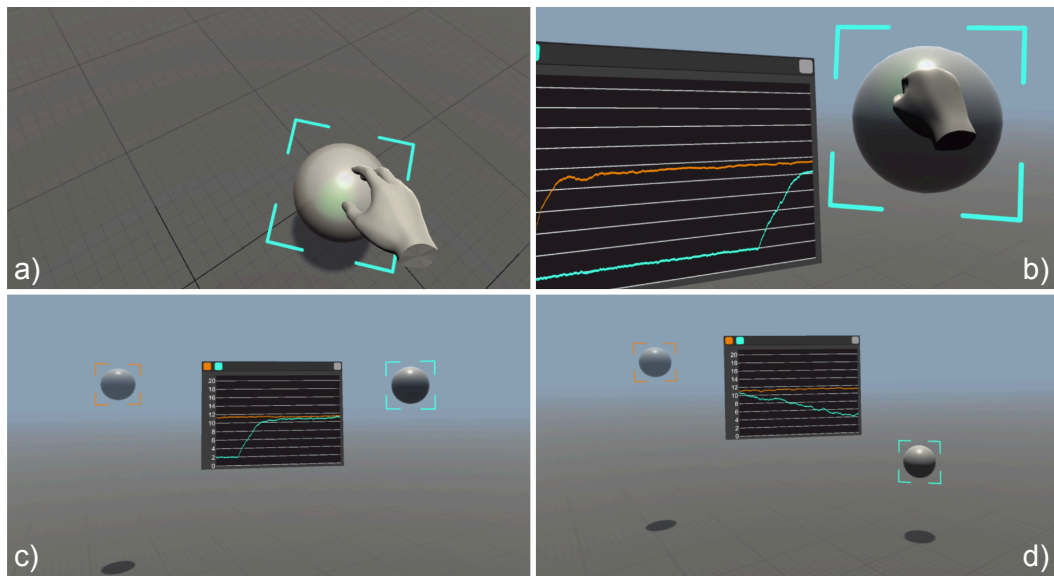


Figure 6.1. A silica (right) and a polystyrene (left) micro-spheres, both having a radius of $1\ \mu\text{m}$, are grabbed with the virtual hand (a), lifted to a height of $z \approx 11\ \mu\text{m}$ from the cover slip (b), and finally released (c) to observe their sedimentation. The heights of the targeted particles can be monitored in real time on a chart (d) that clearly shows that the right particle is heavier (complete data set in Fig. 6.2).

As described in § 5.2, our interface also implements a series of tools to track objects and watch the time evolution of their coordinates on a display (*i.e.* the coordinates monitor). The virtual chart in Fig. 6.1(d) shows that the two balls have very different sedimentation speeds, with the glass ball drifting down with a higher mean speed (the complete data set of the sedimentation is reported in Fig. 6.2). All this can be explained to students with words, pictures and movies, but doing the experiment in first person and watching all this happening in front of our eyes offers a unique and powerful experience of the physical laws that govern the micro-world populated by cells and colloidal particles.

6.1.2 Handcrafting micro-structures

The primary advantage of using holographic optical tweezers is the ability to dynamically arrange multiple traps in 3D. With this technique we can precisely arrange multiple colloidal particles or living cells in controlled spatial configurations to itera-

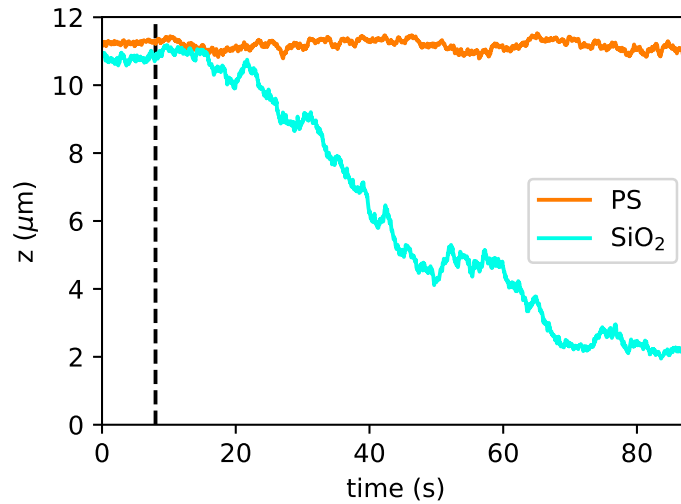


Figure 6.2. Time evolution of the height coordinate of the sedimenting silica (cyan) and polystyrene (orange) micro-spheres in Fig. 6.1. Despite some Brownian fluctuations, the silica sphere is heavier and sediments faster. The vertical dashed line highlights the moment of beads release.

tively study their stochastic behavior following reproducible initial conditions [27,101], or their biological interactions during growth [6]. Using multiple traps it is also possible to grab and rotate micro-fabricated objects with complex shapes, which can be used as tools for advanced microscopy applications [102,103], or for the study of Brownian motion and hydrodynamics of non spherical objects [104,105]. In this regard, a virtual reality interface could simplify and accelerate the assembly of a multi-component micro-system [173] and allow its direct operation with hand gestures and immersive feedback in real time.

As a demonstration of this, we show in Fig. 6.3(a-c) the live manipulation of a cubic structure made of 8 silica beads ($1\ \mu\text{m}$ radius). Grabbing the virtual traps handle, the full structure can be rigidly translated and rotated following hand movements in real time (a). Panel (b) in Fig. 6.3 shows the phase modulation that is simultaneously displayed on the SLM to generate optical traps at the location dictated by the 3D arrangement of the virtual handle. Panel (c) shows the raw holograms recorded on the three color channels of the camera before numerical reconstruction, tracking, and rendering on the VR headset. The possibility of using virtual hands to grab objects and arrange them in 3D configurations that can be inspected immersively and in real time can simplify enormously micro-assembly tasks, especially for users with no previous experience in microscopy and trapping. In support of this claim, we asked six researchers and students from our University to complete a simple 3D assembly operation consisting of placing a bead midway between two other beads. Each user performs the task three times using both our VR interface and a desktop user interface (keyboard or mouse), while the sample is viewed using bright field microscopy on the computer display (see Fig. 6.3(d,e)). In both cases, we calculate the time-to-completion as the mean time interval from the

moment the trap is created until the trap reaches its target within a tolerance of $0.2\ \mu\text{m}$. The time-to-completion using VR is significantly shorter than when using the standard interface ($p < 0.0001$), with an overall speed up factor of 6 (Fig. 6.3(f)).

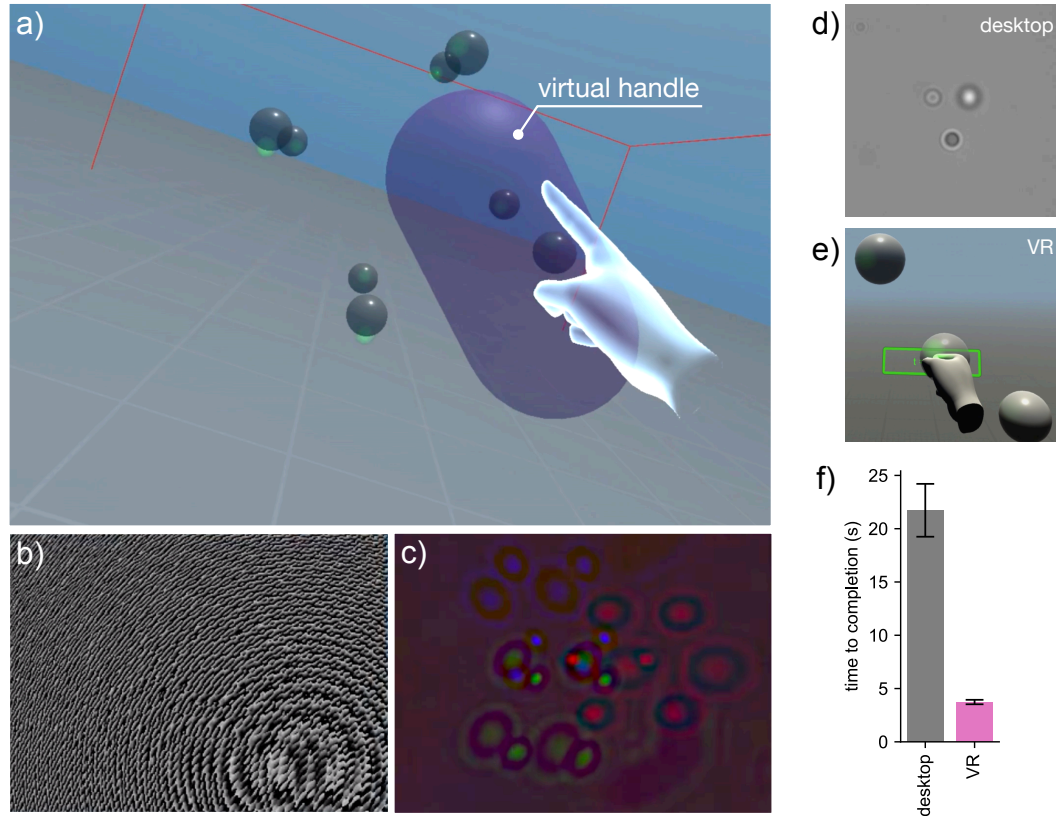


Figure 6.3. (a) Eight silica micro-spheres of $1\ \mu\text{m}$ radius are interactively arranged on the vertices of a cube and then rigidly translated and rotated through a virtual global handle in purple color. (b) Optimized phase mask displayed on the SLM to generate the trap arrangement in (a). (c) RGB hologram recorded by the camera and processed in real time to obtain the scene in (a), as described in § 5.1.1. (d) User micro-assembly task using the standard desktop interface. (e) User micro-assembly task through our VR interface. (f) Bar plots represent the sample mean of time-to-completion using the two interfaces (error bars are standard errors).

Micro-assembly experiments, moreover, are also strongly favored by tailored virtual tools that allow the easy manipulation of distant objects, such as our virtual pointer in Fig. 6.4. Using this tool, virtual traps can be individually pointed and grabbed at a distance, moved around the entire field of view to catch fluctuating beads and assemble them in custom configurations. We report in Fig. 6.4(a,b) the example of 4 beads that have been individually aligned to form a micro-rod of few microns length. However, when a fine tuning of traps relative position is needed, their one-by-one hand arrangement is no longer the most suitable solution. In this case, custom preset spatial configurations have to be loaded into software memory, so that trap arrays with precise geometry can be created at need. Using the virtual pointer, we can remotely grab the virtual trap handle to perform collective translations, rotations, and scaling of the trap grid. We report in Fig. 6.4(c,d) the

example of a tetrahedrally-arranged array of 4 traps, which are populated with collective manipulations of the grid, aiming to sequentially expose a free trap towards a free bead floating over the cover slip.

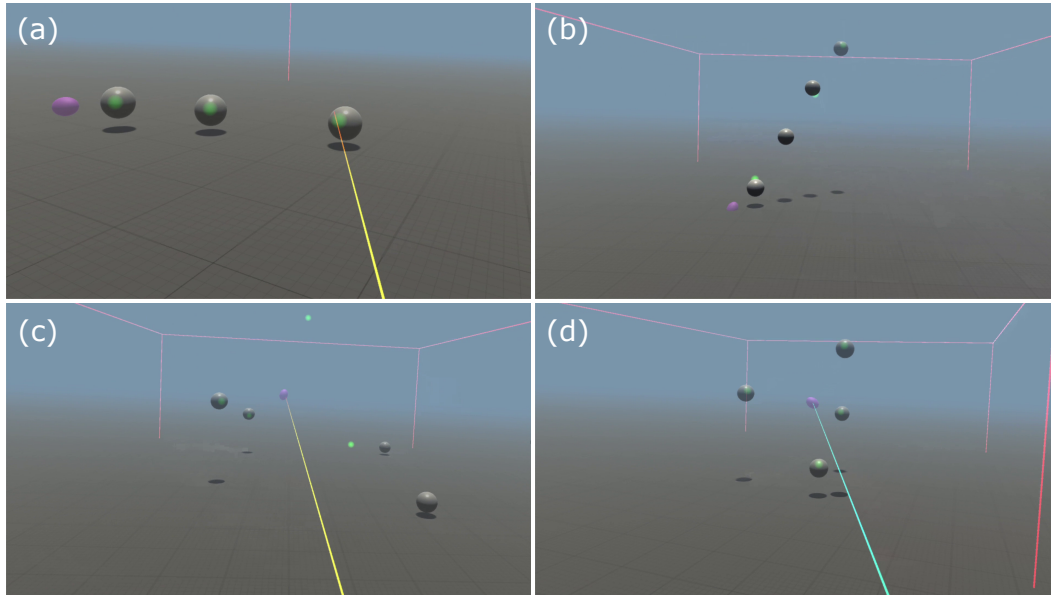


Figure 6.4. (a) Assembly of 4 beads ($1\ \mu\text{m}$ radius) along the same axis by remote manipulation of individual traps with the virtual pointer; (b) final micro-rod structure. (c) Assembly of the same 4 beads on the vertices of a tetrahedron by remote manipulation of a tetrahedral trap grid to pick up particles; (d) final structure. The virtual pointer takes on different colors depending on whether it is grabbing an object (orange) or just pointing at it (cyan).

6.1.3 Fishing for bacteria

In this last example, we demonstrate that, thanks to the high volume-rate achieved by 3-axis holographic microscopy and the reduced lag times in the information loop running between the “holographic” and “VR engine”, we can immersively explore a micro-environment populated by fast swimming bacteria. As mentioned before, we implemented an augmented reality system by which looking at a cell triggers the visibility of a panel displaying morphological and dynamical information on the cell such as length and speed (Fig. 6.5(a)). This feature could be very useful for future applications when a rapid characterization of motility is important, such as for sperm cells in artificial insemination, that could in addition take advantage of the trapping and sorting capabilities of optical tweezers. The trapping interface for bacteria has been optimized for rapidly moving objects. Colloidal particles diffuse by Brownian motion, which gives enough time to navigate in the immediate vicinity of the target bead, grab it through an optical trap and manipulate it with our virtual hands. With a speed of about $20\ \mu\text{m}/\text{s}$, bacteria can cross the entire field of view ($56\ \mu\text{m}$) in less than 3 seconds. We then implemented specific functions in our virtual pointer game object, which allows to quickly point at a distant target cell and, when clicking on a trigger, generate an optical trap at the 3D location of the nearest intersection

point between the virtual pointer beam and the game object representing a real cell. As in the beads assembly example, previously created traps can be selected with the pointer and rapidly moved across the entire field of view “fishing for bacteria” (Fig. 6.5(a)). Once a cell falls in a trap, we can move it around or bring it closer using the pointer as a virtual “tractor beam” that actually pulls the real optical trap towards the user hand. Last frame in Fig. 6.5(a) shows the same cell that, after switching off the trap, is set free and swims away with its initial speed. We can choose to record the tracks of selected objects for subsequent analysis. As an example, we show in Fig. 6.5(c) the 3D trajectory of the cell during the observation. The plot shows the typical circular trace swept by a swimming cell in presence of a bounding wall [155, 159, 163] (the coverglass in our case). The circles are followed by a short trace in which the cell is trapped and a nearly straight line that the cell draws after it is released. The trajectory color corresponds to the bacterium speed values in Fig. 6.5(b). This plot highlights the three moments of the interaction summarized by the frames in panel (a).

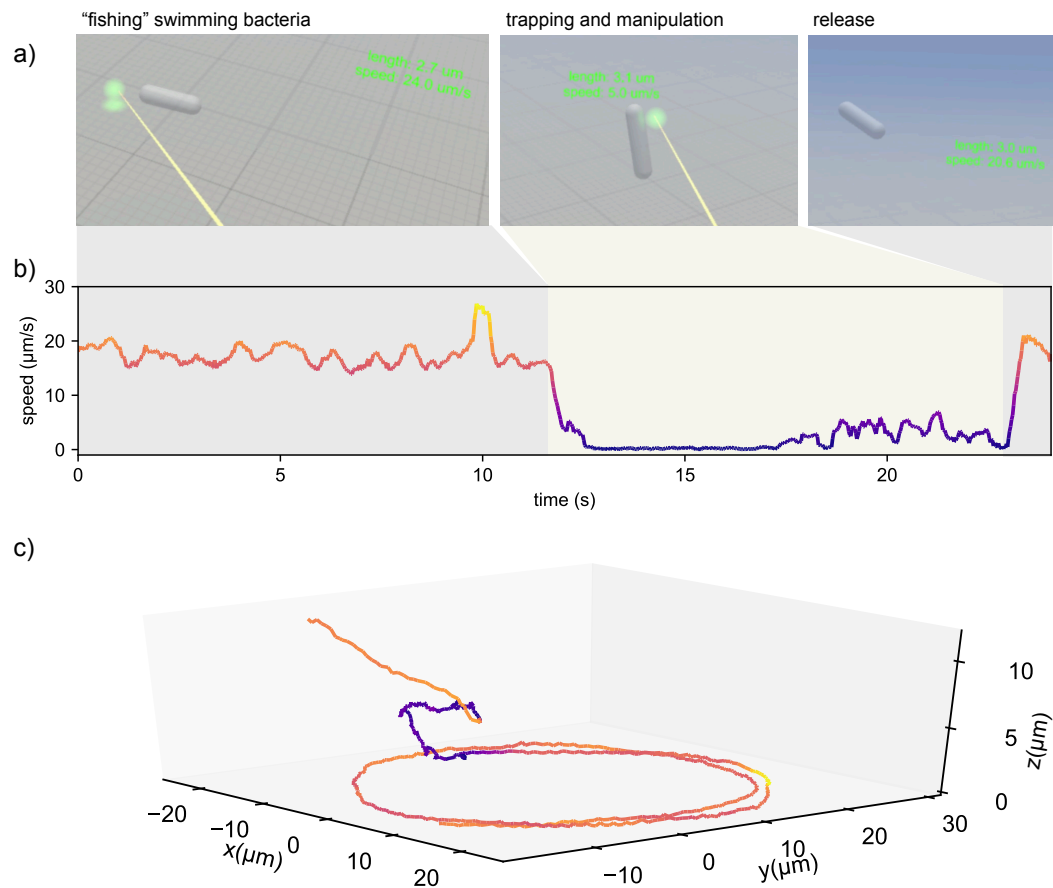


Figure 6.5. (a) These frames show the user view as he aims at a swimming *E. coli* cell, traps it and finally releases it. The VR application displays an info panel for each cell showing size and speed. (b) Cell speed as a function of time during the interaction summarized by the frames above. (c) Full 3D trajectory of the cell showing circular swimming of the free cell, trapping and manipulation (slow speed section), and finally release. The color of the curve corresponds to speed values as shown in (b).

Besides simply trapping and moving micron-sized objects, HOTs can also serve as a powerful tool to reorient prolate objects, like the body of an *E. coli* cell, in arbitrary directions. Indeed, whenever such an object is trapped, it tends to align with the trapping beam direction (*i.e.* vertically in our case). Trapping the poles of the object with two holographic tweezers and then rotating them respect to their midpoint allows its custom reorientation. In this respect, our interface facilitates a lot such duties, by providing both hand and remote control of traps together with a stereoscopic visual feedback. In Fig. 6.6 we show the example of an *E. coli* cell that has been flattened with the strategy just described.

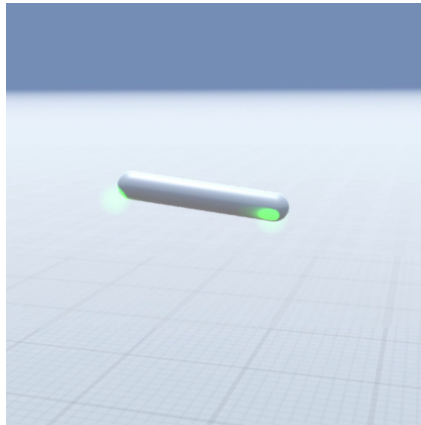


Figure 6.6. The prolate body of an *E. coli* cell is trapped with two holographic tweezers at its poles. Rotating the traps with respect to their midpoint position allows the bacterium reorientation.

6.2 Generic 3D objects

Holographic imaging of objects that, like bacteria, are comparable in size to the wavelength of light is quite a challenging task. At best, volumetric reconstructions represent the convolution of the actual object shape by a point spread function which is approximately a 3D Gaussian and which results in a blurring of the final 3D image (especially along the vertical axis). For the objects we considered so far, we have a reliable a priori information on the shape: colloids have a spherical shape, while bacteria are spherocylinders with a varying length but a pretty constant thickness. In this situation, it may be preferable to use volumetric reconstructions to infer the geometric parameters of these shapes and if we render them as perfect spheres and spherocylinders on the VR headset we get a reconstruction of the scene that is closer to reality. However, this is not always the case and there are situations where a more direct and unbiased representation of holographic reconstructions is what we want to see and interact with.

To implement that, we used the “marching cubes” (MC) algorithm [174]. This algorithm uses a divide-and-conquer approach to obtain triangle models of isosurfaces from the $512 \times 512 \times 61$ reconstructed volumetric images by deriving inter-slice connectivity. For the sake of simplicity, we first discuss the 2D version of the MC algorithm, sketched in Fig. 6.7. In order to deduce the shape of the turquoise object

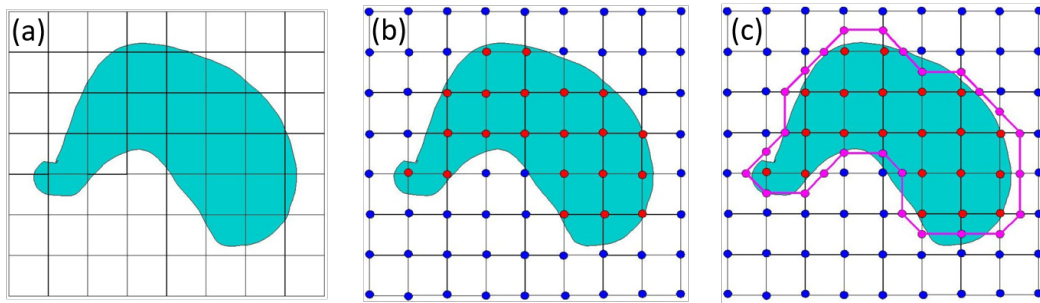


Figure 6.7. 2D version of the marching cubes algorithm to derive the shape of the turquoise object. The domain is divided into squares (a), whose vertices are differently labelled depending on whether they are inside (red) or outside (blue) the object (b). Connecting the midpoints (purple) of the edges having different colored extremes results in a first approximation of the object shape (c).

in Fig. 6.7(a), first of all the domain is divided into squares of custom size. Once labelled the squares vertices as being either inside (red) or outside (blue) the object (see panel (b)), we know that the object boundary crosses those squares edges having different colored ends. As shown in panel (c), connecting the midpoints of such edges (purple) results in a simple approximation of the object, whose roughness can be further refined. The volumetric MC algorithm is based on a similar principle. In this case, the 3D domain is divided into logical cubes of given size, whose vertices (voxels) belong four to four to two adjacent slices of the reconstructed volumetric data stack. By comparing the data values at the vertices with the isosurface value, the algorithm identifies the inner and outer vertices and locates a surface in the cube. As in the 2D case, the surface intersects those cube edges where one vertex is outside the surface and the other is inside. Since a cube has 8 vertices, each of which can assume two different states (inside and outside), there are $2^8 = 256$ ways a surface can intersect the cube. By enumerating these 256 cases, a table can be created to look up surface-edge intersections, given the labeling of a cube vertices. The table contains the edges intersected for each case. Actually, the symmetry properties of the cube allow to reduce the number of different cases to 14, in addition to the case of all vertices inside or outside the surface where no intersection is present. The permutation of these 14 fundamental patterns, shown in Fig. 6.8, using complementary and rotational symmetry produces the 256 cases just mentioned. The surface identified for each cube can be resolved into the union of multiple triangles. Once all triangles have been found, MC calculates a unit normal vector for each triangle vertex. The rendering algorithms use this normal to produce Gouraud-shaded images [175, 176].

The routine, executed on the “holographic engine” GPU, outputs a polygonal mesh, whose triangles vertices and normal vectors are sent over Ethernet to the “VR engine” for live rendering. The time taken for marching cubes algorithm to compute all polygons vertices of a given volumetric reconstruction is 3 ms, which is faster than the segmentation routine used before. Fig. 6.9 shows the raw output of the algorithm, where no kind of graphic correction has been performed. In particular, the MC algorithm applied to the reconstructed volumes of 4 beads of $1 \mu\text{m}$ radius (a) and a trapped *E. coli* cell (c) returns the meshes in panels (b) and (d), respectively. The

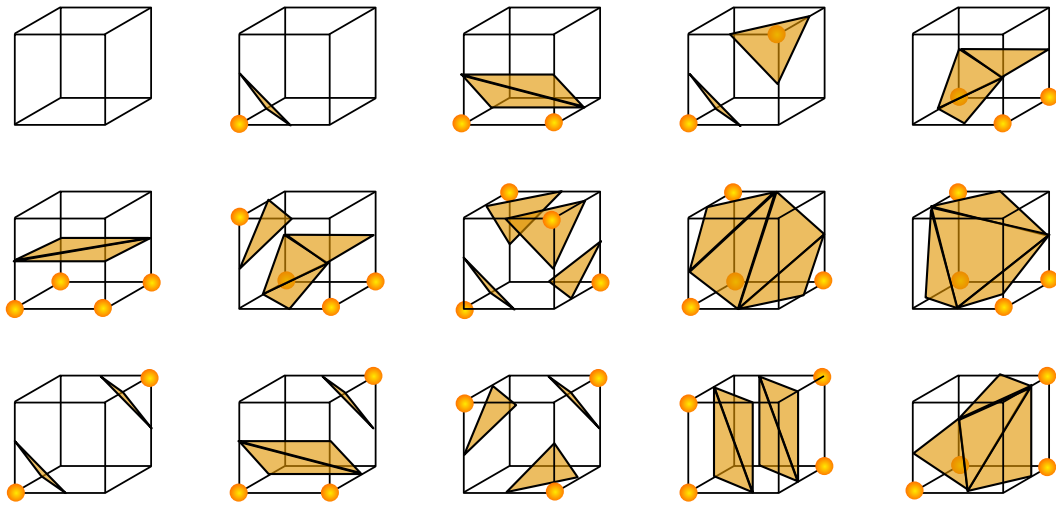


Figure 6.8. Fundamental 14 surface patterns to compute an isosurface mesh with marching cubes algorithm. When all vertices are inside/outside the isosurface, the latter does not intersect the cube (first example).

volumetric images in panels (a) and (c), which describe the same samples discussed in § 4.2, have been reported here again for the sake of clarity. This figure shows the

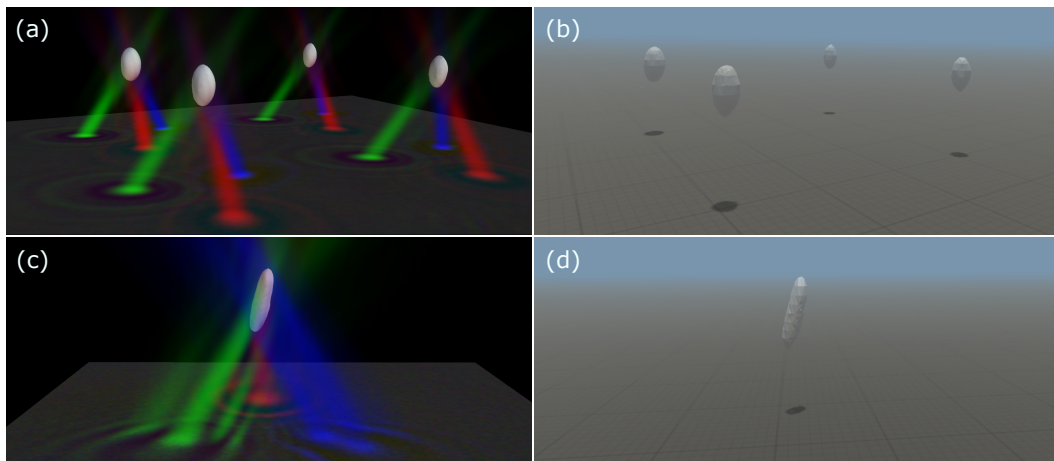


Figure 6.9. Reconstructed volumes of 4 colloidal beads of $1\ \mu\text{m}$ radius (a) and a trapped *E. coli* bacterium (c) and respective isosurfaces meshes (b,d) returned by the marching cubes algorithm.

raw triangle model the algorithm computes. The quality of the mesh can be refined by reducing the triangles dimension, although this option results in a much heavier computational task that hinders the live visual feedback. A more efficient solution is to act on the shading defined by the outward normal vector associated to each vertex. All triangles of the mesh share their vertices with adjacent triangles. Each vertex in common can be represented in the game engine in two different ways. The first possibility is to consider as many vertices (with equal coordinates) as the number of triangles converging in the same corner point. In this case, each vertex assumes the

normal vector of the triangular facet it is part of and the mesh appears discrete as in Fig. 6.9. The strategy we implemented to improve the quality of objects shading exploits a different encoding protocol of the mesh in which no repetitions are present, but every vertex is simultaneously part of all its adjacent triangles. In this case, the normal vector applied to each vertex is the mean of all adjacent facets normal vectors, resulting in a smoothing effect of the mesh, as shown in Fig. 6.10. As a benchmark for this imaging method, we show in this figure the real-time immersive exploration of a sample crowded with swimming bacteria. The comparison between Figs. 6.10(a) and (b), moreover, proves that our interface allows to optimize the information extracted from such a complex sample respect to a classical bright field microscopy view. Indeed, Fig. 6.10(b) shows highly diffracted images of *E. coli* cells, which appear black or white depending on their z location, but whose precise location and orientation can be unveiled only with further image processing.

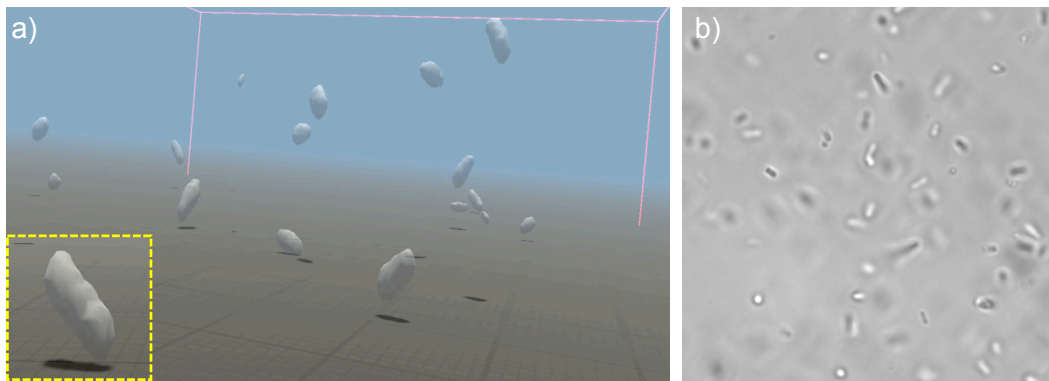


Figure 6.10. (a) Real-time mesh rendering of swimming *E. coli* bacteria. The reconstructed volumetric density in the entire field of view is segmented by an isosurface. A close view of an individual cell is shown in the highlighted square panel. (b) For comparison we show a bright field microscopy image of the same bacteria.

6.3 Eukaryotic cells

We now show as an example the exploration of a sample populated by living eukaryotic cells interacting on the glass substrate, which requires our system to be updated by integrating a different imaging technique. As bacteria discussed above, most living cells show extremely weak absorption in the visible spectrum, resulting in very low-contrast images under light microscopy [177]. Under certain circumstances, microscopy images may gain contrast from light scattering rather than absorption, depending on the thickness and refractive index inhomogeneity of the sample. However, the light scattered by biological specimens like single cells or thin tissue slices is orders of magnitude weaker than the incident light, so that revealing the sample is a challenging task. A technique that is not affected by these impediments is fluorescence microscopy, which has become the main tool of investigation in cell biology [178]. Due to the significant progress in designing fluorescence tags, structures in the cell can now be imaged with high specificity. However, even fluorescence imaging is subject to several limitations. Absorption

of the excitation light may cause the fluorophore to irreversibly alter its molecular structure and stop fluorescing. This process, known as photo-bleaching, limits the time interval over which continuous imaging can be performed [179]. Furthermore, the excitation light is typically toxic to cells, a phenomenon referred to as photo-toxicity [180]. Label-free microscopy provides an alternative solution to overcome these limitations, albeit at the expense of molecular specificity. The experiments discussed so far largely promote holographic microscopy as a powerful label-free technique for fast 3D imaging. However, due to the weak light scattering produced by thin biological specimens laying on a substrate, more suitable strategies are favored. Since such samples significantly affect the phase of light, the information on their structure is encoded in the modifications of the incident beam wavefront upon propagation through the sample. The spatially dependent phase shift is defined as

$$\Delta\phi(x, y) = \frac{2\pi}{\lambda} \int \Delta n(x, y, z) dz \quad (6.1)$$

where λ is the central wavelength of the illumination (orthogonal to sample plane), (x, y) and z are the coordinates on the image plane and along the optical axis, respectively, and Δn is the sample refractive index difference respect to the surrounding medium. Two classical methods that investigate such a wavefront modulation are phase contrast microscopy [181] and differential interference contrast (DIC) microscopy [182, 183], even though they both return qualitative results. A different approach focused precisely on measuring the phase shift $\Delta\phi(x, y)$ is quantitative phase imaging (QPI) [184], which provides a quantitative spatial map of sample thickness. This technique is complementary to established fluorescence microscopy, but as a label-free strategy it exhibits lower photo-toxicity and no photo-bleaching.

In the last period of my PhD, we implemented in our interface the real-time virtual rendering of more complex eukaryotic cells. The cell structure is reconstructed using a new QPI method that combines DIC microscopy with low-coherence interferometry and holography [185]. This label-free technique, referred to as gradient light interference microscopy (GLIM), can follow the dynamics of living cells over broad temporal scales, since it is not affected by typical fluorescence microscopy limitations. The setup designed for GLIM, shown in Fig. 6.11, implements the typical Köhler geometry for sample illumination [186]. The light of a LED source ($\lambda = 530$ nm) is collimated with a collector lens (L_1) and focused on the sample (S) with a condenser lens (L_2), whose numerical aperture can be regulated with an iris diaphragm (D) in its back focal plane. Thus, the illumination field is

$$\mathbf{E}_0 = E_0 e^{i\phi_0} \hat{\epsilon}_0 \quad (6.2)$$

where $E_0 = |\mathbf{E}_0|$, the phase ϕ_0 defines the incident wavefront and the versor $\hat{\epsilon}_0$ stands for the undefined polarization state. A $60\times$ microscope objective (NA = 1), coupled with a 200 mm tube lens (TL), magnifies the field after it propagates through the sample. Such a field can be described by means of the modulated phase pattern $\phi(\mathbf{r}) = \phi_0 + \Delta\phi(\mathbf{r})$ as

$$\mathbf{E}_1 = E_0 e^{i\phi(\mathbf{r})} \hat{\epsilon}_0 \quad (6.3)$$

where $\mathbf{r} = (x, y)$. After reflecting on a mirror (M), the beam is spatially Fourier-transformed with the lens L_3 and impinges on a SLM with vertical active axis in

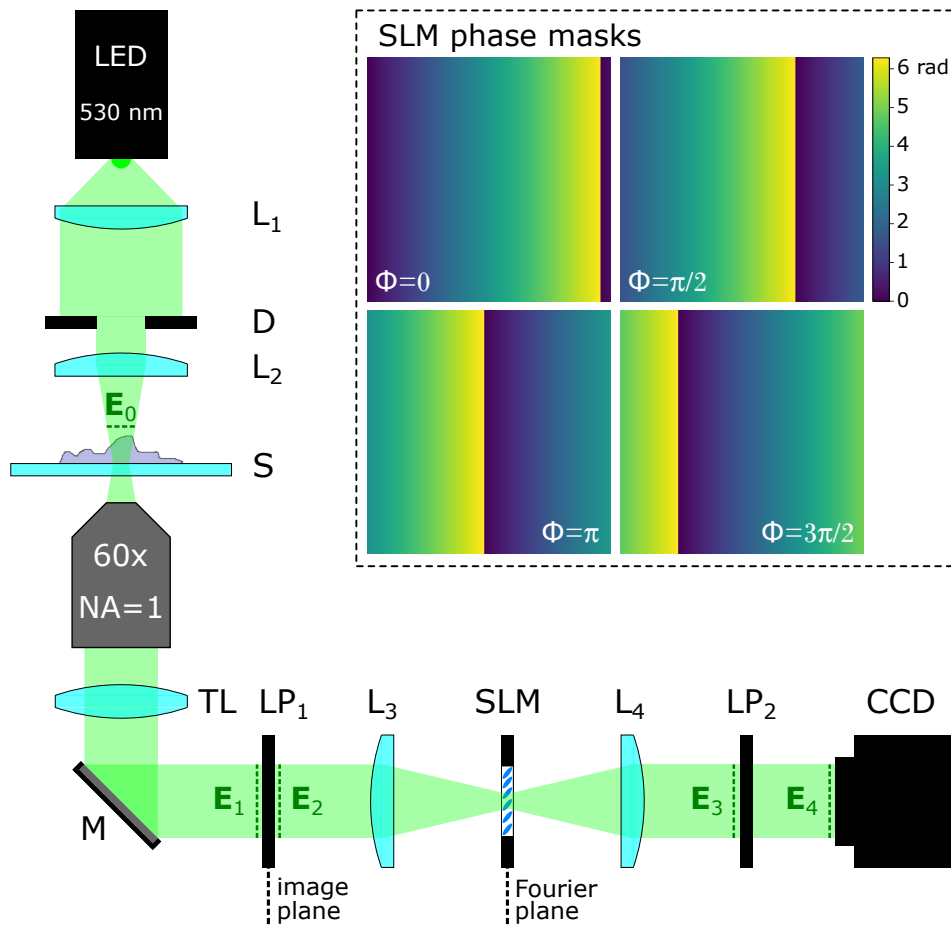


Figure 6.11. GLIM setup. The incoherent and unpolarized light of a 530 nm LED source illuminates the sample (S) after being shaped by a collimator-condenser pair (L_1 - L_2); the condenser numerical aperture is regulated with an iris diaphragm (D). A $60\times$ microscope objective ($NA = 1$) is coupled with a 200 mm tube lens (TL) so that a magnified image of the field is obtained on the image plane. A linear polarizer (LP_1) filters the light along an axis tilted by 45° respect to the SLM liquid crystal axis (*i.e.* the vertical axis). The vertical component $\hat{\epsilon}_V$ of the polarized field is modulated by the SLM, while the horizontal component $\hat{\epsilon}_H$ is not. Both the $\hat{\epsilon}_H$ and $\hat{\epsilon}_V$ component pass through the polarizer LP_2 , whose axis parallel to LP_1 allows them to interfere on the camera plane. The SLM is placed on the Fourier plane; the field \mathbf{E}_2 is Fourier-transformed by the lens L_3 and, after being modulated, is back-transformed by L_4 . The SLM applies an offset Φ to retard the phase, plus a linear grating $\mathbf{q} \cdot \mathbf{r}$ to shift the modulated field by $\mathbf{\Lambda} = \mathbf{q} \lambda f / 2\pi$ on the image plane (f is L_3 and L_4 focal length). The inset shows four SLM phase masks that shift the $\hat{\epsilon}_V$ polarization of $\Lambda_x = +0.3 \mu\text{m}$ and retard the wavefront of $\Phi = [0, \pi/2, \pi, 3\pi/2]$.

the Fourier plane. As in typical DIC methodology, imaging the sample relies on the coherent superposition of two laterally-shifted replicas of the field in the image plane. In this respect, a tailored phase mask displayed on the SLM can modulate the vertically-polarized portion of the imaging light, while the horizontally-polarized portion propagates unmodified. Both the modulated and unmodified component of the field are then Fourier-transformed again by means of lens L_4 and imaged with a

digital camera. However, since the LED source emits incoherent light, this method would result in the mere summation of two distinct intensities in the image plane, also because of their cross polarizations. In order to achieve suitable interference conditions, we introduced in our setup a pair of linear polarizers (LP₁, LP₂) before lens L₃ and after lens L₄, respectively, with both axes rotated by 45° respect to the SLM vertical axis. The light after LP₁ presents a diagonal linear polarization and can be described as

$$\mathbf{E}_2 = \frac{1}{\sqrt{2}} E_1 \hat{\epsilon}_D = \frac{1}{\sqrt{2}} E_0 e^{i\phi(\mathbf{r})} \hat{\epsilon}_D \quad (6.4)$$

where the versor $\hat{\epsilon}_D$ describes the diagonal polarization at 45° and the coefficient $1/\sqrt{2}$ is due to the fact that only half of the unpolarized beam power passes through the polarizer (whatever its axis). The diagonally-polarized field can be resolved into its components with horizontal ($\hat{\epsilon}_H$) and vertical ($\hat{\epsilon}_V$) polarizations as follows:

$$\mathbf{E}_2 = \frac{1}{\sqrt{2}} E_0 e^{i\phi(\mathbf{r})} \left(\frac{1}{\sqrt{2}} \hat{\epsilon}_H + \frac{1}{\sqrt{2}} \hat{\epsilon}_V \right) = \frac{1}{2} E_0 e^{i\phi(\mathbf{r})} \hat{\epsilon}_H + \frac{1}{2} E_0 e^{i\phi(\mathbf{r})} \hat{\epsilon}_V \quad (6.5)$$

The terms of such summation represent two orthogonally-polarized fields that, as components of the same global field \mathbf{E}_2 , are now coherent. The phase hologram the SLM displays to modulate the $\hat{\epsilon}_V$ component of the field is obtained by combination of a constant offset $\Phi = [0, \pi/2, \pi, 3\pi/2]$ to retard the wavefront and a linear grating $\mathbf{q} \cdot \mathbf{r}$ resulting in a lateral shift in the image plane of $\mathbf{\Lambda} = (\Lambda_x, \Lambda_y) = \mathbf{q} \lambda f / 2\pi$, where f is the focal length of lenses L₃ and L₄ (see inset in Fig. 6.11). The field thus modulated and Fourier-transformed by lens L₄ is

$$\mathbf{E}_3 = \frac{1}{2} E_0 e^{i\phi(\mathbf{r})} \hat{\epsilon}_H + \frac{1}{2} E_0 e^{i[\phi(\mathbf{r}+\mathbf{\Lambda})+\Phi]} \hat{\epsilon}_V \quad (6.6)$$

The polarizer LP₂ before the camera filters the projections of both $\hat{\epsilon}_H$ and $\hat{\epsilon}_V$ component along its axis $\hat{\epsilon}_D$, so to render them parallel and allow their interference in the camera plane. Here the field is

$$\mathbf{E}_4 = \frac{1}{2\sqrt{2}} E_0 \left\{ e^{i\phi(\mathbf{r})} + e^{i[\phi(\mathbf{r}+\mathbf{\Lambda})+\Phi]} \right\} \hat{\epsilon}_D \quad (6.7)$$

where the power results halved again due to the second polarizer action. The final intensity pattern recorded by the camera is

$$\begin{aligned} I_\Phi = |\mathbf{E}_4|^2 &= \frac{E_0^2}{8} \left\{ e^{i\phi(\mathbf{r})} + e^{i[\phi(\mathbf{r}+\mathbf{\Lambda})+\Phi]} \right\} \left\{ e^{-i\phi(\mathbf{r})} + e^{-i[\phi(\mathbf{r}+\mathbf{\Lambda})+\Phi]} \right\} = \\ &= \frac{E_0^2}{4} \{ 1 + \cos [\phi(\mathbf{r} + \mathbf{\Lambda}) - \phi(\mathbf{r}) + \Phi] \} \approx \\ &\approx \frac{E_0^2}{4} \{ 1 + \cos [\nabla\phi(\mathbf{r}) \cdot \mathbf{\Lambda} + \Phi] \} \end{aligned} \quad (6.8)$$

where the last approximation is valid for small magnitudes of vector $\mathbf{\Lambda}$. We consider now the case of a shift $\mathbf{\Lambda}$ oriented either along x or y axis, for example $\mathbf{\Lambda} = \Lambda_x \hat{x}$. For fixed magnitude Λ_x , four images of the same sample can be sequentially acquired with the four values of Φ stated before. With such phase offsets, the recorded

intensities are

$$I_0 = \frac{E_0^2}{4} \{1 + \cos [\nabla_x \phi(\mathbf{r}) \cdot \Lambda_x]\} \quad (6.9)$$

$$I_{\frac{\pi}{2}} = \frac{E_0^2}{4} \left\{1 + \cos \left[\nabla_x \phi(\mathbf{r}) \cdot \Lambda_x + \frac{\pi}{2} \right]\right\} = \frac{E_0^2}{4} \{1 - \sin [\nabla_x \phi(\mathbf{r}) \cdot \Lambda_x]\} \quad (6.10)$$

$$I_\pi = \frac{E_0^2}{4} \{1 + \cos [\nabla_x \phi(\mathbf{r}) \cdot \Lambda_x + \pi]\} = \frac{E_0^2}{4} \{1 - \cos [\nabla_x \phi(\mathbf{r}) \cdot \Lambda_x]\} \quad (6.11)$$

$$I_{\frac{3}{2}\pi} = \frac{E_0^2}{4} \left\{1 + \cos \left[\nabla_x \phi(\mathbf{r}) \cdot \Lambda_x + \frac{3}{2}\pi \right]\right\} = \frac{E_0^2}{4} \{1 + \sin [\nabla_x \phi(\mathbf{r}) \cdot \Lambda_x]\} \quad (6.12)$$

where $\nabla_x \phi(\mathbf{r}) = \frac{\partial}{\partial x} \phi(\mathbf{r})$. These four frames can be combined to retrieve the gradient of the phase $\phi(\mathbf{r})$ along x as

$$\nabla_x \phi(\mathbf{r}) = \frac{1}{\Lambda_x} \arctan \left[\frac{I_{\frac{3}{2}\pi} - I_{\frac{\pi}{2}}}{I_0 - I_\pi} \right] \quad (6.13)$$

The gradient of the phase in the orthogonal direction $\nabla_y \phi(\mathbf{r})$ can be retrieved as well from the same combination of four equivalent intensity patterns acquired with the $\hat{\epsilon}_V$ polarization shifted of $\mathbf{\Lambda} = \Lambda_y \hat{y}$. Both gradient components $\nabla_x \phi(\mathbf{r})$ and $\nabla_y \phi(\mathbf{r})$ can be individually differentiated again along x and y , respectively, in order to compute the Laplacian of the phase as

$$\nabla^2 \phi(\mathbf{r}) = \frac{\partial^2}{\partial x^2} \phi(\mathbf{r}) + \frac{\partial^2}{\partial y^2} \phi(\mathbf{r}) = \nabla_x (\nabla_x \phi(\mathbf{r})) + \nabla_y (\nabla_y \phi(\mathbf{r})) \quad (6.14)$$

Thanks to the properties of the Fourier transform [80, 86], the latter operation can be applied twice to the Laplacian in order to obtain the original phase pattern $\phi(\mathbf{r})$ as

$$\phi(\mathbf{r}) = \mathcal{F}^{-1} \left\{ -\frac{1}{k_t^2} \mathcal{F} \left\{ \nabla^2 \phi(\mathbf{r}) \right\} \right\} \quad (6.15)$$

where k_t is the transverse wavevector. In order to extract the phase shift term $\Delta \phi(\mathbf{r}) = \phi(\mathbf{r}) - \phi_0$, the incident wavefront profile ϕ_0 is retrieved by processing through the passages just described an equal set of background intensity patterns recording an empty field of view. The height map of samples whose refractive index is almost homogeneous can now be easily computed through the inverse of Eq. 6.1.

As an example, we show the results of a study on Microglia cells, whose dynamics was analysed by imaging the specimen every 30s. For the sake of symmetry upon reconstruction, we repeatedly acquire the four images described by Eqs. 6.9–6.12 for four different lateral shifts of the vertically-polarized field, two along x and two along y axis ($\Lambda_{x,y} = \pm 0.3 \mu\text{m}$). For every choice of Φ and $\mathbf{\Lambda}$, an empty background image is also recorded. The inset in Fig. 6.11 shows the example of the typical four phase masks shifting the vertically-polarized light of $+0.3 \mu\text{m}$ along x axis. To this aim, the constant offset Φ is added (modulo 2π) to a grating pattern, which has a large pitch due to the tiny translation required. We can notice that, as the offset increases from 0 to $3\pi/2$, the vertical edge signaling where the hologram assumes value 2π shifts to the left. We report in Fig. 6.12 the images of some interacting Microglia cells acquired with the $\hat{\epsilon}_V$ component of light positively shifted along y . The images

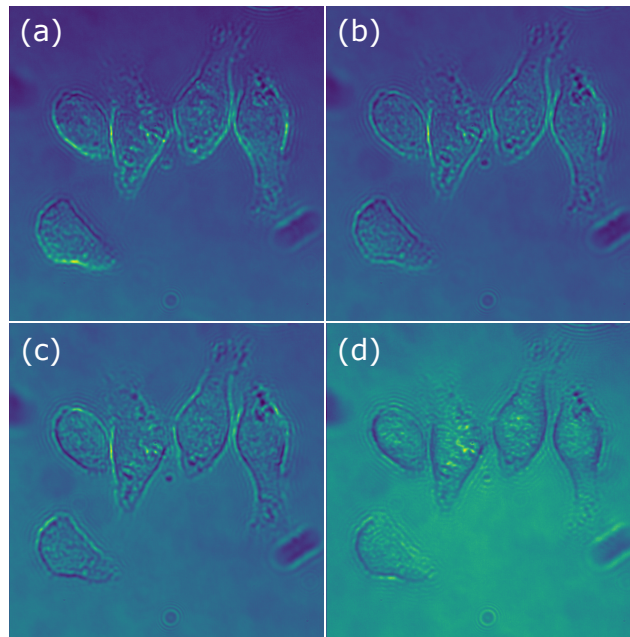


Figure 6.12. Images of five Microglia cells recorded with the typical phase offset Φ of 0 (a), $\pi/2$ (b), π (c), and $3\pi/2$ (d), and the vertically-polarized field shifted of $\Lambda_y = +0.3 \mu\text{m}$.

are arranged in ascending order of Φ from 0 (a) to $3\pi/2$ (d). Such intensities are combined as described by Eq. 6.13 to get the phase gradient along y . Actually, this pattern is averaged with the one obtained from the other four frames acquired with negative y shift, resulting in the global phase gradient along y , shown in Fig. 6.13(b). The eight figures related to both positive and negative shift along x are processed in the same way, resulting in the x component of the global phase gradient, shown in Fig. 6.13(a). The merger of such 2D arrays provides the global phase gradient modulus $|\nabla\phi(\mathbf{r})| = \sqrt{[\nabla_x\phi(\mathbf{r})]^2 + [\nabla_y\phi(\mathbf{r})]^2}$, shown in Fig. 6.13(c). Following the

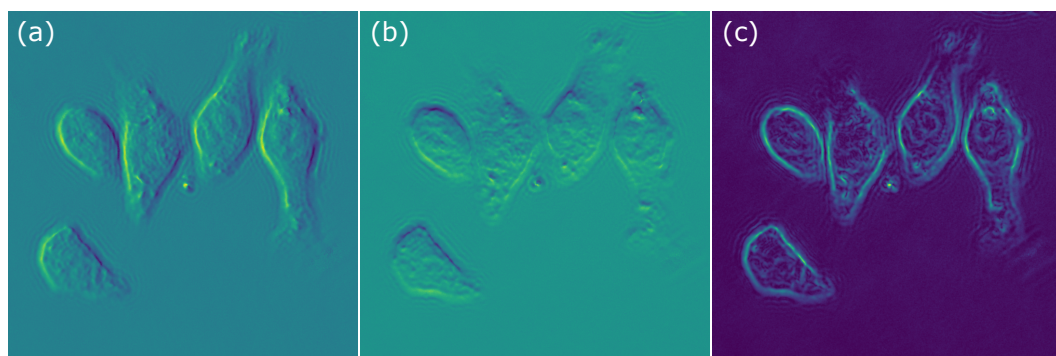


Figure 6.13. Gradient of the wavefront modulated by the cells sample along x (a) and y (b), and global phase gradient modulus deduced by combination of these two components (c).

calculations discussed before, the Laplacian pattern can be deduced as described by Eq. 6.14 and integrated twice as in Eq. 6.15, in order to finally retrieve the

modulated phase $\Delta\phi(\mathbf{r})$, displayed in Fig. 6.14(a). From this image we can clearly distinguish individual cells edges as well as some of their intra-cellular structures. However, the perception of cells thickness is still indirect, since it is encoded in the color map. We exploited the power of our innovative instrument to facilitate this task. As the “VR engine” receives the 2D height map obtained from the modulated phase $\Delta\phi(\mathbf{r})$, it updates the rendering of a terrain game object, which is coloured as well in function of its height, as shown in Fig. 6.14(b). The virtual environment allows to move around the cells to analyze their dynamics and interactions from multiple perspectives, providing a better view also on cells morphological features.

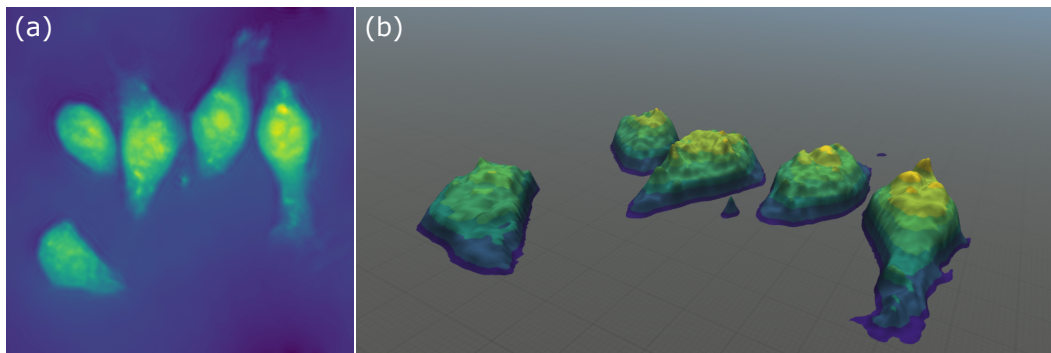


Figure 6.14. Final reconstructed phase $\Delta\phi(\mathbf{r})$ for cells imaging (a), and 3D rendering of the sample with our VR interface (b).

Chapter 7

An optical reaction micro-turbine

In these 3 years of research I have also been involved in some other projects besides the main one. During the first year of my PhD, in particular, I contributed to develop the design of an optical reaction micro-turbine that could maximally exploit light's momentum to generate a strong, uniform, and controllable torque. Such a light guiding structure, fabricated by direct laser writing, is shaped as a garden sprinkler and can precisely reroute input optical power into multiple output channels. Part of this project was published in Ref. [187].

Introduction

Turbines are a large class of turbo-machines that transfer energy from a working fluid, typically water, air, or steam, to a continuously rotating system, the rotor. Despite the large variability in turbine designs and working fluids, torque generation always results from the continuous angular momentum change of the working fluid that flows through them. In the same way, microscopic turbines can use light as a working fluid and generate a torque by redirecting the flow of optical energy through them, so that outgoing light has a different angular momentum than incoming light. Both for a macroscopic hydraulic turbine or a microscopic optical turbine the generated torque will be then given by the difference in the rate of incoming and outgoing angular momentum, that in the optical case reads:

$$T_z = \frac{nP}{c} \left(k_\phi^{\text{out}} r^{\text{out}} - k_\phi^{\text{in}} r^{\text{in}} \right) \quad (7.1)$$

where P is the optical power, n is the refractive index of the surrounding medium, z is the direction of the rotor axis, ϕ the azimuthal coordinate, k_ϕ^{in} and k_ϕ^{out} the azimuthal components of respectively incoming and outgoing light directions and r^{in} and r^{out} the radial distances of inlet and outlet (Fig. 7.1(a)). Eq. 7.1 is formally very similar to the Euler turbo-machine equation [188] expressing torque in hydraulic turbines and where P is replaced by mass flow and nk_ϕ^{in}/c , nk_ϕ^{out}/c by the azimuthal components of inlet and outlet velocities. In the optical case, however, although incoming light will often be a focused laser beam with a well defined inlet point and

propagation direction, outgoing light results from a complex scattering interaction and cannot be associated with unique values of k_ϕ^{out} and r^{out} . However, because of its fundamental character, Eq. 7.1 can still be used to put an upper bound to the torque that an optical turbine can generate. In the case of axial turbines where incoming light propagates in the z direction ($k_\phi^{\text{in}} = 0$), the maximum achievable torque is:

$$T_{\text{max}} = \frac{nP}{c}r \quad (7.2)$$

corresponding to all outgoing light emerging with tangential direction ($k_\phi^{\text{out}} = 1$) from the turbine point having the largest distance from the axis (r). Different designs for optical turbines have been proposed in recent literature. The so-called “light mill” [189,190] is an axial turbine with a propeller-shaped 3D micro-rotor. A central rod component guarantees stable trapping and alignment along the axis of a focused tweezer beam while tilted radial arms scatter light with a nonzero component of orbital angular momentum. In Ref. [189] it is shown that a beam with power $P = 10$ mW could spin a $r = 3$ μm structure at an angular frequency of $\omega = 7$ rad/s. The corresponding optical torque will balance the hydrodynamic viscous torque $T = \gamma\omega \sim 1$ pN μm , where we used for the rotational drag coefficient $\gamma = 0.2$ pN $\mu\text{m s rad}^{-1}$ as estimated for a very similar structure in Ref. [189]. Using Eq. 7.2, we find that the maximum achievable torque is $T_{\text{max}} = 136$ pN μm . The resulting torque efficiency, defined as the ratio T/T_{max} is $< 1\%$. Similarly to light-mills, micro-structures of different shapes can exploit chirality to generate torque. Among them, cylinders [191] with slanted bases or chiral crosses [192,193] could only generate a torque that is two orders of magnitude smaller than the maximum value.

Another proposed design for an optical turbine is the paddle-wheel [194] that, as an optical equivalent of a Pelton turbine, employs a non-chiral structure and an off-axis pushing beam. The structure consists of four paddles connected to a central axis with two spheroids at its extremities. The two spheroids serve as handles for optical trapping while the paddles recoil by partially reflecting a low divergence beam thus causing the rotation of the entire structure. From the reported values for drag $\gamma = 5.3$ pN $\mu\text{m s rad}^{-1}$, power $P = 6$ mW and angular speed $\omega = 1.8$ rad/s [194] we estimate an optical torque of $T = \gamma\omega = 9.5$ pN μm . This design results in an improved torque efficiency (10% of the maximal value $T_{\text{max}} = 106$ pN μm , excluding the power in the trapping beams) although rotations are strongly non uniform. Other optical turbines, employing symmetric rotors like the paddle-wheel, rely on structured wavefront of the beam to generate torque. Laguerre–Gauss beams have been employed for this purpose giving a ratio between torque and T_{max} that is comparable [195] (~ 0.01) or lower [196] ($\sim 10^{-3}$) than the above cited cases.

Finally, birefringent particles can generate torque through the exchange of the spin component of optical angular momentum [197–200]. The maximum achievable torque in this case is $P\lambda/\pi c$ that is only a fraction $\lambda/\pi nr$ of the maximum torque in Eq. 7.2 (from Ref. [200] we compute a torque efficiency of the order of 10^{-3}). Despite a small torque efficiency, high rotation rates can be still obtained with this method provided that the rotational drag is very low as in the case of small particles [198] or low viscosity fluids [199,200]. Here we are interested in maximizing the efficiency of conversion from optical power to torque so that, in the following, we will only

focus on strategies exploiting the orbital angular momentum of light.

Both the light-mill and the paddle-wheel are close analogues of hydraulic impulse turbines where the working fluid, moving in free-space, impacts on the turbine blades transferring impulse. In a different class of turbines, called reaction turbines, the working fluid is always enclosed in the blade system which, by deflecting the incoming mass flow, recoils by reaction forces.

Here we designed a light-guiding structure made of SU8 photoresist with a chiral shape resembling that of a garden sprinkler. By replacing scattering with guided light propagation inside micro-fibers we could reroute most of the incoming light onto outlet points located at the radial periphery of the structure and from which light emerges in a tangential direction. With such a design we maximize the reaction torque that is of the same order of magnitude of the ideal maximum value.

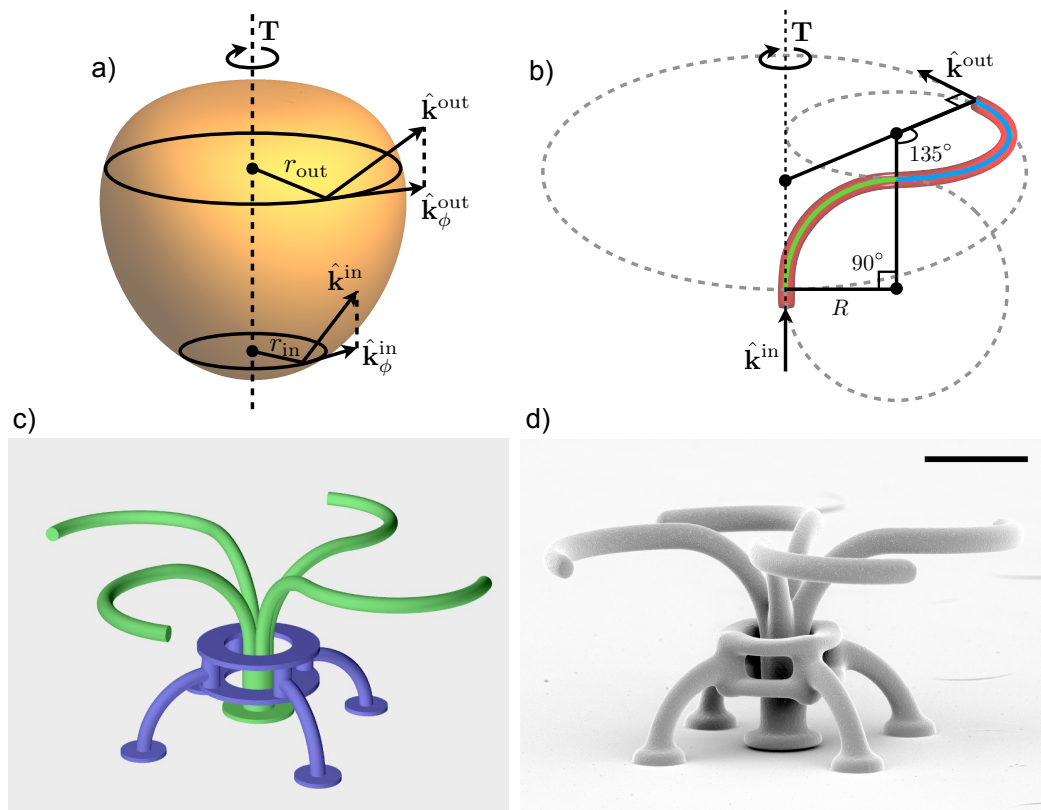


Figure 7.1. Micro-turbine design. (a) A schematic representation of the generic working principle of torque generation in turbines. The working fluid enters and leaves the rotor with directions and radial distances indicated respectively with $\hat{\mathbf{k}}^{in,out}$ and $r^{in,out}$. The optical torque is given by the difference between the input and output flux of angular momentum $\mathbf{T} = (nP/c) (\hat{\mathbf{k}}^{out} \times \mathbf{r}^{out} - \hat{\mathbf{k}}^{in} \times \mathbf{r}^{in})$. (b) 3D shape of the curved arms. The arm is composed of two circular arcs: the first (green) redirects light from axial to radial direction while the second (blue) from radial to tangential. (c) 3D computer model of the designed structure. The stator, which is anchored to the cover glass, is highlighted in blue while the rotor, composed by a waveguide splitting into four curved arms, is highlighted in green. (d) Scanning electron microscopy image of a micro-turbine (scale bar is $10 \mu\text{m}$).

Bend losses

The structure starts with a larger circular core ($4\ \mu\text{m}$) oriented in the axial \hat{z} direction (see Fig. 7.1(c)). The input fiber then splits into four $2\ \mu\text{m}$ cores that guide light towards outlet fiber tips oriented in the azimuthal direction $\hat{\phi}$ (Fig. 7.1(c)). If all available light could be coupled into the structure and propagate all the way to the outlets with no losses, this design would achieve the theoretical maximal torque in Eq. 7.2. We know, however, that three main causes of losses are present in our structures: coupling, splitting, and bending.

Bend losses, although always present in curved optical fibers, decrease exponentially with the curvature radius R [201, 202] becoming negligible for macroscopic bends ($R \sim 1\ \text{cm}$). However, a microscopic optical turbine will need to redirect incoming light within a small propagation distance by using optical fibers with curvature radii in the micron range. Although bend losses have been widely studied in literature [202–204], scaling those results to the range of micrometric curvature radii is not straightforward and potentially inaccurate due to breaking of typical approximations.

To get a direct and accurate evaluation of bend losses, we used direct laser writing via two-photon polymerization [7, 8] to fabricate a set of 180° arches having a constant radius of curvature R and a circular cross-section with diameter $2a = 2\ \mu\text{m}$. Both the input and output facets of the fiber arches lie on the coverslip surface plane allowing us to use the same objective ($20\times$, $\text{NA} = 0.5$) to couple light in and collect output light. A laser beam ($\lambda = 1064\ \text{nm}$) is focused at the center of the input core while the transmitted light is imaged with a digital camera (Fig. 7.2(a)). Transmitted power is recorded by integrating light intensity over a circular region that is about twice the size of the fiber core. We repeated the procedure for 5 arches having the same curvature radius and for a total of 10 radii. The laser power that is actually coupled to each fiber arc is unknown but the same for every R since it only depends on the core diameter and input beam shape. Therefore, we only know transmission versus R within a common normalization factor that is chosen to best match theory and simulation at large R values (see Fig. 7.2(b)). A strong decrease in transmission is observed for curvature radii smaller than $10\ \mu\text{m}$ while a slower decrease is observed at larger radii. A similar two step decay is obtained using the analytical formula derived in Ref. [202], (dashed line in Fig. 7.2(b)) a refined version of the theory proposed by Marcuse [201]. The formula predicts losses in each mode so we first need to find excited modes in our fibers. If straight, our fibers would support three guided modes (LP_{01} , LP_{02} , and LP_{11}) of which only the first two are excited by our focused laser beam ($\text{NA} = 0.5$, $\text{FWHM} = 2.3\ \mu\text{m}$), with the first mode taking about 70% of guided light. The largest drop of transmission at about $R = 10\ \mu\text{m}$ is due to the first mode (LP_{01}) while the slow transmission decrease at larger R is due to the second mode (LP_{02}).

When comparing quantitative values, however, strong deviations between theory and experiment are found for $R < 20\ \mu\text{m}$. This is not so surprising when we consider that analytical predictions were based on approximations like weak guiding and large curvature radius ($R \gg a$) which may not be valid in the present case. A closer theoretical description can be obtained by numerical simulations with 3D scalar Beam Propagation Method (BPM) [205]. We first write the Helmholtz equation for

the field E using a cylindrical coordinate system (ρ, ϕ, z) as shown in Fig. 7.2(a):

$$\left[\frac{\partial^2}{\partial z^2} + \frac{1}{\rho^2} \frac{\partial^2}{\partial \phi^2} + \frac{1}{\rho} \frac{\partial}{\partial \rho} \rho \frac{\partial}{\partial \rho} + n^2 k_0^2 \right] E = 0 \quad (7.3)$$

where $k_0 = 2\pi/\lambda$ is the wavenumber in vacuum. A common method for simulating a bent waveguide with BPM prescribes a coordinate transformation from the cylindrical coordinate system to a curvilinear coordinate system ($u = R \log(\rho/R)$, $s = R\phi$, $z' = z$). Under such a transformation, the Helmholtz equation is written as:

$$\left[e^{2u/R} \frac{\partial^2}{\partial z'^2} + \frac{\partial^2}{\partial s^2} + \frac{\partial^2}{\partial u^2} + \left(e^{u/R} n \right)^2 k_0^2 \right] E = 0 \quad (7.4)$$

The coordinate transformation has the effect of mapping n onto an effective refractive index $ne^{u/R}$ (see Fig. 7.2(a)). As the effective refractive index increases with u , evanescent tails of the guided modes can leak outside of the core leading to power losses. If the term multiplying the partial derivatives in z is neglected (*i.e.* $e^{2u/R} \frac{\partial^2}{\partial z'^2} \approx \frac{\partial^2}{\partial z'^2}$), the system can be simulated using a standard BPM algorithm [205] where the propagation direction is s while u and z' are discretized on a grid. However, since our waveguides have a large curvature (small R), we modified the BPM algorithm to simulate Eq. 7.4 without approximations. Results are plotted as solid lines in Fig. 7.2(b) showing a remarkably good agreement with experimental findings.

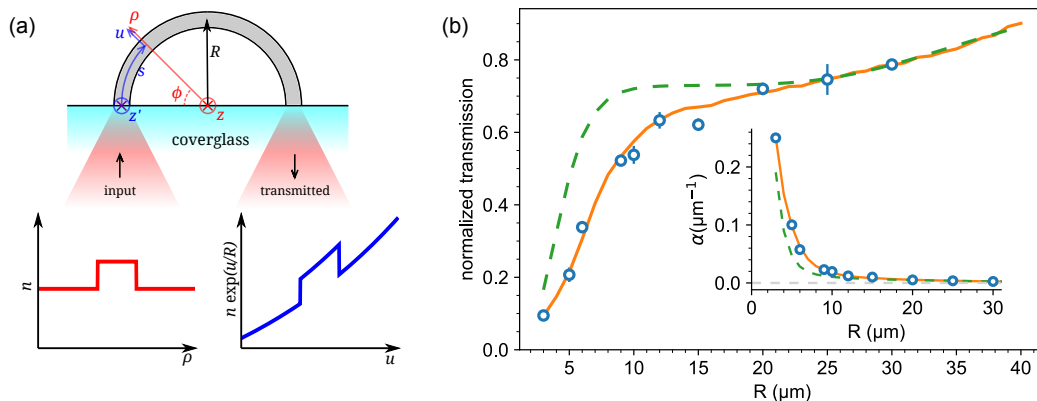


Figure 7.2. Bend losses. (a) An infrared laser beam is coupled into one end of a 180° fiber arc to measure attenuation of light transmitted to other fiber end. The red line represents the refractive index (n) profile along the radial coordinate ρ . Propagation in curved fibers can be mapped into a straight fiber problem with the effective refractive index shown by the blue line. (b) Transmitted power as a function of the arc curvature radius. Experimental data are shown as circles. Error bars represent the standard deviation between the transmission of 5 arches with same curvature. BPM simulations and analytical prediction are plotted as solid orange and dashed green lines, respectively. Inset shows the attenuation coefficient per unit length obtained from transmission data in the main panel. Gray dashed line is a guide to the eye representing the axis $\alpha = 0$.

Design of an optical turbine

To design an efficient optical turbine, we need solid microfibers tracing 3D paths that maximize reaction torque while minimizing bend losses. The rotor was designed as a four-arm structure where each arm is composed by two arcs with constant curvature radius R . The first one, appearing in green in Fig. 7.1(b), spans 90° and diverts axially incoming light in the radial direction. The second arc, in blue, lies on a plane that is orthogonal to the axial direction and extends for 135° ($3\pi/4$) turning light's propagation direction from radial to azimuthal. As a result, the radial distance of the fiber outputs from the structure axis is $r = (1 + \sqrt{2})R$. The total light emerging from the four fiber outputs will be $P = \beta\sigma\chi P_0$ with P_0 the input power and β, σ, χ , respectively, the attenuation due to bending, splitting, and coupling losses. For a fixed number of arms and fiber core diameters σ and χ will be constant while $\beta(r)$ will be a function of system size. Analysis of bend losses in our fibers suggests that curvature radius must be kept above $10\ \mu\text{m}$ to avoid severe bend losses. However, a much larger structure size would result in slower rotations and a smaller mechanical power output due to increasing viscous drag. To see this we recall from Eq. 7.1 that while the applied torque will scale as $T \sim P(r)r \sim \beta(r)r$ the rotational drag γ scales with the third power of the size, *i.e.* $\gamma \sim r^3$. Therefore the dissipated mechanical power will scale as $T\omega = T^2/\gamma \sim \beta^2(r)/r$. In order to evaluate $\beta(r)$, we first note that the total transmission over a semicircular arc can be written as $e^{-\alpha(R)\pi R}$ with $\alpha(R)$ the loss coefficient per unit length (see inset in Fig. 7.2(b)). We then obtain the fraction of transmitted power over the curved part of each arm in our structure as $\beta(r) = e^{-\alpha(R)L}$ with arm length $L = (5/4)\pi R$ and $R = r/(1 + \sqrt{2})$. We can then plot the expected mechanical power $\sim \beta^2(r)/r$ as a function of rotor size r as shown in Fig. 7.3(a). We select the value $r = 24\ \mu\text{m}$ which is close to the maximum and corresponds to $R = 10\ \mu\text{m}$. With this choice we expect to have an attenuation coefficient $\alpha(R) = 0.0176\ \mu\text{m}^{-1}$ (see Fig. 7.2(b)) and therefore we have $\beta(r) = 0.5$. Fig. 7.1(c) shows a 3D model of the full structure. In addition to the rotor (in green), we designed a static support (in blue) that prevents structure from falling and, once actuated with light, counteracts the recoiling force arising from the absorption of linear momentum in the axial direction. The structures were fabricated by the two photon polymerization of SU8 photoresist in a custom built setup [29]. Resulting 3D structures were imaged by scanning electron microscopy as shown in Fig. 7.1(d).

Torque to power performance

As a preliminary test, we recorded the free Brownian motion of the rotors when immersed in water. The rotor angle θ was extracted by a feature-tracking algorithm applied to optical microscopy images that were recorded by a digital camera running at 150 frames per second. The time evolution of the angular coordinate of seven different rotors is reported in Fig. 7.4 (left). We used the time tracks $\theta(t)$ to compute the mean square angular displacement that can be fitted by the linear function $2Dt$ to get the angular diffusion coefficient D , as shown in Fig. 7.4 (right). The rotational drag γ is related to the diffusivity D by the Stokes-Einstein relation $\gamma = k_B T/D = 151 \pm 15\ \text{pN}\ \mu\text{m}\ \text{s}\ \text{rad}^{-1}$. When a laser beam ($1064\ \text{nm}$) is focused

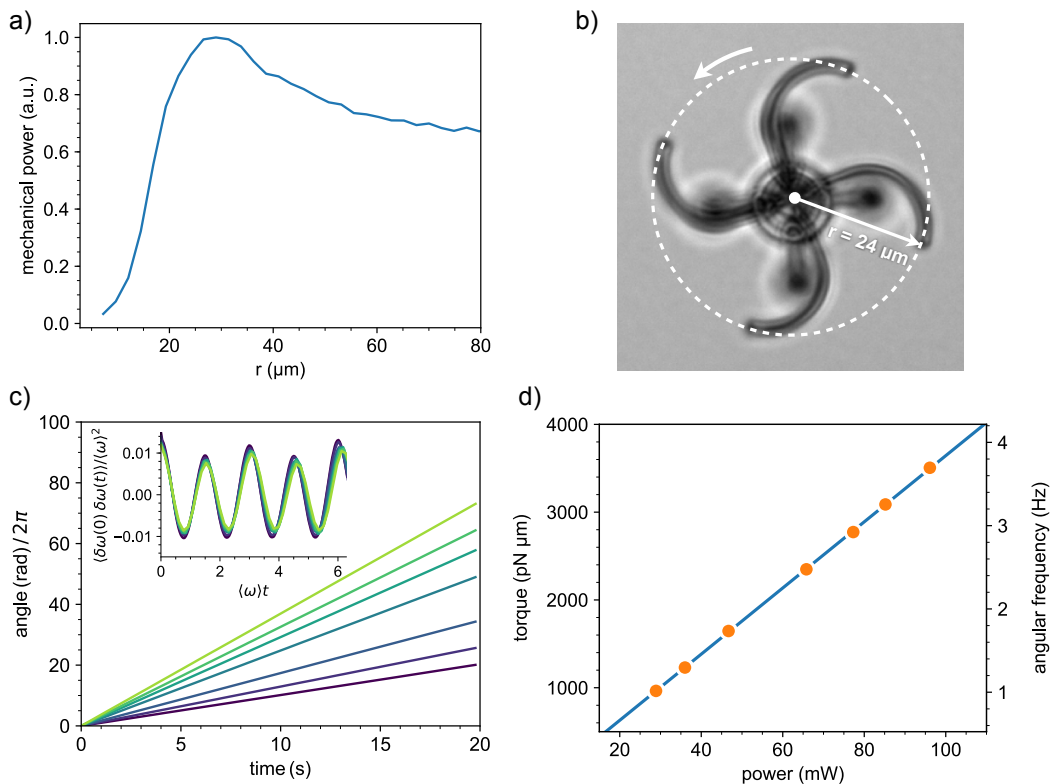


Figure 7.3. Rotating micro-turbines. (a) Expected mechanical power as a function of the structure radius. (b) Optical microscopy image of a rotating structure. (c) Time evolution of the angular position of a rotating structure driven by different laser powers. Inset shows the time auto-correlation function of the relative fluctuations of the angular speed. (d) Torque and angular frequency as a function of laser power. Laser power has been measured on the objective focal plane with a microscope slide power sensor (Thorlabs S170C). Solid line is a linear fit.

at the input fiber, the structures start to rotate smoothly with a speed that is linearly related to input laser power. Fig. 7.3(b) shows a bright-field image of a rotating structure. Fig. 7.3(c) shows the angular displacement $\theta(t)$ of the same rotating structure for different levels of incident laser power. The angle θ (shown in Fig. 7.3(c)) is a linear function of time plus a small periodic modulation. To show this, we compute the time auto-correlation of the normalized angular speed fluctuations $\delta\omega = (\omega - \langle\omega\rangle) / \langle\omega\rangle$ shown in the inset of Fig. 7.3(c). We find that these modulations are power independent and of the order of 10%. Moreover we observe that ω is higher than the average when the rotor arms are not aligned with the linear polarization direction of the laser. We also fabricated structures with 2 and 3 arms which are found to be unstable as they often rotate off axis and are much more prone to get stuck on the stator. For further information, however, we report in Fig. 7.5 the data of the average mean square angular displacement and the obtained rotational drag for rotors with 2, 3, and 4 arms. Extracting angular speeds $\langle\omega\rangle$ and multiplying by the previously determined rotational drag γ we obtain the linear torque vs power curve shown in Fig. 7.3(d). Similar results have been obtained for tens of experimental replica of our structures. Specifically, for four

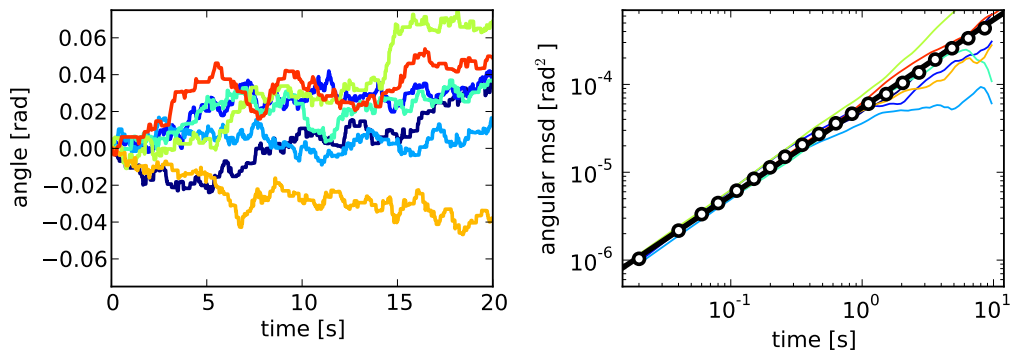


Figure 7.4. Rotor mean square angular displacement: time evolution of the angular coordinate $\theta(t)$ of seven rotors freely moving in water by Brownian motion (left), and mean square angular displacement of the same rotors with average values (dots) and a linear fit (solid line) (right).

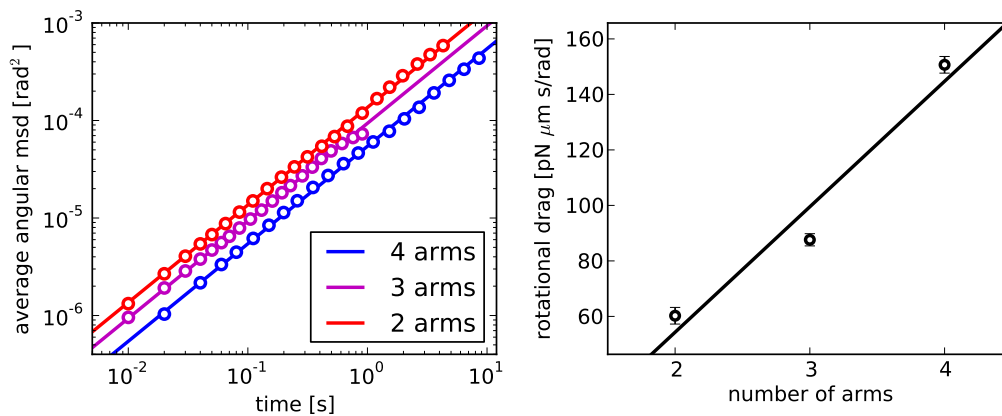


Figure 7.5. Average values and linear fit of the mean square angular displacement of rotors with 2, 3, and 4 arms freely moving in water by Brownian motion (left). Rotational drag of the same rotors extracted from mean square angular displacement data (right); the solid line is a guide to the eye.

rotors in the same batch, we found less than 5% deviation in rotational speed for any input power. Fitting data in Fig. 7.3(d) with a straight line we obtain a torque per unit power coefficient $\tau = T/P = 38 \pm 1 \text{ pN } \mu\text{m mW}^{-1}$. Eq. 7.2 sets an upper bound for this coefficient $\tau_{\text{max}} = nr/c = 107 \text{ pN } \mu\text{m mW}^{-1}$ where we have used $n = 1.33$ for water and $r = 24 \mu\text{m}$ as the radial distance of the fibers outputs from the structure axis. The ratio $\tau/\tau_{\text{max}} = 0.36$ provides a direct experimental value for the torque efficiency in our turbine. The combined effect of coupling, splitting and bend losses then amounts to a total attenuation $\beta(r)\sigma\chi = 0.36$. As discussed above, we can estimate for our structures a value for bend attenuation $\beta(r) = 0.5$. The remaining attenuation can be attributed to the combined effect of coupling and splitting, *i.e.* $\sigma\chi = 0.72$.

Discussion

We demonstrated that optical reaction micro-turbines can exploit guided light propagation to precisely and efficiently reroute an incoming flow of optical energy maximizing the exchanged angular momentum. The resulting torque reaches an unprecedented fraction (36%) of the maximum torque that can be extracted from an optical flow. This limit could be further improved by carefully shaping the driving beam to maximize light coupling with the structure base and minimize splitting losses. Synchronization phenomena in arrays of nearby turbines may also show nontrivial features arising from the interplay of hydrodynamic and optical couplings. Optical micro-pumps [206], driven by dynamically steered optical traps, have already been employed in micro-fluidic chips. Optical traps can generate forces of order QnP/c with Q a trapping efficiency factor that is usually in the range $10^{-2} - 10^{-1}$ (see Ref. [207]). In these systems, the theoretical torque efficiency is therefore a fraction Q of τ_{\max} (but in practice [208] often only of order 10^{-6}) suggesting that optical reaction micro-turbines could be more efficiently used as flow generators in micro-fluidic devices.

Chapter 8

Conclusion

In this PhD thesis we present a novel strategy for real-time exploration and manipulation of both synthetic and biological micro-systems through an immersive user interface. A 3-axis implementation of digital holographic microscopy provides high frame rate volumetric reconstructions of the sample with submicrometer resolution in the three directions of space. On a parallel track, holographic optical tweezers allow the live dynamic arrangement of multiple traps in 3D. Such holographic techniques for 3D imaging and micromanipulation are merged with, accessed, and controlled through the virtual reality technology, providing an unprecedented immersive and interactive experience of microscopic phenomena. For the first time we can enter our micro-sample, “walk” on a microscope slide, observe the dynamic phenomena that occur around us in real time and use our virtual hands to grab, move, and build 3D spatial arrangements of microscopic objects and living cells. In particular, we test our strategy on performing specific tasks such as configuring micron-sized particles in precise custom geometries. We observe a time-to-completion speedup factor of 6 with respect to performing the same task through a standard desktop interface. Our technique also facilitates the study of particles rapidly moving in the field of view. Thanks to the tailored virtual tools we developed, we can effortlessly trap swimming *E. coli* bacteria, which we can then manipulate, reorient, and release, just as we can analyze their morphological and dynamical features, all that in real time and with the possibility of floating around the observed bacterial cells. Furthermore, our system has also great potential for educational purposes. Indeed, we can design tailored didactic experiments that provide a direct experience of the micro-world. We report the example of the falling-body experiment, where a silica and a polystyrene spheres of $1\ \mu\text{m}$ radius are lifted to the same height and then released to observe their respective sedimentation at the micron scale. Simple phenomena like this one, whose physics at the macroscopic scale is commonly known, can be replicated on a microscopic scale within an immersive environment, which offers a more direct perception of the laws that dominate at those length scales. By applying the marching cubes algorithm to the reconstructed volume for segmentation and mesh extraction, we can also perform the live rendering of generic objects for which we lack an a priori morphological knowledge.

In the future, the approach we describe can be extended in many different directions and the last example we present is a glimpse of that. A system of living eu-

karyotic cells is immersively explored by implementing a different imaging technique that is more suitable to that kind of specimen. Using tomographic reconstructions we might interact with larger and more complex cells, whose reconstructed refractive index 3D map could be processed to obtain the mesh data of the cell membrane as well as of its organelles. All such cellular elements could be rendered in the virtual interface as embedded closed surfaces of different materials, which the user could observe either globally from outside or individually from within by entering the cell game object for a closer analysis of their behavior. For the real-time immersive exploration of the tomographic reconstructions of eukaryotic cells, however, faster algorithms will be required for image data acquisition and processing.

A further project is presented in the final chapter of the thesis, which reports how we developed an optical reaction micro-turbine whose design allows to extract the maximum torque from the input optical power. The structure, fabricated by direct laser writing via two-photon polymerization on SU8 photoresist, is made of four curved micron-sized optical fibers arranged in a shape resembling that of a garden sprinkler. By effectively rerouting the input flow of optical energy, such a sprinkler maximizes the exchanged angular momentum, which powers its rotation with unprecedented efficiency. Aiming to optimize the size of the final rotor, a study of power loss as a function of the fibers curvature with radius in the micron range was carried out. Experimental data show very good matching with the results of simulations performed through Beam Propagation Method. Conversely, the analytical prediction for curvature radii of few microns ($R < 20 \mu\text{m}$) fails. Experiments of this kind also offer interesting ideas to develop our VR interface. Another intriguing possibility for VR in the microscopic realm, indeed, is interactive microfabrication through optical lithography, where we design our structures using a VR CAD and then monitor the fabrication process in real time by holographic microscopy of the material being photo-polymerized. With this add-on, custom micro-tools for advanced microscopy applications as well as complex bio-hybrid micro-machines could be assembled and operated in an immersive environment.

8.1 Author contributions

In order to carry out the immersive micromanipulation project through our virtual reality interface, I worked together with my thesis advisor, Roberto Di Leonardo, two other researchers from our group, Silvio Bianchi and Giacomo Frangipane, and an external collaborator to our group, Barbara Cortese. The experiment was conceived and designed by Roberto and Silvio. Together with them, I was in charge of writing the software. In particular, I was mainly responsible for developing the software running on the “VR engine”, while Roberto and Silvio focused more on the software managing the holographic system. All the experiments were performed by Silvio and me. Giacomo provided us with *E. coli* bacteria, while Microglia cells were supplied by Barbara.

Regarding the optical reaction micro-turbine project, I worked with Roberto, Silvio, and other two researchers from our group, Gaszton Vizsnyiczai and Claudio Maggi. The experiments were designed by Roberto and Gaszton. Together with Gaszton and Silvio, I was in charge of performing experiments. Moreover, the

structures employed, namely the turbine and the arcs, were designed and fabricated by Gaszton and me. The simulations were performed by Roberto, Silvio, and me; Silvio, in addition, carried out theoretical analysis of bend losses. The microscopy data were analyzed by Gaszton and Claudio.

Appendix A

Light propagation through a spherical lens

In this appendix we show the rigorous derivation of Eq. 3.34 (see § 3.2), mapping the distribution of a monochromatic field in the back focal plane of a spherical lens to its distribution in the lens front focal plane (*i.e.* the Fourier plane) [80]. To this aim, we take advantage of the Fourier optics description of light propagation, based on harmonic analysis and linear systems. A generic monochromatic field propagating in a homogeneous medium, indeed, can be modelled as the superposition of independent plane waves. If the response of the system to each plane wave is known, its effect on an arbitrary wave can be determined as well using harmonic analysis at the input and the principle of superposition at the output. Furthermore, due to the important role Fourier analysis plays in describing linear systems, it is useful to analyze the propagation of light through linear optical components, including free space, using a linear-system approach.

Free-space propagation

We consider a monochromatic wave $E(x, y, z)$ of wavelength λ and wavevector of magnitude $k = 2\pi/\lambda$ in free space, whose Fourier transform definition is

$$E(x, y, z) = \frac{1}{4\pi^2} \iint A(k_x, k_y) e^{i(k_x x + k_y y + k_z z)} dk_x dk_y \quad (\text{A.1})$$

The global field is resolved into an infinite number of spatial harmonic functions of the form $A(k_x, k_y) e^{i(k_x x + k_y y + k_z z)}$, each one representing a plane wave of amplitude $A(k_x, k_y)$ and wavevector $\mathbf{k} = (k_x, k_y, k_z)$, with $k_z = \sqrt{k^2 - k_x^2 - k_y^2}$. Given the field distribution $E(x, y, 0) = E_0(x, y)$ in the plane $z = 0$, regarded as the input plane of the system, we derive the distribution $E(x, y, d) = E_d(x, y)$ in the plane $z = d$, regarded as the output plane. A linear system may be characterized either by its impulse-response function $h(x, y)$ (*i.e.* the response of the system to an impulse, or a point, at the input) or by its transfer function $\mathcal{H}(k_x, k_y)$ (*i.e.* the response to spatial harmonic functions). In particular, the transfer function $\mathcal{H}(k_x, k_y)$ is the factor by which an input spatial harmonic function of transverse wavevector (k_x, k_y) is multiplied to yield the output harmonic function. We therefore consider

a harmonic input function $E_0(x, y) = A e^{i(k_x x + k_y y)}$, corresponding to a plane wave $E(x, y, z) = A e^{i(k_x x + k_y y + k_z z)}$ in the plane $z = 0$. Since the output function is $E_d(x, y) = A e^{i(k_x x + k_y y + k_z d)}$, the transfer function of free space is

$$\mathcal{H}(k_x, k_y) = \frac{E_d(x, y)}{E_0(x, y)} = e^{ik_z d} = e^{i\sqrt{k^2 - k_x^2 - k_y^2} d} \quad (\text{A.2})$$

This expression can be simplified if the plane-wave components of the input field are such that $k_x \ll k$ and $k_y \ll k$ (*i.e.* in the paraxial approximation). As discussed in the text, in this case each plane-wave component propagates forming angles with the yz and xz planes respectively equal to

$$\begin{aligned} \theta_x &\approx k_x/k \\ \theta_y &\approx k_y/k \end{aligned} \quad (\text{A.3})$$

as shown also in Fig. A.1. By denoting the angle with the optical axis as

$$\theta^2 = \theta_x^2 + \theta_y^2 \approx \frac{k_x^2 + k_y^2}{k^2} \quad (\text{A.4})$$

the phase factor in Eq. A.2 becomes

$$\sqrt{k^2 - k_x^2 - k_y^2} d = kd \sqrt{1 - \theta^2} = kd \left(1 - \frac{\theta^2}{2} + \frac{\theta^4}{8} - \dots \right) \quad (\text{A.5})$$

We now suppose that the third term of this expansion is much smaller than π for all θ , namely

$$kd \frac{\theta^4}{8} \ll \pi \quad \implies \quad \frac{\theta^4 d}{4\lambda} \ll 1 \quad (\text{A.6})$$

With this approximation, known as the Fresnel approximation, the third and higher terms of the series expansion can be neglected and Eq. A.2 can be written as

$$\mathcal{H}(k_x, k_y) \approx \mathcal{H}_0 e^{-i\frac{kd}{2}\theta^2} = \mathcal{H}_0 e^{-i\frac{d}{2k}(k_x^2 + k_y^2)} \quad (\text{A.7})$$

where $\mathcal{H}_0 = e^{ikd}$. Given the input function $E_0(x, y)$, the output function $E_d(x, y)$ may be deduced as follows:

1. we determine the Fourier transform

$$A(k_x, k_y) = \iint E_0(x, y) e^{-i(k_x x + k_y y)} dx dy \quad (\text{A.8})$$

representing the complex envelopes of the plane-wave components in the input plane;

2. the product $\mathcal{H}(k_x, k_y) A(k_x, k_y)$ gives the complex envelopes of the plane-wave components in the output plane;
3. the complex amplitude in the output plane results from the sum of the contributions of all such plane waves:

$$E_d(x, y) = \frac{1}{4\pi^2} \iint \mathcal{H}(k_x, k_y) A(k_x, k_y) e^{i(k_x x + k_y y)} dk_x dk_y \quad (\text{A.9})$$

Using the Fresnel approximation for $\mathcal{H}(k_x, k_y)$, given by Eq. A.7, we have

$$E_d(x, y) = \frac{\mathcal{H}_0}{4\pi^2} \iint A(k_x, k_y) e^{-i\frac{d}{2k}(k_x^2 + k_y^2)} e^{i(k_x x + k_y y)} dk_x dk_y \quad (\text{A.10})$$

Eqs. A.8 and A.10 relate the output function $E_d(x, y)$ to the input function $E_0(x, y)$. An alternative procedure to relate the complex amplitudes E_0 and E_d involves the use of the impulse-response function $h(x, y)$ of the system. For the free-space propagation, it is defined as the response $E_d(x, y)$ when the input $E_0(x, y)$ is a point at the origin $(0, 0)$. We deduce from Eqs. A.8 and A.9 that it is the inverse Fourier transform of the transfer function $\mathcal{H}(k_x, k_y)$, namely

$$h(x, y) = \frac{1}{4\pi^2} \iint \mathcal{H}(k_x, k_y) e^{i(k_x x + k_y y)} dk_x dk_y \approx h_0 e^{i\frac{\pi}{\lambda d}(x^2 + y^2)} \quad (\text{A.11})$$

where $h_0 = -(i/\lambda d) e^{ikd}$. This function is proportional to the complex amplitude at the $z = d$ plane of a paraboloidal wave centered about the origin $(0, 0)$. Thus, we can regard E_0 as a superposition of different points, each producing a paraboloidal wave which is superposed to all the others at the output plane. The wave originating at the point (x', y') has an amplitude $E_0(x', y')$ and is centered about (x', y') so that it generates a wave with amplitude $E_0(x', y') h(x - x', y - y')$ at the point (x, y) in the output plane. The sum of these contributions is the two-dimensional convolution

$$E_d(x, y) = \iint E_0(x', y') h(x - x', y - y') dx' dy' \quad (\text{A.12})$$

which in Fresnel approximation becomes

$$E_d(x, y) = h_0 \iint E_0(x', y') e^{i\frac{\pi}{\lambda d}[(x-x')^2 + (y-y')^2]} dx' dy' \quad (\text{A.13})$$

Propagation in the far field

We have just shown that within the Fresnel approximation there are two approaches to determine the complex amplitude $E_d(x, y)$ in the output plane, given the complex amplitude $E_0(x, y)$ in the input plane. On the one hand, Eq. A.13 is based on a space-domain approach in which the input wave is expanded in terms of paraboloidal elementary waves. On the other hand, Eq. A.10 shows a frequency-domain approach in which the input wave is expanded as the sum of plane waves. However, at a sufficiently long distance only a single plane wave contributes to the total amplitude at each point in the output plane, while all other waves contributions cancel out due to destructive interference (Fraunhofer approximation). We now show that, if the propagation distance d in free space is sufficiently long, the only plane wave contributing to the complex amplitude at the point (x, y) in the output plane is the one forming angles $\theta_x \approx x/d$ and $\theta_y \approx y/d$ with the optical axis, as depicted in Fig. A.1. Such a wave has amplitude $A(k_x, k_y)$ and wavevector components $k_x \approx (x/d)k$ and $k_y \approx (y/d)k$. First of all, we compute the phase term in the argument of the exponent in Eq. A.13:

$$\frac{\pi}{\lambda d} [(x - x')^2 + (y - y')^2] = \frac{\pi}{\lambda d} [(x^2 + y^2) + (x'^2 + y'^2) - 2(xx' + yy')] \quad (\text{A.14})$$

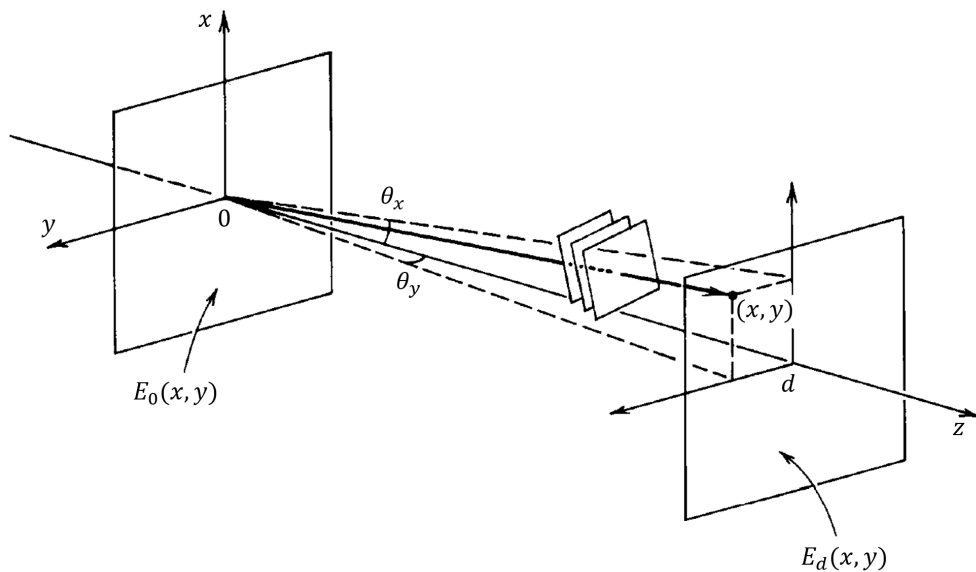


Figure A.1. Light propagation in free space. When the distance d is long enough, the complex amplitude at point (x, y) in the $z = d$ plane is proportional to the complex amplitude of the plane-wave component with angles $\theta_x \approx x/d \approx k_x/k$ and $\theta_y \approx y/d \approx k_y/k$, *i.e.* to the Fourier transform $A(k_x, k_y)$ of $E_0(x, y)$, with $k_x = kx/d$ and $k_y = ky/d$. Taken from [80].

If $E_0(x, y)$ is confined to a small area of radius b and if the distance d is large enough, then the phase factor $(\pi/\lambda d)(x'^2 + y'^2) \leq \pi(b^2/\lambda d)$ is negligible and Eq. A.13 can be approximated as

$$E_d(x, y) = h_0 e^{i\frac{\pi}{\lambda d}(x^2+y^2)} \iint E_0(x', y') e^{-i\frac{2\pi}{\lambda d}(xx'+yy')} dx' dy' \quad (\text{A.15})$$

We can identify the factors $\frac{2\pi x}{\lambda d} = k_x$ and $\frac{2\pi y}{\lambda d} = k_y$, so that

$$E_d(x, y) = h_0 e^{i\frac{\pi}{\lambda d}(x^2+y^2)} A\left(\frac{kx}{d}, \frac{ky}{d}\right) \quad (\text{A.16})$$

where $A(kx/d, ky/d)$ is the Fourier transform of $E_0(x, y)$. The phase factor $e^{i\frac{\pi}{\lambda d}(x^2+y^2)}$ may be neglected as well if we are interested in points in the output plane within a circle of radius a centered about the optical axis, so that $\pi(x^2 + y^2)/\lambda d \leq \pi a^2/\lambda d \ll \pi$ when $a^2/\lambda d \ll 1$.

Propagation through a spherical lens

We finally discuss the effect a spherical lens has on a generic monochromatic wave. A plane wave, for example, is turned into a paraboloidal wave focused to a point in the lens focal plane. If the plane wave arrives at small angles θ_x and θ_y , as in Fig. A.2, the paraboloidal wave is centered about the point $(\theta_x f, \theta_y f)$, where f is the focal length. In reference to the optical system shown in Fig. A.3, we denote as $E_0(x, y)$ the complex amplitude of the optical wave in the $z = 0$ plane. The field is decomposed into plane waves, each traveling at small angles $\theta_x = k_x/k$ and

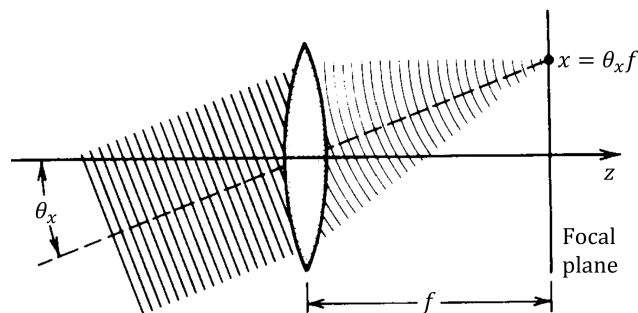


Figure A.2. A plane wave forming small angles (θ_x, θ_y) with the optical axis is focused by a thin spherical lens to a point $(x, y) = (\theta_x f, \theta_y f)$ in its focal plane. Taken from [80].

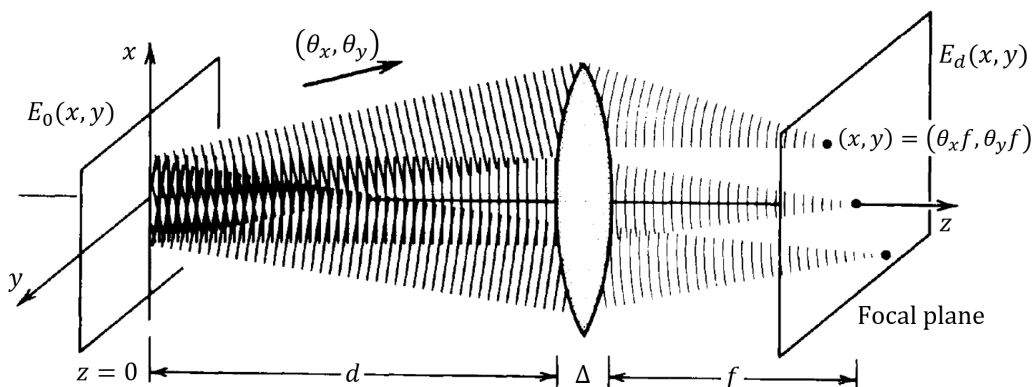


Figure A.3. Light propagation through a spherical lens. The field $E_0(x, y)$ at the input plane can be modelled as the sum of different plane waves. The plane wave with direction $(\theta_x, \theta_y) = (k_x/k, k_y/k)$ has amplitude proportional to the Fourier transform $A(k_x, k_y)$ and is focused at the point $(x, y) = (\theta_x f, \theta_y f) = (fk_x/k, fk_y/k)$. Taken from [80].

$\theta_y = k_y/k$ and having complex amplitude proportional to the Fourier transform $A(k_x, k_y)$. Such a wave is focused by the lens into a point (x, y) in the focal plane, where $x = \theta_x f = fk_x/k$ and $y = \theta_y f = fk_y/k$. The complex amplitude at point (x, y) in the output plane is therefore proportional to the Fourier transform of $E_0(x, y)$ evaluated at $k_x = kx/f$ and $k_y = ky/f$, so that

$$E_d(x, y) \propto A\left(\frac{kx}{f}, \frac{ky}{f}\right) \quad (\text{A.17})$$

To determine the proportionality factor in Eq. A.17, we analyze the input function $E_0(x, y)$ into its Fourier components and trace the plane wave corresponding to each component through the optical system. We then superpose the contributions of these waves at the output plane to obtain $E_d(x, y)$. All these waves will be assumed to be paraxial and the Fresnel approximation will be used. The procedure takes the following four steps.

1. The plane wave with angles $\theta_x = k_x/k$ and $\theta_y = k_y/k$ has complex amplitudes in the input plane ($z = 0$) and immediately before crossing the lens ($z = d$)

respectively equal to

$$E(x, y, 0) = A(k_x, k_y) e^{i(k_x x + k_y y)} \quad (\text{A.18})$$

$$E(x, y, d) = \mathcal{H}(k_x, k_y) A(k_x, k_y) e^{i(k_x x + k_y y)} \quad (\text{A.19})$$

where $\mathcal{H}(k_x, k_y) = \mathcal{H}_0 e^{-i\frac{d}{2k}(k_x^2 + k_y^2)}$ is the transfer function of a distance d of free space and $\mathcal{H}_0 = e^{ikd}$.

2. Upon crossing the lens, the complex amplitude is multiplied by the lens phase factor $e^{-i\frac{k}{2f}(x^2 + y^2)}$ (we neglect the phase factor $e^{ik\Delta}$, accounting for the lens width Δ). Thus

$$E(x, y, d + \Delta) = \mathcal{H}_0 e^{-i\frac{k}{2f}(x^2 + y^2)} e^{-i\frac{d}{2k}(k_x^2 + k_y^2)} A(k_x, k_y) e^{i(k_x x + k_y y)} \quad (\text{A.20})$$

This expression is simplified by writing

$$-\frac{k}{2f}x^2 + k_x x = -\frac{k}{2f}\left(x^2 - 2f\frac{k_x}{k}x\right) = -\frac{k}{2f}\left[(x - x_0)^2 - x_0^2\right] \quad (\text{A.21})$$

where $x_0 = fk_x/k$; a similar relation for y is written with $y_0 = fk_y/k$, so that

$$E(x, y, d + \Delta) = \tilde{A}(k_x, k_y) e^{-i\frac{k}{2f}[(x - x_0)^2 + (y - y_0)^2]} \quad (\text{A.22})$$

where

$$\tilde{A}(k_x, k_y) = \mathcal{H}_0 e^{i\frac{f-d}{2k}(k_x^2 + k_y^2)} A(k_x, k_y) \quad (\text{A.23})$$

3. In order to examine the propagation in the free space between the lens and the output plane, aiming to determine $E(x, y, d + \Delta + f)$, we apply Eq. A.13 to Eq. A.22. By means of the relation

$$\int e^{i\frac{2\pi}{\lambda f}(x - x_0)x'} dx' = \lambda f \delta(x - x_0) \quad (\text{A.24})$$

we obtain

$$E(x, y, d + \Delta + f) = h_0 (\lambda f)^2 \tilde{A}(k_x, k_y) \delta(x - x_0) \delta(y - y_0) \quad (\text{A.25})$$

where $h_0 = -(i/\lambda f) e^{ikf}$. Indeed, the plane wave is focused into a single point at (x_0, y_0) , with $x_0 = fk_x/k$ and $y_0 = fk_y/k$.

4. We finally integrate over all the plane waves (*i.e.* all k_x and k_y). By virtue of the sifting property of the delta function

$$\delta(x - x_0) = \delta\left(x - f\frac{k_x}{k}\right) = \frac{k}{f} \delta\left(k_x - k\frac{x}{f}\right) \quad (\text{A.26})$$

such an integral gives $E_d(x, y) = h_0 \tilde{A}\left(\frac{kx}{f}, \frac{ky}{f}\right)$. Substituting from Eq. A.23 we get

$$E_d(x, y) = h_l e^{i\frac{k(f-d)}{2f^2}(x^2 + y^2)} A\left(\frac{kx}{f}, \frac{ky}{f}\right) \quad (\text{A.27})$$

where $h_l = \mathcal{H}_0 h_0 = -(i/\lambda f) e^{ik(f+d)}$. It follows from Eq. A.27 that the field intensity at the output plane is

$$I_d(x, y) = \frac{1}{(\lambda f)^2} \left| A \left(\frac{kx}{f}, \frac{ky}{f} \right) \right|^2 \quad (\text{A.28})$$

The intensity of light at the lens focal plane is therefore proportional to the squared absolute value of the Fourier transform of the complex amplitude of the wave at the input plane, regardless of the distance d . Moreover, in the Fourier configuration, namely when $d = f$, the phase factor in Eq. A.27 vanishes and the field in the lens focal plane is

$$\begin{aligned} E_d(x, y) &= h_l A \left(\frac{kx}{f}, \frac{ky}{f} \right) = \\ &= -\frac{i}{\lambda f} e^{i2kf} \iint E_0(x', y') e^{-i\frac{k}{f}(xx'+yy')} dx' dy' \end{aligned} \quad (\text{A.29})$$

Bibliography

- [1] A. Ashkin, *Optical trapping and manipulation of neutral particles using lasers: a reprint volume with commentaries*. World Scientific, 2006.
- [2] P. H. Jones, O. M. Maragò, and G. Volpe, *Optical tweezers: Principles and applications*. Cambridge University Press, 2015.
- [3] M. Padgett and R. Di Leonardo, “Holographic optical tweezers and their relevance to lab on chip devices,” *Lab on a Chip*, vol. 11, no. 7, pp. 1196–1205, 2011.
- [4] T. L. Min, P. J. Mears, L. M. Chubiz, C. V. Rao, I. Golding, and Y. R. Chemla, “High-resolution, long-term characterization of bacterial motility using optical tweezers,” *Nature methods*, vol. 6, no. 11, pp. 831–835, 2009.
- [5] J. Guck, R. Ananthakrishnan, H. Mahmood, T. J. Moon, C. C. Cunningham, and J. Käs, “The optical stretcher: a novel laser tool to micromanipulate cells,” *Biophysical journal*, vol. 81, no. 2, pp. 767–784, 2001.
- [6] G. R. Kirkham, E. Britchford, T. Upton, J. Ware, G. M. Gibson, Y. Devaud, M. Ehrbar, M. Padgett, S. Allen, L. D. Buttery, *et al.*, “Precision assembly of complex cellular microenvironments using holographic optical tweezers,” *Scientific reports*, vol. 5, no. 1, pp. 1–7, 2015.
- [7] S. Maruo, O. Nakamura, and S. Kawata, “Three-dimensional microfabrication with two-photon-absorbed photopolymerization,” *Optics letters*, vol. 22, no. 2, pp. 132–134, 1997.
- [8] S. Kawata, H.-B. Sun, T. Tanaka, and K. Takada, “Finer features for functional microdevices,” *Nature*, vol. 412, no. 6848, p. 697, 2001.
- [9] H.-B. Sun and S. Kawata, “Two-photon photopolymerization and 3d lithographic microfabrication,” *NMR • 3D Analysis • Photopolymerization*, pp. 169–273, 2004.
- [10] R. Bowman, G. Gibson, D. Carberry, L. Picco, M. Miles, and M. Padgett, “itweezers: optical micromanipulation controlled by an apple ipad,” *Journal of Optics*, vol. 13, no. 4, p. 044002, 2011.
- [11] C. Pacoret, R. Bowman, G. Gibson, S. Haliyo, D. Carberry, A. Bergander, S. Régnier, and M. Padgett, “Touching the microworld with force-feedback optical tweezers,” *Optics express*, vol. 17, no. 12, pp. 10259–10264, 2009.

- [12] W. Choi, C. Fang-Yen, K. Badizadegan, S. Oh, N. Lue, R. R. Dasari, and M. S. Feld, “Tomographic phase microscopy,” *Nature methods*, vol. 4, no. 9, pp. 717–719, 2007.
- [13] Y. Kim, H. Shim, K. Kim, H. Park, J. H. Heo, J. Yoon, C. Choi, S. Jang, and Y. Park, “Common-path diffraction optical tomography for investigation of three-dimensional structures and dynamics of biological cells,” *Optics express*, vol. 22, no. 9, pp. 10398–10407, 2014.
- [14] J. Jung, K. Kim, J. Yoon, and Y. Park, “Hyperspectral optical diffraction tomography,” *Optics express*, vol. 24, no. 3, pp. 2006–2012, 2016.
- [15] J. M. Soto, J. A. Rodrigo, and T. Alieva, “Label-free quantitative 3d tomographic imaging for partially coherent light microscopy,” *Optics express*, vol. 25, no. 14, pp. 15699–15712, 2017.
- [16] S. Chowdhury, M. Chen, R. Eckert, D. Ren, F. Wu, N. Repina, and L. Waller, “High-resolution 3d refractive index microscopy of multiple-scattering samples from intensity images,” *Optica*, vol. 6, no. 9, pp. 1211–1219, 2019.
- [17] J. Lim, A. B. Ayoub, E. E. Antoine, and D. Psaltis, “High-fidelity optical diffraction tomography of multiple scattering samples,” *Light: Science & Applications*, vol. 8, no. 1, pp. 1–12, 2019.
- [18] M. Minderer, C. D. Harvey, F. Donato, and E. I. Moser, “Neuroscience: virtual reality explored,” *Nature*, vol. 533, no. 7603, pp. 324–325, 2016.
- [19] M. O’Connor, H. M. Deeks, E. Dawn, O. Metatla, A. Roudaut, M. Sutton, L. M. Thomas, B. R. Glowacki, R. Sage, P. Tew, *et al.*, “Sampling molecular conformations and dynamics in a multiuser virtual reality framework,” *Science advances*, vol. 4, no. 6, p. eaat2731, 2018.
- [20] T. De Jong, M. C. Linn, and Z. C. Zacharia, “Physical and virtual laboratories in science and engineering education,” *Science*, vol. 340, no. 6130, pp. 305–308, 2013.
- [21] R. Hollis, S. Salcudean, and D. Abraham, “Toward a tele-nanorobotic manipulation system with atomic scale force feedback and motion resolution,” in *IEEE Proceedings on Micro Electro Mechanical Systems, An Investigation of Micro Structures, Sensors, Actuators, Machines and Robots.*, pp. 115–119, IEEE, 1990.
- [22] R. M. Taylor, W. Robinett, V. L. Chi, F. P. Brooks Jr, W. V. Wright, R. S. Williams, and E. J. Snyder, “The nanomanipulator: a virtual-reality interface for a scanning tunneling microscope,” in *Proceedings of the 20th annual conference on Computer graphics and interactive techniques*, pp. 127–134, 1993.
- [23] M. Sitti and H. Hashimoto, “Tele-nanorobotics using atomic force microscope,” in *Proceedings. 1998 IEEE/RSJ International Conference on Intelligent Robots and Systems. Innovations in Theory, Practice and Applications (Cat. No. 98CH36190)*, vol. 3, pp. 1739–1746, IEEE, 1998.

- [24] M. Guthold, M. R. Falvo, W. G. Matthews, S. Paulson, S. Washburn, D. A. Erie, R. Superfine, F. Brooks, and R. M. Taylor, "Controlled manipulation of molecular samples with the nanomanipulator," *IEEE/ASME transactions on mechatronics*, vol. 5, no. 2, pp. 189–198, 2000.
- [25] A. Bolopion, H. Xie, D. S. Haliyo, and S. Régnier, "Haptic teleoperation for 3-d microassembly of spherical objects," *IEEE/ASME Transactions on Mechatronics*, vol. 17, no. 1, pp. 116–127, 2010.
- [26] F. Saglimbeni, S. Bianchi, A. Lepore, and R. Di Leonardo, "Three-axis digital holographic microscopy for high speed volumetric imaging," *Optics express*, vol. 22, no. 11, pp. 13710–13718, 2014.
- [27] S. Bianchi, F. Saglimbeni, and R. Di Leonardo, "Holographic imaging reveals the mechanism of wall entrapment in swimming bacteria," *Physical Review X*, vol. 7, no. 1, p. 011010, 2017.
- [28] S. Ferretti, S. Bianchi, G. Frangipane, and R. Di Leonardo, "A virtual reality interface for the immersive manipulation of live microscopic systems," *Scientific reports*, vol. 11, no. 1, pp. 1–9, 2021.
- [29] G. Vizsnyiczai, G. Frangipane, C. Maggi, F. Saglimbeni, S. Bianchi, and R. Di Leonardo, "Light controlled 3d micromotors powered by bacteria," *Nature communications*, vol. 8, p. 15974, 2017.
- [30] G. Binnig, H. Rohrer, C. Gerber, and E. Weibel, "Surface studies by scanning tunneling microscopy," *Physical review letters*, vol. 49, no. 1, p. 57, 1982.
- [31] G. Binnig and H. Rohrer, "Scanning tunneling microscopy," *Surface science*, vol. 126, no. 1-3, pp. 236–244, 1983.
- [32] G. Binnig and H. Rohrer, "Scanning tunneling microscopy—from birth to adolescence," *reviews of modern physics*, vol. 59, no. 3, p. 615, 1987.
- [33] J. Foster, J. Frommer, and P. Arnett, "Molecular manipulation using a tunnelling microscope," *Nature*, vol. 331, no. 6154, pp. 324–326, 1988.
- [34] T. Albrecht, M. Dovek, C. Lang, P. Grütter, C. Quate, S. Kuan, C. Frank, and R. Pease, "Imaging and modification of polymers by scanning tunneling and atomic force microscopy," *Journal of applied physics*, vol. 64, no. 3, pp. 1178–1184, 1988.
- [35] S.-i. Park and C. Quate, "Tunneling microscopy of graphite in air," *Applied physics letters*, vol. 48, no. 2, pp. 112–114, 1986.
- [36] R. Becker, J. Golovchenko, and B. Swartzentruber, "Atomic-scale surface modifications using a tunnelling microscope," *Nature*, vol. 325, no. 6103, pp. 419–421, 1987.
- [37] A. Kobayashi, F. Grey, R. Williams, and M. Aono, "Formation of nanometer-scale grooves in silicon with a scanning tunneling microscope," *Science*, vol. 259, no. 5102, pp. 1724–1726, 1993.

- [38] I.-W. Lyo and P. Avouris, "Field-induced nanometer-to atomic-scale manipulation of silicon surfaces with the stm," *Science*, vol. 253, no. 5016, pp. 173–176, 1991.
- [39] J. A. Stroscio and D. Eigler, "Atomic and molecular manipulation with the scanning tunneling microscope," *Science*, vol. 254, no. 5036, pp. 1319–1326, 1991.
- [40] T. A. Jung, R. R. Schlittler, J. Gimzewski, H. Tang, and C. Joachim, "Controlled room-temperature positioning of individual molecules: Molecular flexure and motion," *Science*, vol. 271, no. 5246, pp. 181–184, 1996.
- [41] S. Maruno, K. Inanaga, and T. Isu, "Threshold height for movement of c60 molecules on si (111)-7×7 with a scanning tunneling microscope," *Applied physics letters*, vol. 63, no. 10, pp. 1339–1341, 1993.
- [42] P. Beton, A. Dunn, and P. Moriarty, "Manipulation of c60 molecules on a si surface," *Applied Physics Letters*, vol. 67, no. 8, pp. 1075–1077, 1995.
- [43] B. Drake, C. Prater, A. Weisenhorn, S. Gould, T. Albrecht, C. Quate, D. Cannel, H. Hansma, and P. Hansma, "Imaging crystals, polymers, and processes in water with the atomic force microscope," *Science*, vol. 243, no. 4898, pp. 1586–1589, 1989.
- [44] S. Lindsay, L. Nagahara, T. Thundat, U. Knipping, R. Rill, B. Drake, C. Prater, A. Weisenhorn, S. Gould, and P. Hansma, "Stm and afm images of nucleosome dna under water," *Journal of Biomolecular Structure and Dynamics*, vol. 7, no. 2, pp. 279–287, 1989.
- [45] M. Guthold, M. Bezanilla, D. A. Erie, B. Jenkins, H. G. Hansma, and C. Bustamante, "Following the assembly of rna polymerase-dna complexes in aqueous solutions with the scanning force microscope," *Proceedings of the National Academy of Sciences*, vol. 91, no. 26, pp. 12927–12931, 1994.
- [46] M. Guthold, X. Zhu, C. Rivetti, G. Yang, N. H. Thomson, S. Kasas, H. G. Hansma, B. Smith, P. K. Hansma, and C. Bustamante, "Direct observation of one-dimensional diffusion and transcription by escherichia coli rna polymerase," *Biophysical journal*, vol. 77, no. 4, pp. 2284–2294, 1999.
- [47] D. Schaefer, R. Reifenberger, A. Patil, and R. Andres, "Fabrication of two-dimensional arrays of nanometer-size clusters with the atomic force microscope," *Applied Physics Letters*, vol. 66, no. 8, pp. 1012–1014, 1995.
- [48] T. Junno, K. Deppert, L. Montelius, and L. Samuelson, "Controlled manipulation of nanoparticles with an atomic force microscope," *Applied Physics Letters*, vol. 66, no. 26, pp. 3627–3629, 1995.
- [49] T. Ramachandran, A. Madhukar, P. Chen, and B. Koel, "Imaging and direct manipulation of nanoscale three-dimensional features using the noncontact atomic force microscope," *Journal of Vacuum Science & Technology A: Vacuum, Surfaces, and Films*, vol. 16, no. 3, pp. 1425–1429, 1998.

- [50] H. Hansma, J. Vesenka, C. Siegerist, G. Kelderman, H. Morrett, R. L. Sinsheimer, V. Elings, C. Bustamante, and P. Hansma, "Reproducible imaging and dissection of plasmid dna under liquid with the atomic force microscope," *Science*, vol. 256, no. 5060, pp. 1180–1184, 1992.
- [51] E. Henderson, "Imaging and nanodissection of individual supercoiled plasmids by atomic force microscopy," *Nucleic acids research*, vol. 20, no. 3, pp. 445–447, 1992.
- [52] J. Vesenka, M. Guthold, C. Tang, D. Keller, E. Delaine, and C. Bustamante, "Substrate preparation for reliable imaging of dna molecules with the scanning force microscope," *Ultramicroscopy*, vol. 42, pp. 1243–1249, 1992.
- [53] R. Stark, S. Thalhammer, J. Wienberg, and W. Heckl, "The afm as a tool for chromosomal dissection—the influence of physical parameters.," *Applied Physics A: Materials Science & Processing*, vol. 66, no. 7, 1998.
- [54] D. Sarid, R. Coratger, F. Ajustron, and J. Beauvillain, "Scanning force microscopy—with applications to electric, magnetic and atomic forces," *Microscopy Microanalysis Microstructures*, vol. 2, no. 6, pp. 649–649, 1991.
- [55] F. Ohnesorge and G. Binnig, "True atomic resolution by atomic force microscopy through repulsive and attractive forces," *Science*, vol. 260, no. 5113, pp. 1451–1456, 1993.
- [56] T. Stowe, K. Yasumura, T. Kenny, D. Botkin, K. Wago, and D. Rugar, "Attonewton force detection using ultrathin silicon cantilevers," *Applied Physics Letters*, vol. 71, no. 2, pp. 288–290, 1997.
- [57] J. E. Colgate, "Robust impedance shaping telemanipulation," *IEEE Transactions on robotics and automation*, vol. 9, no. 4, pp. 374–384, 1993.
- [58] P. G. Collins, A. Zettl, H. Bando, A. Thess, and R. Smalley, "Nanotube nanodevice," *Science*, vol. 278, no. 5335, pp. 100–102, 1997.
- [59] Z. Yao, H. W. C. Postma, L. Balents, and C. Dekker, "Carbon nanotube intramolecular junctions," *Nature*, vol. 402, no. 6759, pp. 273–276, 1999.
- [60] L. Yang, M. Anantram, J. Han, and J. Lu, "Band-gap change of carbon nanotubes: Effect of small uniaxial and torsional strain," *Physical Review B*, vol. 60, no. 19, p. 13874, 1999.
- [61] D. Bensimon, A. Simon, V. Croquette, and A. Bensimon, "Stretching dna with a receding meniscus: experiments and models," *Physical review letters*, vol. 74, no. 23, p. 4754, 1995.
- [62] E. F. Nichols and G. F. Hull, "The pressure due to radiation," in *Proceedings of the American Academy of Arts and Sciences*, vol. 38, pp. 559–599, JSTOR, 1903.
- [63] J. J. de Mairan, *Traité physique et historique de l'aurore boréale*. De l'Imprimerie royale, 1754.

- [64] J. C. Maxwell, *A treatise on electricity and magnetism*, vol. 1. Oxford: Clarendon Press, 1873.
- [65] A. G. Bartoli, *Sopra i movimenti prodotti dalla luce e dal calore: e sopra il radiometro di Crookes*. Coi tipi dei successori le Monnier, 1876.
- [66] A. Bartoli, "Il calorico raggianti e il secondo principio di termodinamica," *Il Nuovo Cimento (1877-1894)*, vol. 15, no. 1, pp. 193–202, 1884.
- [67] T. H. Maiman, "Stimulated optical radiation in ruby," *nature*, vol. 187, no. 4736, pp. 493–494, 1960.
- [68] C. H. Townes, *How The Laser Happened*. Oxford, U.K.: Oxford Univ. Press, 1999.
- [69] C.-E. Guillaume, *Rapports présentés au Congrès international de physique réuni à Paris en 1900 sous les auspices de la Société française de physique*, vol. 2. Gauthier-Villars, 1900.
- [70] P. Lebedev, "Experimental examination of light pressure," *Nuovo Cimento*, vol. 15, no. 195, p. 195, 1883.
- [71] A. Ashkin, "History of optical trapping and manipulation of small-neutral particle, atoms, and molecules," *IEEE Journal of Selected Topics in Quantum Electronics*, vol. 6, no. 6, pp. 841–856, 2000.
- [72] A. Ashkin, "Acceleration and trapping of particles by radiation pressure," *Physical review letters*, vol. 24, no. 4, p. 156, 1970.
- [73] A. Ashkin and J. Dziedzic, "Optical levitation by radiation pressure," *Applied Physics Letters*, vol. 19, no. 8, pp. 283–285, 1971.
- [74] A. Ashkin, J. M. Dziedzic, J. E. Bjorkholm, and S. Chu, "Observation of a single-beam gradient force optical trap for dielectric particles," *Optics letters*, vol. 11, no. 5, pp. 288–290, 1986.
- [75] A. Ashkin, "Trapping of atoms by resonance radiation pressure," *Physical Review Letters*, vol. 40, no. 12, p. 729, 1978.
- [76] S. Chu, J. Bjorkholm, A. Ashkin, and A. Cable, "Experimental observation of optically trapped atoms," *Physical review letters*, vol. 57, no. 3, p. 314, 1986.
- [77] A. Ashkin, "Forces of a single-beam gradient laser trap on a dielectric sphere in the ray optics regime," *Biophysical journal*, vol. 61, no. 2, pp. 569–582, 1992.
- [78] G. Roosen, "La levitation optique de spheres," *Canadian Journal of Physics*, vol. 57, no. 9, pp. 1260–1279, 1979.
- [79] G. Roosen and C. Imbert, "Optical levitation by means of two horizontal laser beams: a theoretical and experimental study," *Physics Letters A*, vol. 59, no. 1, pp. 6–8, 1976.

- [80] B. E. Saleh and M. C. Teich, *Fundamentals of photonics*. John Wiley & Sons, 2019.
- [81] H. Misawa, K. Sasaki, M. Koshioka, N. Kitamura, and H. Masuhara, "Multi-beam laser manipulation and fixation of microparticles," *Applied physics letters*, vol. 60, no. 3, pp. 310–312, 1992.
- [82] K. Sasaki, M. Koshioka, H. Misawa, N. Kitamura, and H. Masuhara, "Pattern formation and flow control of fine particles by laser-scanning micromanipulation," *Optics letters*, vol. 16, no. 19, pp. 1463–1465, 1991.
- [83] K. Visscher, G. Brakenhoff, and J. Krol, "Micromanipulation by "multiple" optical traps created by a single fast scanning trap integrated with the bilateral confocal scanning laser microscope," *Cytometry: The Journal of the International Society for Analytical Cytology*, vol. 14, no. 2, pp. 105–114, 1993.
- [84] K. Sasaki, H. Fujiwara, and H. Masuhara, "Optical manipulation of a lasing microparticle and its application to near-field microspectroscopy," *Journal of Vacuum Science & Technology B: Microelectronics and Nanometer Structures Processing, Measurement, and Phenomena*, vol. 15, no. 6, pp. 2786–2790, 1997.
- [85] K. Visscher, S. P. Gross, and S. M. Block, "Construction of multiple-beam optical traps with nanometer-resolution position sensing," *IEEE journal of selected topics in quantum electronics*, vol. 2, no. 4, pp. 1066–1076, 1996.
- [86] J. W. Goodman, *Introduction to Fourier optics*. Roberts and Company Publishers, 2005.
- [87] E. R. Dufresne and D. G. Grier, "Optical tweezer arrays and optical substrates created with diffractive optics," *Review of scientific instruments*, vol. 69, no. 5, pp. 1974–1977, 1998.
- [88] E. R. Dufresne, G. C. Spalding, M. T. Dearing, S. A. Sheets, and D. G. Grier, "Computer-generated holographic optical tweezer arrays," *Review of Scientific Instruments*, vol. 72, no. 3, pp. 1810–1816, 2001.
- [89] Y. Hayasaki, M. Itoh, T. Yatagai, and N. Nishida, "Nonmechanical optical manipulation of microparticle using spatial light modulator," *Optical review*, vol. 6, no. 1, pp. 24–27, 1999.
- [90] M. Reicherter, T. Haist, E. Wagemann, and H. J. Tiziani, "Optical particle trapping with computer-generated holograms written on a liquid-crystal display," *Optics letters*, vol. 24, no. 9, pp. 608–610, 1999.
- [91] J. Liesener, M. Reicherter, T. Haist, and H. J. Tiziani, "Multi-functional optical tweezers using computer-generated holograms," *Optics Communications*, vol. 185, no. 1-3, pp. 77–82, 2000.
- [92] J. E. Curtis, B. A. Koss, and D. G. Grier, "Dynamic holographic optical tweezers," *Optics communications*, vol. 207, no. 1-6, pp. 169–175, 2002.

- [93] D. G. Grier, “A revolution in optical manipulation,” *nature*, vol. 424, no. 6950, pp. 810–816, 2003.
- [94] G. C. Spalding, J. Courtial, and R. Di Leonardo, “Holographic optical tweezers,” *Structured light and its applications: an introduction to phase-structured beams and nanoscale optical forces*, p. 139, 2008.
- [95] P. Korda, G. C. Spalding, E. R. Dufresne, and D. G. Grier, “Nanofabrication with holographic optical tweezers,” *Review of Scientific Instruments*, vol. 73, no. 4, pp. 1956–1957, 2002.
- [96] S. Bianchi and R. Di Leonardo, “Real-time optical micro-manipulation using optimized holograms generated on the gpu,” *Computer Physics Communications*, vol. 181, no. 8, pp. 1444–1448, 2010.
- [97] J. Leach, G. Sinclair, P. Jordan, J. Courtial, M. J. Padgett, J. Cooper, and Z. J. Laczik, “3d manipulation of particles into crystal structures using holographic optical tweezers,” *Optics Express*, vol. 12, no. 1, pp. 220–226, 2004.
- [98] G. Sinclair, P. Jordan, J. Courtial, M. Padgett, J. Cooper, and Z. J. Laczik, “Assembly of 3-dimensional structures using programmable holographic optical tweezers,” *Optics Express*, vol. 12, no. 22, pp. 5475–5480, 2004.
- [99] G. Akselrod, W. Timp, U. Mirsaidov, Q. Zhao, C. Li, R. Timp, K. Timp, P. Matsudaira, and G. Timp, “Laser-guided assembly of heterotypic three-dimensional living cell microarrays,” *Biophysical journal*, vol. 91, no. 9, pp. 3465–3473, 2006.
- [100] P. Jordan, J. Leach, M. Padgett, P. Blackburn, N. Isaacs, M. Goksör, D. Hanstorp, A. Wright, J. Girkin, and J. Cooper, “Creating permanent 3d arrangements of isolated cells using holographic optical tweezers,” *Lab on a Chip*, vol. 5, no. 11, pp. 1224–1228, 2005.
- [101] R. Di Leonardo, S. Keen, J. Leach, C. Saunter, G. Love, G. Ruocco, and M. Padgett, “Eigenmodes of a hydrodynamically coupled micron-size multiple-particle ring,” *Physical Review E*, vol. 76, no. 6, p. 061402, 2007.
- [102] G. Vizsnyiczai, A. Búzás, B. L. Aekbote, T. Fekete, I. Grexa, P. Ormos, and L. Kelemen, “Multiview microscopy of single cells through microstructure-based indirect optical manipulation,” *Biomedical Optics Express*, vol. 11, no. 2, pp. 945–962, 2020.
- [103] D. B. Phillips, G. Gibson, R. Bowman, M. Padgett, S. Hanna, D. Carberry, M. Miles, and S. Simpson, “An optically actuated surface scanning probe,” *Optics express*, vol. 20, no. 28, pp. 29679–29693, 2012.
- [104] S. Bianchi, V. C. Sosa, G. Vizsnyiczai, and R. Di Leonardo, “Brownian fluctuations and hydrodynamics of a microhelix near a solid wall,” *Scientific Reports*, vol. 10, no. 1, pp. 1–8, 2020.

- [105] R. Di Leonardo, E. Cammarota, G. Bolognesi, H. Schäfer, and M. Steinhart, “Three-dimensional to two-dimensional crossover in the hydrodynamic interactions between micron-scale rods,” *Physical review letters*, vol. 107, no. 4, p. 044501, 2011.
- [106] J. Leach, K. Wulff, G. Sinclair, P. Jordan, J. Courtial, L. Thomson, G. Gibson, K. Karunwi, J. Cooper, Z. J. Laczik, *et al.*, “Interactive approach to optical tweezers control,” *Applied optics*, vol. 45, no. 5, pp. 897–903, 2006.
- [107] R. Di Leonardo, F. Ianni, and G. Ruocco, “Computer generation of optimal holograms for optical trap arrays,” *Optics Express*, vol. 15, no. 4, pp. 1913–1922, 2007.
- [108] M. Montes-Usategui, E. Pleguezuelos, J. Andilla, and E. Martín-Badosa, “Fast generation of holographic optical tweezers by random mask encoding of fourier components,” *Optics express*, vol. 14, no. 6, pp. 2101–2107, 2006.
- [109] J. E. Curtis, C. H. Schmitz, and J. P. Spatz, “Symmetry dependence of holograms for optical trapping,” *Optics letters*, vol. 30, no. 16, pp. 2086–2088, 2005.
- [110] L. Lesem, P. Hirsch, and J. Jordan, “The kinoform: a new wavefront reconstruction device,” *IBM Journal of Research and Development*, vol. 13, no. 2, pp. 150–155, 1969.
- [111] T. Haist, M. Reicherter, M. Wu, and L. Seifert, “Using graphics boards to compute holograms,” *Computing in Science & Engineering*, vol. 8, no. 1, pp. 8–13, 2006.
- [112] J. N. Mait, “Diffractive beauty,” *Optics and Photonics News*, vol. 9, no. 11, p. 21, 1998.
- [113] R. W. Gerchberg, “A practical algorithm for the determination of phase from image and diffraction plane pictures,” *Optik*, vol. 35, pp. 237–246, 1972.
- [114] N. Gallagher and B. Liu, “Method for computing kinoforms that reduces image reconstruction error,” *Applied optics*, vol. 12, no. 10, pp. 2328–2335, 1973.
- [115] R. Gerchberg, “Super-resolution through error energy reduction,” *Optica Acta: International Journal of Optics*, vol. 21, no. 9, pp. 709–720, 1974.
- [116] B. Liu and N. Gallagher, “Convergence of a spectrum shaping algorithm,” *Applied optics*, vol. 13, no. 11, pp. 2470–2471, 1974.
- [117] T. Haist, M. Schönleber, and H. Tiziani, “Computer-generated holograms from 3d-objects written on twisted-nematic liquid crystal displays,” *Optics Communications*, vol. 140, no. 4-6, pp. 299–308, 1997.
- [118] G. Sinclair, J. Leach, P. Jordan, G. Gibson, E. Yao, Z. J. Laczik, M. J. Padgett, and J. Courtial, “Interactive application in holographic optical tweezers of a multi-plane gerchberg-saxton algorithm for three-dimensional light shaping,” *Optics Express*, vol. 12, no. 8, pp. 1665–1670, 2004.

- [119] J. A. Neff, R. A. Athale, and S. H. Lee, “Two-dimensional spatial light modulators: a tutorial,” *Proceedings of the IEEE*, vol. 78, no. 5, pp. 826–855, 1990.
- [120] Y. Igasaki, F. Li, N. Yoshida, H. Toyoda, T. Inoue, N. Mukohzaka, Y. Kobayashi, and T. Hara, “High efficiency electrically-addressable phase-only spatial light modulator,” *Optical Review*, vol. 6, no. 4, pp. 339–344, 1999.
- [121] J. Amako and T. Sonehara, “Kinoform using an electrically controlled birefringent liquid-crystal spatial light modulator,” *Applied optics*, vol. 30, no. 32, pp. 4622–4628, 1991.
- [122] K. C. Neuman and S. M. Block, “Optical trapping,” *Review of scientific instruments*, vol. 75, no. 9, pp. 2787–2809, 2004.
- [123] G. D. Love, “Wave-front correction and production of zernike modes with a liquid-crystal spatial light modulator,” *Applied optics*, vol. 36, no. 7, pp. 1517–1524, 1997.
- [124] Y. Roichman, A. Waldron, E. Gardel, and D. G. Grier, “Optical traps with geometric aberrations,” *Applied optics*, vol. 45, no. 15, pp. 3425–3429, 2006.
- [125] K. D. Wulff, D. G. Cole, R. L. Clark, R. DiLeonardo, J. Leach, J. Cooper, G. Gibson, and M. J. Padgett, “Aberration correction in holographic optical tweezers,” *Optics express*, vol. 14, no. 9, pp. 4169–4174, 2006.
- [126] A. Jesacher, A. Schwaighofer, S. Fürhapter, C. Maurer, S. Bernet, and M. Ritsch-Marte, “Wavefront correction of spatial light modulators using an optical vortex image,” *Optics express*, vol. 15, no. 9, pp. 5801–5808, 2007.
- [127] A. Curran, S. Tuohy, D. G. Aarts, M. J. Booth, T. Wilson, and R. P. Dullens, “Decoupled and simultaneous three-dimensional imaging and optical manipulation through a single objective,” *Optica*, vol. 1, no. 4, pp. 223–226, 2014.
- [128] J. Pawley, *Handbook of biological confocal microscopy*, vol. 236. Springer Science & Business Media, 2006.
- [129] W. R. Zipfel, R. M. Williams, and W. W. Webb, “Nonlinear magic: multiphoton microscopy in the biosciences,” *Nature biotechnology*, vol. 21, no. 11, pp. 1369–1377, 2003.
- [130] P. A. Santi, “Light sheet fluorescence microscopy: a review,” *Journal of Histochemistry & Cytochemistry*, vol. 59, no. 2, pp. 129–138, 2011.
- [131] H. C. Berg, *E. coli in Motion*. Springer Science & Business Media, 2008.
- [132] J. Schwarz-Linek, J. Arlt, A. Jepson, A. Dawson, T. Vissers, D. Miroli, T. Pilizota, V. A. Martinez, and W. C. Poon, “Escherichia coli as a model active colloid: A practical introduction,” *Colloids and Surfaces B: Biointerfaces*, vol. 137, pp. 2–16, 2016.

- [133] S. Choi, P. Kim, R. Boutilier, M. Y. Kim, Y. Lee, and H. Lee, "Development of a high speed laser scanning confocal microscope with an acquisition rate up to 200 frames per second," *Optics express*, vol. 21, no. 20, pp. 23611–23618, 2013.
- [134] M. K. Kim, "Digital holographic microscopy," in *Digital Holographic Microscopy*, pp. 149–190, Springer, 2011.
- [135] J. Sheng, E. Malkiel, and J. Katz, "Digital holographic microscope for measuring three-dimensional particle distributions and motions," *Applied optics*, vol. 45, no. 16, pp. 3893–3901, 2006.
- [136] U. Schnars and W. Jüptner, "Direct recording of holograms by a ccd target and numerical reconstruction," *Applied optics*, vol. 33, no. 2, pp. 179–181, 1994.
- [137] E. Cuche, P. Marquet, and C. Depeursinge, "Simultaneous amplitude-contrast and quantitative phase-contrast microscopy by numerical reconstruction of fresnel off-axis holograms," *Applied optics*, vol. 38, no. 34, pp. 6994–7001, 1999.
- [138] U. Schnars and W. P. Jüptner, "Digital recording and numerical reconstruction of holograms," *Measurement science and technology*, vol. 13, no. 9, p. R85, 2002.
- [139] W. Xu, M. Jericho, I. Meinertzhagen, and H. Kreuzer, "Digital in-line holography of microspheres," *Applied optics*, vol. 41, no. 25, pp. 5367–5375, 2002.
- [140] Y. Park, G. Popescu, K. Badizadegan, R. R. Dasari, and M. S. Feld, "Fresnel particle tracing in three dimensions using diffraction phase microscopy," *Optics letters*, vol. 32, no. 7, pp. 811–813, 2007.
- [141] L. Cavallini, G. Bolognesi, and R. Di Leonardo, "Real-time digital holographic microscopy of multiple and arbitrarily oriented planes," *Optics letters*, vol. 36, no. 17, pp. 3491–3493, 2011.
- [142] S.-H. Lee, Y. Roichman, G.-R. Yi, S.-H. Kim, S.-M. Yang, A. Van Blaaderen, P. Van Oostrum, and D. G. Grier, "Characterizing and tracking single colloidal particles with video holographic microscopy," *Optics express*, vol. 15, no. 26, pp. 18275–18282, 2007.
- [143] S.-H. Lee and D. G. Grier, "Holographic microscopy of holographically trapped three-dimensional structures," *Optics Express*, vol. 15, no. 4, pp. 1505–1512, 2007.
- [144] J. Garcia-Sucerquia, W. Xu, S. K. Jericho, P. Klages, M. H. Jericho, and H. J. Kreuzer, "Digital in-line holographic microscopy," *Applied optics*, vol. 45, no. 5, pp. 836–850, 2006.
- [145] F. Shen and A. Wang, "Fast-fourier-transform based numerical integration method for the rayleigh-sommerfeld diffraction formula," *Applied optics*, vol. 45, no. 6, pp. 1102–1110, 2006.

- [146] J. Sheng, E. Malkiel, J. Katz, J. Adolf, R. Belas, and A. R. Place, "Digital holographic microscopy reveals prey-induced changes in swimming behavior of predatory dinoflagellates," *Proceedings of the National Academy of Sciences*, vol. 104, no. 44, pp. 17512–17517, 2007.
- [147] F. Saglimbeni, S. Bianchi, G. Bolognesi, G. Paradossi, and R. Di Leonardo, "Optical characterization of an individual polymer-shelled microbubble structure via digital holography," *Soft Matter*, vol. 8, no. 34, pp. 8822–8825, 2012.
- [148] L. Repetto, E. Piano, and C. Pontiggia, "Lensless digital holographic microscope with light-emitting diode illumination," *Optics letters*, vol. 29, no. 10, pp. 1132–1134, 2004.
- [149] F. Dubois, L. Joannes, and J.-C. Legros, "Improved three-dimensional imaging with a digital holography microscope with a source of partial spatial coherence," *Applied optics*, vol. 38, no. 34, pp. 7085–7094, 1999.
- [150] D. Tseng, O. Mudanyali, C. Oztoprak, S. O. Isikman, I. Sencan, O. Yaglidere, and A. Ozcan, "Lensfree microscopy on a cellphone," *Lab on a Chip*, vol. 10, no. 14, pp. 1787–1792, 2010.
- [151] H. C. Berg, "Escherichia coli in motion," *Biological, and Medical Physics Biomedical Engineering. Springer Verlag AIP: Press New York*, 2004.
- [152] S. Bianchi, F. Saglimbeni, A. Lepore, and R. Di Leonardo, "Polar features in the flagellar propulsion of e. coli bacteria," *Physical Review E*, vol. 91, no. 6, p. 062705, 2015.
- [153] P. D. Frymier, R. M. Ford, H. C. Berg, and P. T. Cummings, "Three-dimensional tracking of motile bacteria near a solid planar surface," *Proceedings of the National Academy of Sciences*, vol. 92, no. 13, pp. 6195–6199, 1995.
- [154] M. Vigeant and R. M. Ford, "Interactions between motile escherichia coli and glass in media with various ionic strengths, as observed with a three-dimensional-tracking microscope.," *Applied and Environmental Microbiology*, vol. 63, no. 9, pp. 3474–3479, 1997.
- [155] P. D. Frymier and R. M. Ford, "Analysis of bacterial swimming speed approaching a solid–liquid interface," *AIChE journal*, vol. 43, no. 5, pp. 1341–1347, 1997.
- [156] L. A. Pratt and R. Kolter, "Genetic analysis of escherichia coli biofilm formation: roles of flagella, motility, chemotaxis and type i pili," *Molecular microbiology*, vol. 30, no. 2, pp. 285–293, 1998.
- [157] T. K. Wood, A. F. G. Barrios, M. Herzberg, and J. Lee, "Motility influences biofilm architecture in escherichia coli," *Applied microbiology and biotechnology*, vol. 72, no. 2, pp. 361–367, 2006.
- [158] J. C. Conrad, "Physics of bacterial near-surface motility using flagella and type iv pili: implications for biofilm formation," *Research in microbiology*, vol. 163, no. 9-10, pp. 619–629, 2012.

- [159] W. R. DiLuzio, L. Turner, M. Mayer, P. Garstecki, D. B. Weibel, H. C. Berg, and G. M. Whitesides, “Escherichia coli swim on the right-hand side,” *Nature*, vol. 435, no. 7046, pp. 1271–1274, 2005.
- [160] P. Galajda, J. Keymer, P. Chaikin, and R. Austin, “A wall of funnels concentrates swimming bacteria,” *Journal of bacteriology*, vol. 189, no. 23, pp. 8704–8707, 2007.
- [161] R. Di Leonardo, L. Angelani, D. Dell’Arciprete, G. Ruocco, V. Iebba, S. Schippa, M. P. Conte, F. Mecarini, F. De Angelis, and E. Di Fabrizio, “Bacterial ratchet motors,” *Proceedings of the National Academy of Sciences*, vol. 107, no. 21, pp. 9541–9545, 2010.
- [162] A. Sokolov, M. M. Apodaca, B. A. Grzybowski, and I. S. Aranson, “Swimming bacteria power microscopic gears,” *Proceedings of the National Academy of Sciences*, vol. 107, no. 3, pp. 969–974, 2010.
- [163] S. Bianchi, F. Saglimbeni, G. Frangipane, D. Dell’Arciprete, and R. Di Leonardo, “3d dynamics of bacteria wall entrapment at a water–air interface,” *Soft matter*, vol. 15, no. 16, pp. 3397–3406, 2019.
- [164] E. Lauga, W. R. DiLuzio, G. M. Whitesides, and H. A. Stone, “Swimming in circles: motion of bacteria near solid boundaries,” *Biophysical journal*, vol. 90, no. 2, pp. 400–412, 2006.
- [165] S. E. Spagnolie and E. Lauga, “Hydrodynamics of self-propulsion near a boundary: predictions and accuracy of far-field approximations,” *arXiv preprint arXiv:1211.6996*, 2012.
- [166] R. Di Leonardo, D. Dell’Arciprete, L. Angelani, and V. Iebba, “Swimming with an image,” *Physical review letters*, vol. 106, no. 3, p. 038101, 2011.
- [167] L. Shaw, D. Preece, and H. Rubinsztein-Dunlop, “Kinect the dots: 3d control of optical tweezers,” *Journal of Optics*, vol. 15, no. 7, p. 075303, 2013.
- [168] <https://www.unity3D.com/>.
- [169] <https://www.visualstudio.microsoft.com/>.
- [170] J. S. Parkinson, “Complementation analysis and deletion mapping of escherichia coli mutants defective in chemotaxis.,” *Journal of bacteriology*, vol. 135, no. 1, pp. 45–53, 1978.
- [171] A. J. Wolfe, M. P. Conley, T. J. Kramer, and H. C. Berg, “Reconstitution of signaling in bacterial chemotaxis.,” *Journal of Bacteriology*, vol. 169, no. 5, pp. 1878–1885, 1987.
- [172] C. Jarzynski, “Equalities and inequalities: Irreversibility and the second law of thermodynamics at the nanoscale,” *Annu. Rev. Condens. Matter Phys.*, vol. 2, no. 1, pp. 329–351, 2011.

- [173] P. J. Rodrigo, L. Kelemen, D. Palima, C. A. Alonzo, P. Ormos, and J. Glückstad, “Optical microassembly platform for constructing reconfigurable microenvironments for biomedical studies,” *Optics Express*, vol. 17, no. 8, pp. 6578–6583, 2009.
- [174] W. E. Lorensen and H. E. Cline, “Marching cubes: A high resolution 3d surface construction algorithm,” *ACM siggraph computer graphics*, vol. 21, no. 4, pp. 163–169, 1987.
- [175] H. Gouraud, “Computer display of curved surfaces,” tech. rep., UTAH UNIV SALT LAKE CITY COMPUTER SCIENCE DIV, 1971.
- [176] H. Gouraud, “Continuous shading of curved surfaces,” *IEEE transactions on computers*, vol. 100, no. 6, pp. 623–629, 1971.
- [177] Y. Park, C. Depeursinge, and G. Popescu, “Quantitative phase imaging in biomedicine,” *Nature Photonics*, vol. 12, no. 10, pp. 578–589, 2018.
- [178] A. Diaspro, *Optical fluorescence microscopy: From the spectral to the nano dimension*. Springer Science & Business Media, 2010.
- [179] J. Lippincott-Schwartz, N. Altan-Bonnet, and G. H. Patterson, “Photobleaching and photoactivation: following protein dynamics in living cells,” *Nature cell biology*, pp. S7–14, 2003.
- [180] R. Hoebe, C. Van Oven, T. W. Gadella, P. Dhonukshe, C. Van Noorden, and E. Manders, “Controlled light-exposure microscopy reduces photobleaching and phototoxicity in fluorescence live-cell imaging,” *Nature biotechnology*, vol. 25, no. 2, pp. 249–253, 2007.
- [181] F. Zernike, “How i discovered phase contrast,” *Science*, vol. 121, no. 3141, pp. 345–349, 1955.
- [182] N. T. Shaked, Z. Zalevsky, and L. L. Satterwhite, *Biomedical optical phase microscopy and nanoscopy*. Academic Press, 2012.
- [183] D. Way, “Principles and applications of differential interference contrast light microscopy,” *Micros. Anal. Light Microsc. Suppl.*, vol. 20, pp. 9–11, 2006.
- [184] G. Popescu, *Quantitative phase imaging of cells and tissues*. McGraw Hill Professional, 2011.
- [185] T. H. Nguyen, M. E. Kandel, M. Rubessa, M. B. Wheeler, and G. Popescu, “Gradient light interference microscopy for 3d imaging of unlabeled specimens,” *Nature communications*, vol. 8, no. 1, pp. 1–9, 2017.
- [186] A. Köhler, “Ein neues beleuchtungsverfahren für mikrographische zwecke,” *Zeitschrift für wissenschaftliche Mikroskopie und für Mikroskopische Technik*, vol. 10, no. 4, pp. 433–440, 1893.
- [187] S. Bianchi, G. Vizsnyiczai, S. Ferretti, C. Maggi, and R. Di Leonardo, “An optical reaction micro-turbine,” *Nature communications*, vol. 9, no. 1, pp. 1–6, 2018.

- [188] B. R. Munson, T. H. Okiishi, A. P. Rothmayer, and W. W. Huebsch, *Fundamentals of fluid mechanics*. John Wiley & Sons, 2014.
- [189] P. Galajda and P. Ormos, “Rotors produced and driven in laser tweezers with reversed direction of rotation,” *Applied Physics Letters*, vol. 80, no. 24, pp. 4653–4655, 2002.
- [190] P. Galajda and P. Ormos, “Rotation of microscopic propellers in laser tweezers,” *Journal of Optics B: Quantum and Semiclassical Optics*, vol. 4, no. 2, p. S78, 2002.
- [191] H. Ukita and K. Nagatomi, “Optical tweezers and fluid characteristics of an optical rotator with slopes on the surface upon which light is incident and a cylindrical body,” *Applied optics*, vol. 42, no. 15, pp. 2708–2715, 2003.
- [192] E. Higurashi, H. Ukita, H. Tanaka, and O. Ohguchi, “Optically induced rotation of anisotropic micro-objects fabricated by surface micromachining,” *Applied Physics Letters*, vol. 64, no. 17, pp. 2209–2210, 1994.
- [193] H. Ukita and M. Kanehira, “A shuttlecock optical rotator-its design, fabrication and evaluation for a microfluidic mixer,” *IEEE Journal of selected topics in quantum electronics*, vol. 8, no. 1, pp. 111–117, 2002.
- [194] T. Asavei, T. A. Nieminen, V. L. Loke, A. B. Stilgoe, R. Bowman, D. Preece, M. J. Padgett, N. R. Heckenberg, and H. Rubinsztein-Dunlop, “Optically trapped and driven paddle-wheel,” *New Journal of Physics*, vol. 15, 2013.
- [195] T. Asavei, V. L. Loke, M. Barbieri, T. A. Nieminen, N. R. Heckenberg, and H. Rubinsztein-Dunlop, “Optical angular momentum transfer to microrotors fabricated by two-photon photopolymerization,” *New Journal of Physics*, vol. 11, no. 9, p. 093021, 2009.
- [196] J. E. Curtis and D. G. Grier, “Structure of optical vortices,” *Physical review letters*, vol. 90, no. 13, p. 133901, 2003.
- [197] M. Friese, T. Nieminen, N. Heckenberg, and H. Rubinsztein-Dunlop, “Optical alignment and spinning of laser-trapped microscopic particles,” *Nature*, vol. 394, no. 6691, p. 348, 1998.
- [198] A. I. Bishop, T. A. Nieminen, N. R. Heckenberg, and H. Rubinsztein-Dunlop, “Optical microrheology using rotating laser-trapped particles,” *Physical Review Letters*, vol. 92, no. 19, p. 198104, 2004.
- [199] Y. Arita, M. Mazilu, and K. Dholakia, “Laser-induced rotation and cooling of a trapped microgyroscope in vacuum,” *Nature communications*, vol. 4, p. 2374, 2013.
- [200] Y. Arita, A. W. McKinley, M. Mazilu, H. Rubinsztein-Dunlop, and K. Dholakia, “Picoliter rheology of gaseous media using a rotating optically trapped birefringent microparticle,” *Analytical chemistry*, vol. 83, no. 23, pp. 8855–8858, 2011.

-
- [201] D. Marcuse, "Curvature loss formula for optical fibers," *JOSA*, vol. 66, no. 3, pp. 216–220, 1976.
- [202] R. T. Schermer and J. H. Cole, "Improved bend loss formula verified for optical fiber by simulation and experiment," *IEEE Journal of Quantum Electronics*, vol. 43, no. 10, pp. 899–909, 2007.
- [203] C.-W. Lee, S. Pagliara, U. Keyser, and J. J. Baumberg, "Perpendicular coupling to in-plane photonics using arc waveguides fabricated via two-photon polymerization," *Applied Physics Letters*, vol. 100, no. 17, p. 171102, 2012.
- [204] A. Sharma, A.-H. Al-Ani, and S. Halme, "Constant-curvature loss in monomode fibers: an experimental investigation," *Applied optics*, vol. 23, no. 19, pp. 3297–3301, 1984.
- [205] G. L. Pedrola, *Beam Propagation Method for Design of Optical Waveguide Devices*. John Wiley & Sons, 2015.
- [206] S. Maruo and H. Inoue, "Optically driven micropump produced by three-dimensional two-photon microfabrication," *Applied Physics Letters*, vol. 89, no. 14, p. 144101, 2006.
- [207] N. Malagnino, G. Pesce, A. Sasso, and E. Arimondo, "Measurements of trapping efficiency and stiffness in optical tweezers," *Optics Communications*, vol. 214, no. 1-6, pp. 15–24, 2002.
- [208] M. Ito, M. Nakajima, H. Maruyama, and T. Fukuda, "On-chip fabrication and assembly of rotational microstructures," in *Intelligent Robots and Systems, 2009. IROS 2009. IEEE/RSJ International Conference on*, pp. 1849–1854, IEEE, 2009.